Emma Cave

Ions and Interfaces: Probing Fundamental Dynamics of Lithium-Ion Batteries

Emma Cave

A dissertation

submitted in partial fulfillment of the

requirements for the degree of

Doctor of Philosophy

University of Washington

2023

Reading Committee:

Cody Schlenker, Chair

Brandi Cossairt

Bo Zhang

Program Authorized to Offer Degree:

Chemistry

University of Washington

Abstract

Ions and Interfaces: Probing Fundamental Dynamics of Lithium-Ion Batteries

Emma Cave

Chair of the Supervisory Committee:
Professor Cody Schlenker
Department of Chemistry

Lithium-ion batteries have revolutionized the technological world as we know it today, however upgrades to next-generation materials will be required to meet the needs of a clean energy future. Group IV semiconductors such as silicon (Si) offer a high-capacity alternative to the current anode material (graphite). However, due to a difference in lithiation mechanism and surface chemistry, Si electrodes exhibit unstable cycling performance which impedes their commercialization. This thesis focuses on fundamental studies of interfacial processes at the anode/electrolyte interface using *in situ* vibrational spectroelectrochemistry. First, we study the kinetically-resolved correlations between interfacial ion speciation and lithium-ion storage in a model system by applying global analysis to our spectroelectrochemical data. We observe that it may be more kinetically viable for lithium to be extracted from contact ion pairs to contribute to faster charging rather than fully-solvated lithium. Next, we use a dipole surface modification to dynamically respond to weak spots of Si electrodes during cycling. This strategy allows for interfacial energetic tuning to mitigate unwanted parasitic reactions within the electrode and enhance cycling stability. In situ spectroelectrochemistry and electrochemical methods were used to probe the origin of enhanced stability. The fundamental studies presented in this thesis are meant to contribute to a deeper understanding of how interfacial processes behave in LIBs and inform future design of next-generation electrochemical energy storage systems.

TABLE OF CONTENTS

List of Figures iii

List of Tables vii

Chapter 1. Introduction 1

1.1 Clean Energy Storage 1

1.1.1 Increased Demand for Clean Energy Storage 1

1.1.2 Types of Energy Storage 3

1.2 Lithium-Ion Batteries 4

1.2.1 History of Lithium-Ion Batteries 4

1.2.2 Basic Operating Principles 5

1.2.3 Fundamental Studies to Inform Future Design 6

1.3 References 8

Chapter 2. Background 15

2.1 Lithium-Ion Battery Interfaces 15

2.1.1 LIB Electrodes 15

2.1.2 LIB Electrolyte 17

2.1.3 Solid-Electrolyte Interphase (SEI) 19

2.1.4 Tuning Interfacial Energetics 20

2.2 Electrochemical Characterization of Lithium-Ion Batteries 21

2.3 In Situ Vibrational Spectroelectrochemistry 22

2.3.1 Vibrational Spectroscopy Principles 22

2.3.2 In situ Vibrational Spectroelectrochemistry Cell Design 26

2.4 Global Analysis 28

2.5 References 29

Chapter 3. Ion-Pairing Dynamics Revealed by Kinetically Resolved In Situ FTIR Spectroelectrochemistry during Lithium-Ion Storage 34

3.1 Overview 34

3.2 Introduction 34

3.3 Experimental Methods 40

3.4 Results and Discussion 41

3.5 Conclusions 50

3.6 References 51

Chapter 4. Increased Capacity Retention in Li-Ion Battery Silicon Anodes by Dipole-Modification 57

4.1 Overview 57

4.2 Introduction 57

4.3 Experimental Methods 61

4.4 Results and Discussion 64

4.5 Conclusions 74

4.6 References 75

Appendix A: SUPPLEMENTARY INFORMATION FOR CHAPTER 3 80

LIST OF FIGURES

Figure 1.1. The International Energy Agency's (IEA) roadmap for the global energy sector to reach net zero by 2050. Reproduced from International Energy Agency (2021), Net Zero by 2050, IEA, Paris.[3] 2

Figure 1.2. Lithium-ion battery operation diagram depicting charge/discharge using a graphite anode on a copper current collector, lithium metal oxide cathode on an aluminum current collector, and electrolyte motion between the two electrodes across a separator....... 5

Figure 1.3. Energy density (Wh/L) vs. specific energy (Wh/kg) of current LIBs, energy-optimized LIBs, lithium-metal batteries, and post-LIB technologies (Li/S and Li/O_2). *Reproduced with permission from Springer Nature*.[17] 7

Figure 2.1. Tuning interfacial energetics using dipole surface modification. 20

Figure 2.2. Representative plot of diatomic molecule with harmonic (blue) and anharmonic (black) oscillator potential wells and energy levels. Potential energy V(r) as a function of atomic displacement from equilibrium (r). 23

Figure 2.3. Michelson interferometer components including laser, beamsplitter, stationary and moving mirrors and detector. 24

Figure 2.4. Single beam attenuated total reflectance (ATR) diagram. 25

Figure 2.5. (a) Picture of air-free in situ vibrational spectroelectrochemical cell designed and built for potential-dependent ATR-FTIR measurements of model system ATR accessory. (b) Cross-sectional scheme of the interior of the sample cell. 26

Figure 2.6. In situ FTIR spectroelectrochemical measurement protocol.......................... 27

Figure 2.7. Visual representation of the global target analysis fitting matrix. Our time-resolved data (bottom left) is represented as a superposition of n components, each containing distinct energy-dependent spectral species (top left). These species are weighted by a time-dependent concentration profile (bottom right). 28

Figure 3.1. (a) Nitrile stretch (solvation reporter) of 1.0 M $LiClO_4$ in acetonitrile (ACN) at open circuit potential (OCP). ACN coordinates to Li+ causing a blue shift of nitrile peak. Free nitrile stretch appears at 2253 cm^{-1} and coordinated nitrile appears at 2276 cm^{-1}, providing a signature for solvation. (b) Perchlorate stretch (ion pairing reporter) of 1.0 M $LiClO_4$ in

ACN at OCP. This is a convolution of multiple peaks corresponding to paired and unpaired anions. For the purposes of simplifying analysis, our focus will be on the most prominent peaks for paired (1134 cm^{-1}) and unpaired (1102 cm^{-1}) perchlorate. When a potential of -1 V (vs OCP) is applied to 1.0 M $LiClO_4$ in ACN using the in situ cell described in Figure 2.5, the concentration of coordinated (solvated)/ uncoordinated ACN (c) and paired/unpaired perchlorate (d) changes at the electrode/electrolyte interface. Spectra for (c) and (d) were collected at a time interval of ~150 s and serve as a qualitative representation of the change in species concentration due to applied potential.. 42

Figure 3.2. Time-resolved in situ ATR-FTIR spectroelectrochemistry data of (a) solvation (Li-ACN) signature and (b) ion pairing (Paired ClO_4^-) signature. Referenced against OCP, these data represent the difference in interfacial speciation due to an applied potential of -1V (vs. OCP). Spectra were collected every 8 minutes over a 99 minute window. 44

Figure 3.3. Species associated difference spectra (SADS) resulting from global target analysis of the time-resolved data for the (a) nitrile (solvation reporter) and (b) perchlorate (ion pairing reporter) vibrational stretches. SADS comprise vibrational signatures which are either enriched (positive peak) or depleted (negative peak) with the same time constant. The y-axis defined as SADS carries units of molar absorptivity. Concentration profiles of each SADS for the nitrile (a) and perchlorate (b) with respect to time are shown in (c) and (d), respectively. 45

Figure 3.4. (a) Power laws were fit to the baseline of each spectrum of the time-resolved data set to represent the electron accumulation within the TiO_2 electrode. (b) Global target analysis of the power law fits resolved two kinetic SADS for the electron accumulation, Fast and Slow. When overlaid with the SADS for the vibrational resonances of solvation and ion pairing, we reveal a kinetic correlation between ion speciation across the interface and charge storage. No electron accumulation species was found to match the Medium kinetic trace, indicating that the rise in its baseline is due to a frequency independent shift.47

Figure 3.5. (a) Initial organization of interfacial electrolyte species due to applied potential across the interface. (b) Fast time scale dissociation of CIPs kinetically correlated with the initial electron accumulation in the electrode. (c) Medium time scale re-equilibration desolvation of lithium and loss of all perchlorate (paired and unpaired) forms intermediate

state which is independent of electron accumulation. (d) Slow time scale charge storage resulting as a consequence of desolvated lithium. 49

Figure 4.1. (a) Silicon (orange sphere) volume expansion causes cracks in SEI layer (purple layer), further decomposition occurs at these crack sites and over many cycles grows a thick SEI layer which causes capacity fade. (b) dipolar surface modification can shift the Fermi energy of the anode relative to the electrochemical potential (μsol) of the electrolyte, making electrolyte reduction thermodynamically uphill. (c) interfacial energetic tuning strategy of binder modification (red line with arrow) allows the dipoles to dynamically align at crack sites to mitigate further SEI formation. 59

Figure 4.2. (a) Reaction scheme of poly(acrylic acid) (PAA) crosslinking with either 3-cyanopropyltriethoxysilane (CPTES) or Vinyltriethoxysilane (VTES). (b) FTIR characterization of the functional groups after modification for VTES-PAA (top, 1600 cm-1), CPTES-PAA (middle, 2255 cm^{-1}), and PAA (bottom). (c) Normalized carbonyl stretch of PAA [black], CPTES-PAA [blue] and VTES-PAA [red] (top) with difference spectra (bottom, modified – unmodified) showing blue shift with formation of silyl ester. 64

Figure 4.3. (a) Capacity retention (C/C2) of half cells made with 80% 50nm SiNP, 10% conductive carbon, and 10% binder (PAA [black] or CPTES-PAA [blue]). (b) Nyquist plot of half cells after seven cycles using PAA or CPTES-PAA and the corresponding equivalent circuit model and fits (lines), showing an increase in R_{CT} as seen in the second semicircle. (c) Differential capacity (dQ/dV) of the initial cycles for half cells made with PAA (black) and CPTES-PAA (blue). 66

Figure 4.4. Data corresponding to half cells made with 80% 150nm Si NP, 10% conductive carbon and 10% binder (PAA [P, black], CPTES-PAA [C-P, blue], VTES-PAA [V-P, red]). (a) Power cycling test after one formation cycle (C/20). (b) Capacity retention normalized to the 23rd cycle from plot (a) to monitor the stability of the cells after kinetic stress. (c) dQ/dV of cycle 36 (solid) and cycle 236 (dotted) from cycles shown in capacity retention plot. (d) Coulombic efficiency (C.E.) of first six cycles. 70

Figure 4.5. (a) In situ spectroelectrochemical FTIR spectra for binder-only films PAA (black), CPTES-PAA (blue), and VTES-PAA (red) in 1M $LiPF_6$ in 1:1 EC:DMC (10% FEC) after -1V (vs. OCP) polarization for one hour. Spectra collected every 4 minutes. Spectral window

shows C-O stretch for free and Li-coordinated EC (1202 cm^{-1} and 1158 cm^{-1}), respectively. Negative going peaks represent a diminished concentration of the corresponding species and positive going peaks are the increased concentration (b) EC-Li decay fits normalized for easier comparison with time constants. Due to measurement restrictions, time constants are to be taken as relative values rather than true values. 73

Figure A.1. Unbranched, unidirectional sequential model used for Global Target Analysis (Glotaran). Each box represents the kinetically distinct spectral species which includes all vibrational reporters evolving on the same time constant. The initial spectral species is populated by the speciation change due to the initial applied potential and subsequently decays into the second, Fast species with a time constant of τfast. The Fast species decays into the Medium, the Medium into the Slow, and the Slow decays back to equilibrium. Data was not collected for the process of re-equilibration, so the Slow species represents the longest-lived species but does not provide quantitative information regarding the re-equilibration process. 80

Figure A.2. Full FTIR spectrum of our sample cell with an anatase titanium dioxide electrode and 1.0 M lithium perchlorate ($LiClO_4$) electrolyte. Electrolyte signatures (~2250 cm^{-1} nitrile stretch and ~1100 cm^{-1} perchlorate stretch) and electrode signature (~750 cm^{-1} O-Ti-O stretch) are both resolved in our cell geometry. 81

Figure A.3. Broad, structureless signature associated with electron accumulation grows when a potential of -1 V (vs open circuit potential, OCP) is applied using our in situ cell for 1.0 M lithium perchlorate ($LiClO_4$) on the left. No such feature is observed when we switch to a larger cation in 1.0 M tetrabutylammonium perchlorate ($TBAClO_4$) on the right. A frequency independent baseline shift is observed in 1 M $TBAClO_4$. 81

Figure A.4. Chronoamperogram for corresponding in situ FTIR spectroelectroechemical measurement. X-axis scaled to relevant window of 8-100 min to match the corresponding spectral window. 82

LIST OF TABLES

Table 4.1. Equivalent circuit model fits of Nyquist plots from Figure 4.3....................... 66

ACKNOWLEDGEMENTS

First, I must thank my incredibly amazing wife, Emily. Your passion, drive, and ambition for making the world a better place inspired me to pursue this degree with empathy and awareness of my impact as a scientist. Throughout this experience, you have been my constant support, tireless motivator, pandemic office-mate, personal hype-man, and so much more. I truly don’t know if I could have made it through without you and I am grateful for you every single day. I love you, bid.

To my parents, thank you for your unwavering support and confidence in me. You have always made me feel like there is nothing I can’t tackle, and I am eternally grateful. Thank you for the unconditional love, pushing me to experience things outside of my comfort zone, the laughs at stupid SNL skits, playing the mouth horn in unison to the Olympics theme song, and always believing in me.

To Megan, thank you for being the best sister-in-law I could have hoped for. Growing up as an only child, the one thing I wanted the most was a sibling to do weird things with. I am so grateful I finally have that in you. Thank you for being the Magic Blake to my Magic Karl and always sending it to Darrell. I would follow you into hell, brother.

To Karen and David, thank you for being great in-laws. I am grateful for all the wonderful dinners, pool hangs, fireworks, dog adventures, and summer trips to recharge. Thank you for everything.

To all my friends in Seattle who have supported me throughout this time, I cannot thank you enough. Ali and Kynan, thank you for weathering the pandemic with us. Thank you for good food, overly competitive game nights, introducing me to LFC, travel adventures, coast trips, trying to get all the animals in one picture, and tub times. YNWA. Zack and Daniel, thank you for always being down to do weird stuff together, floating the river, watching Rupaul's Drag Race, and being number one Trysta Cherie fans. Oooooouuuuuhhhhhhhhh. Alex, thank you for always being down to grab coffee and chat about life and science. To everyone else in and out of Seattle who has been a friend and support system throughout this time, thank you so much. You are all truly my chosen family and I could not have done this without you.

I want to thank the staff in the Chemistry Department at the UW for your support and help throughout my time here. Diana, Leesa, Kristine, Mike, Christine, Adrienne, Martin and many others answered so many of my questions and made my time at the UW run smoothly and I am grateful for each of you. Thank you to Professor Andrea Carroll for always trusting me to be your lead TA.

Thank you to all the student club and organization members I had the pleasure of working with. Working with everyone in CEI, Torrance Tech, oSTEM at the UW, InCS, and ProCURE truly added a deeper meaning and purpose to my time in graduate school and I will forever be grateful for those experiences. I am also grateful to the entire team at Membrion who welcomed me into the team during my summer internship and gave me an amazing opportunity to learn and grow as a scientist.

Thank you to my exam committees, past and present, for their interest and time. To Professor Brandi Cossairt for serving on my general and final exam committees for your useful insights into my work and greater dedication to working towards creating an equitable, inclusive department. To Professor Munira Khalil for finding time to sit on my committee or attend my talks during your busy tenure as Department Chair. To Professor Bo Zhang for your astute questions and feedback on my work. To my GSRs Professor Vincent Holmberg and Professor Corie Cobb for your keen insight and perspective into my work. You all have helped me push to be a better scientist and I am grateful for you all.

I truly cannot express how grateful I am for all the members of the Schlenker Lab. To the original members – thank you for establishing such an amazing group, I feel lucky I was able to join when most of you were still around. To Dr. Jarred Olson, thank you for teaching me everything I know about batteries and electrochemistry, being a great mentor, and most of all being super weird along the way. To the Schlenker ladies, thank you for being so welcoming, warm, open, compassionate and supportive. Dr. Katie Corp, thank you for loving cranes with me, your never-ending support, and always listening to my teaching stories. Dr. Emily Rabe, thank you for your genuine interest in helping me with science completely unrelated to yours, your mentorship, and doing that all with goofiness. Dr. Sarah Pristash, thank you for becoming a senior member of the lab with me, for cry laughing at jokes, saving every picture of Kyle I sent you, for the Bachelor recaps and meme notes. I am truly so grateful that you stayed on as a post-doc during my final year so we could continue to recap reality shows together and hear your gossip podcast stories. Ryan, thank you for being an incredible scientist and an even more incredible gamer and friend. To the newer Schlenker members, I am so thankful you are the next generation to carry this group. Liam, thank you for all the wild stories and always being down to help out. Mark, thank you for inspiring RPDR discussions and your passion for teaching. Tyson, thank you for braving the pandemic with Glotaran and I and still sticking around. I am so thankful you were there to hold down Team Battery with me. Thank you for the pasta, rice, tapioca, and above all else Caraway Rye Triscuits (#noryenobuy). Chris, thank you for your hard work and being willing to jump into difficult projects. Alexis, thank you for introducing me to Max Headroom, your passion for Twilight, and overall being a great scientist and human. Cecily, thank you for sharing a love of queer reality shows, being eager to volunteer for things, and deeply caring about the science you do and for the people you are around. Anton, thank you for bringing new synthesis to the group. Doyk, thank you for your amazing scientific contributions and fun times over Zoom. To all the undergraduate students who worked on the battery project - Liam, Vanessa, and Thuy – thank you for being so willing to jump into new things. It was a privilege to share an office and Zoom calls with you all over the last six years and I truly think I could not have done it without you. Thank you.

Last, but certainly not least, I would like to thank my advisor Professor Cody Schlenker. Thank you for your passion for science, your willingness to learn alongside us, and your mentorship. Thank you for your guidance in navigating uncharted areas of science and boosting me up along the way. You have helped me become a better scientist over the last six years and I will always be grateful for your guidance.

DEDICATION

To Pig, Bear, Stink, Pork and McRib.

Chapter 1. Introduction

1.1 CLEAN ENERGY STORAGE

1.1.1 ***Increased Demand for Clean Energy Storage***

The global climate crisis has reached a “code red for humanity” according to the United Nations (UN) Secretary-General António Guterres.[1] This quote references a pivotal and eye-opening report published by the UN’s International Panel on Climate Change (IPCC) in 2021 which outlined the need for urgent, intentional action to combat the rapid global heating due to carbon dioxide (CO_2) and other greenhouse gas emission.[2] The report warns that we are at “imminent risk” of exceeding the Paris Agreement’s threshold of maintaining a global temperature increase of 1.5 °C since pre-industrial levels.[2] As the pace of the temperature rise gets faster and the threat of irreversible climate damage looms over us, it is imperative that we take intentional next steps to swiftly mitigating these effects by curbing the CO_2 emission. While the solutions to this problem are vast and widespread, from technological development to governmental policy change, energy storage plays a huge role.

In 2021, the International Energy Agency released an ambitious plan for reaching net zero emissions (NZE) by 2050.[3] Figure 1.1 depicts an overview of the global energy sectors and milestones involved in the roadmap to NZE. While clean energy storage will not solve the problem alone, it is a significant contributing factor in this roadmap. The successful implementation of the planned milestones of two of the larger sectors, Electricity/Heat and Transport, are reliant on advances in the field. According to this plan large-scale storage capacities will need to increase by 170x over the next three decades to meet the growing electricity demands of a world pushing for NZE.[3] Similar growth is required in the Transport sector, which projects the requirement of an 18x increase in electric vehicle sales by only 2030 (60% of global car sales).[3] Because of the wide variety of needs across several use cases (electric vehicles, grid storage, etc.) within the umbrella of this plan, it is important to highlight that there are multiple types of energy storage systems. These will be discussed in the following section.

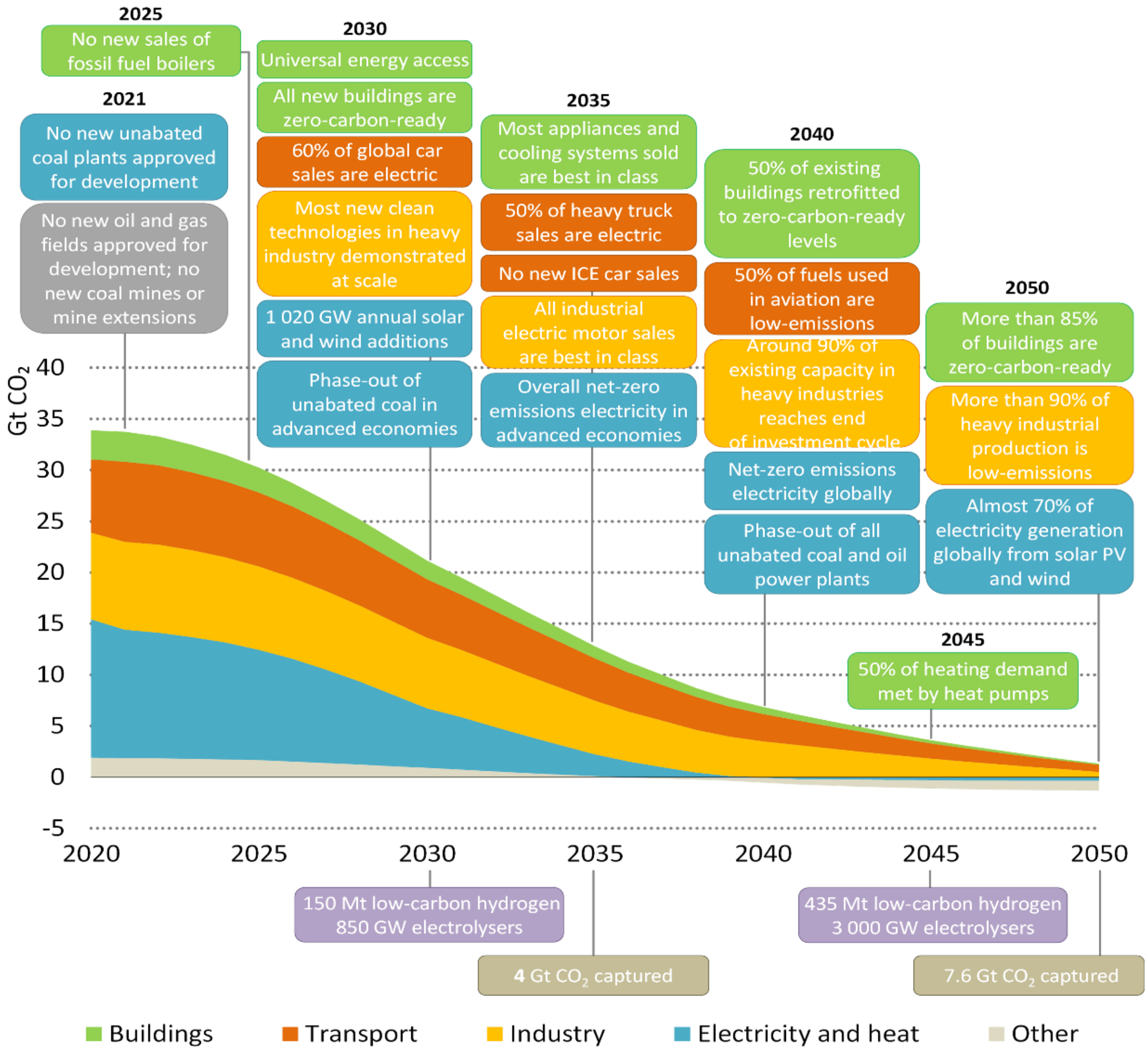

Figure 1.1. The International Energy Agency's (IEA) roadmap for the global energy sector to reach net zero by 2050. Reproduced from International Energy Agency (2021), Net Zero by 2050, IEA, Paris.[3]

1.1.2 *Types of Energy Storage*

Renewable energy storage systems have become ubiquitous when considering a clean energy future. Broadly, energy storage systems (ESS) can be classified under one of the following categories: mechanical, thermal, chemical, electrochemical, electrical, magnetic or a hybrid blend comprising two separate forms.[4] The type of ESS chosen depends greatly on the requirements of a given application. As of 2022, pumped hydro storage accounted for 95% of the global storage capacity.[5] This system uses a mechanical energy storage mechanism via the movement of water between reservoir’s positioned at different heights. While this is a good candidate for large-scale storage, its topological requirements and detrimental effects on the land are less than ideal. The diversification of energy storage systems is required to meet the goals for reaching NZE by 2050.

While it is expected that pumped hydro will remain dominant in global energy storage capacity for the near future, electrochemical energy storage systems (EESS) like batteries are rapidly increasing. EESS harness chemical energy by converting it to electrical energy and are suitable for applications that require high energy density (batteries) or power density (supercapacitors).[5] Classified as either primary (single-use) or secondary (rechargeable), batteries offer an array of opportunities that other storage mechanisms do not. Most notably, lithium-ion batteries (LIB) have enabled the world as we know it today. Due to lithium’s monovalent charge, low reduction potential and small size, LIBs have high energy density and have revolutionize the technological world as we know it today.[6] In the race to NZE by 2050, LIB will play a huge role. This work aims to study fundamental processes in these systems using in situ vibrational spectroelectrochemistry to help inform future design.

1.2 LITHIUM-ION BATTERIES

1.2.1 ***History of Lithium-Ion Batteries***

The birth of lithium-ion batteries as we know it dates to the late 1970s. The pioneering research work of Dr. Stanley Whittingham, Dr. John Goodenough, Dr. Akira Yoshino and countless others laid the foundation for the technological world we know today. Born out of the petroleum crisis of the 1970s, the search for enabling the use of alternative energy sources began.[7] In the mid-1970s , Dr. Whittingham discovered that lithium ions (Li^+) could intercalate into transition metal disulphides (TiS_2) and dichalcogenides which lead to the construction of the first rechargeable LIB.[8-10] Building on this work, in the 1980s Dr. Goodenough and coworkers demonstrated the effective use of transition metal oxide cathode materials as a more stable alternative to disulphides.[11-13] While many research developments have been made over the several decades, transition metal oxides remain dominant in commercial cathodes.[14] The quest for a commercially viable LIB was incomplete without the addition of a stable anode. Although it was known that lithium ions could intercalate into graphite, Dr. Yoshino and his team at Asahi Chemical recognized that it typically decomposed in the presence of the common electrolyte solvent propylene carbonate (PC).[15] As such, he focused on using carbonaceous materials with specific crystalline structures to enable the intercalation process but circumvent the decomposition of PC.[16] This was the prototype that lead to the commercialization of the first LIB in the 1990s, enabling energy-dense rechargeable processes and revolutionizing the world as we know it today.

1.2.2 *Basic Operating Principles*

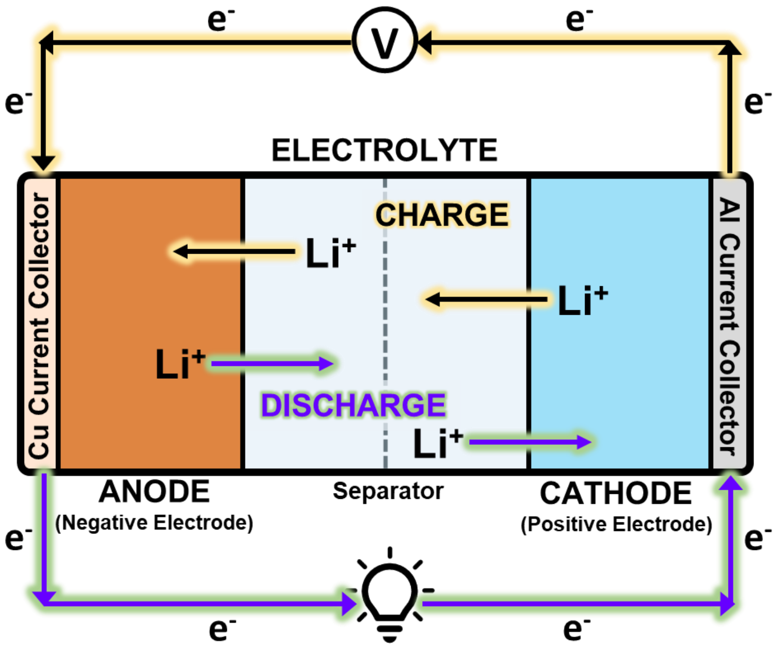

Figure 1.2. Lithium-ion battery operation diagram depicting charge/discharge using a graphite anode on a copper current collector, lithium metal oxide cathode on an aluminum current collector, and electrolyte motion between the two electrodes across a separator.

Lithium-ion batteries are secondary energy storage devices that store charge via electrochemical reactions. Figure 1.2 depicts a conventional LIB comprising three active components – graphite anode, lithium metal oxide cathode and lithium salt-based electrolyte. The two solid electrodes are used for Li^+ storage while the liquid electrolyte acts as an ion shuttle within the device. During charge, an external electrical power source (i.e., charger) is attached to the device which initiates the flow of electrons around an external circuit from the cathode to the anode. Concomitantly, the positively charged lithium ions migrate from the cathode, through the electrolyte and separator, to the anode to compensate for the negative charge of the electrons. The exact opposite process occurs during discharge. When the device is unplugged, the lithium ions spontaneously migrate from the anode to be stored in the more thermodynamically stable state within the cathode while the electrons flow around the external circuit to provide electricity. The inactive materials within the LIB act as electron conductors (current collectors) or insulators (separators) to ensure electrons flow through the external circuit rather than internally. This work aims to investigate fundamental processes and manipulation strategies at the anode/electrolyte interface. As such, we will simplify the system studied by only considering half-cell battery geometries, using lithium metal as the cathode, and focusing specifically on lithiation and delithiation of the active electrode (anode). See Section 2.1 for more information on electrode and electrolyte materials and properties.

1.2.3 *Fundamental Studies to Inform Future Design*

Despite their commercial success since the 1990s, improvements to current LIBs are required to meet the demands of NZE by 2050.[3] Using electric vehicles as an examples, next-generation batteries must be able to store a large amount of charge in a small mass (specific energy Wh/kg) and a small volume (energy density Wh/L), charge quickly, low cost, and long lifetime (cycle life). While the current LIBs have enabled the commercialization of electric vehicles, they are limited by a relatively low charge capacity compared to next-generation materials and technologies. Figure 1.3 demonstrates the relative capacities (energy density vs. specific energy) of current state of the art LIBs, energy optimized LIBs, lithium-metal batteries (CLIM), lithium-sulfur (Li/S) batteries and lithium-air (Li/O_2) batteries.[17] Beyond the state of the art LIBs (current LIB with optimized cathode/anode combination), each one of these next-generation technologies requires a fundamental understanding of their materials and chemistries.[18] Specifically, the work presented in this thesis will focus on studying interfacial processes and modification strategies to inform future design of high capacity, alloying anode materials such as silicon (Si). See Section 2.1 for more background information.

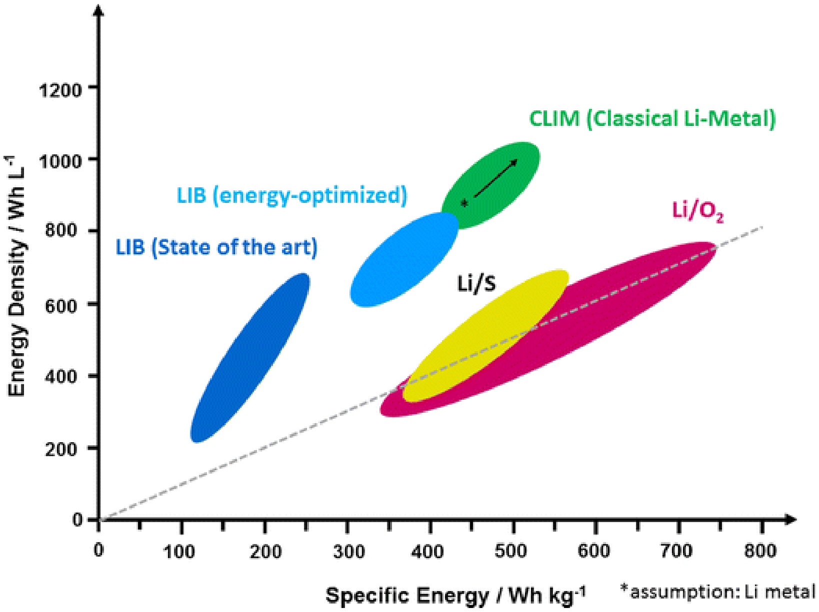

Figure 1.3. Energy density (Wh/L) vs. specific energy (Wh/kg) of current LIBs, energy-optimized LIBs, lithium-metal batteries, and post-LIB technologies (Li/S and Li/O_2). *Reproduced with permission from Springer Nature*.[17]

Over the last several decades, researchers in the energy storage field have developed quite a few analytical techniques to provide mechanistic insights into current and next-generation LIB systems such as silicon anodes. Since the most important processes within these systems are inherently interfacial and dynamic (lithiation, delithiation, electron tunneling, etc.), in situ characterization methods are a specifically powerful subset of tools.[19] Influential insights into silicon anode mechanism have been elucidated by several in situ techniques including but not limited to: scanning electrochemical microscopy, atomic force microscopy,[20-22] x-ray spectroscopy,[23, 24] nuclear magnetic resonance spectroscopy,[25-27] Raman spectroscopy, and Fourier-transform infrared (FTIR) spectroscopy.[19, 28-64] This thesis will focus on using the latter technique (in situ vibrational spectroelectrochemistry) to study fundamental processes.

The scope of this thesis is to study fundamental ion dynamics and interface modification strategies to inform future design of next-generation anode materials. Building off the foundational literature of LIB analysis techniques, I will describe the in situ vibrational spectroelectrochemical cell that I have built to enable the study of the anode/electrolyte interface of LIBs. When coupled with a time-resolved spectroscopy analysis method called global analysis,[65] this characterization technique is a powerful tool for probing the dynamics of vibrational reporters within an LIB model system. I will next describe an electrostatic surface modification strategy we have tested as a tool for mitigating capacity fade in next-generation alloying anodes. Employing the in situ spectroelectrochemical technique with battery cycling data will provide mechanistic insight into the origin of the enhanced performance observed.

1.3 REFERENCES

1. Guterres, A. Secretary-General's statement on the IPCC Working Group 1 Report on the Physical Science Basis of the Sixth Assessment | United Nations Secretary-General. https://www.un.org/sg/en/content/secretary-generals-statement-the-ipcc-working-group-1-report-the-physical-science-basis-of-the-sixth-assessment?_gl=1*fd5i30*_ga*ODA0OTI2Mjk5LjE2ODM3MzU2MjI.*_ga_TK9BQL5X7Z*MTY4MzczNTYyMS4xLjEuMTY4MzczNjQzNC4wLjAuMA..
2. Arias, P.; Bellouin, N.; Coppola, E.; Jones, R.; Krinner, G.; Marotzke, J.; Naik, V.; Palmer, M.; Plattner, G.-K.; Rogelj, J., Climate Change 2021: The Physical Science Basis. Contribution of Working Group I to the Sixth Assessment Report of the Intergovernmental Panel on Climate Change; Technical Summary. **2021**.
3. Bouckaert, S.; Pales, A. F.; McGlade, C.; Remme, U.; Wanner, B.; Varro, L.; D'Ambrosio, D.; Spencer, T. *Net zero by 2050: A roadmap for the global energy sector*; License: CC BY 4.0; International Energy Agency: Paris, 2021.
4. Rahman, M. M.; Oni, A. O.; Gemechu, E.; Kumar, A., Assessment of energy storage technologies: A review. *Energy Convers. Manage.* **2020,** *223*, 113295.

5. Chakraborty, M. R.; Dawn, S.; Saha, P. K.; Basu, J. B.; Ustun, T. S., A Comparative Review on Energy Storage Systems and Their Application in Deregulated Systems. *Batteries* **2022,** *8* (9), 124.
6. Mitali, J.; Dhinakaran, S.; Mohamad, A. A., Energy storage systems: a review. *Energy Storage and Saving* **2022,** *1* (3), 166-216.
7. Winter, M.; Barnett, B.; Xu, K., Before Li Ion Batteries. *Chem. Rev.* **2018,** *118* (23), 11433-11456.
8. Whittingham, M. S., Electrointercalation in transition-metal disulphides. *J. Chem. Soc., Chem. Commun.* **1974,** (9), 328.
9. Whittingham, M. S.; Gamble, F. R., The lithium intercalates of the transition metal dichalcogenides. *Mater. Res. Bull.* **1975,** *10* (5), 363-371.
10. Whittingham, M. S., Electrical Energy Storage and Intercalation Chemistry. *Science* **1976,** *192* (4244), 1126-1127.
11. Mizushima, K.; Jones, P. C.; Wiseman, P. J.; Goodenough, J. B., $LixCoO_2$ ($0<x<-1$): A new cathode material for batteries of high energy density. *Mater. Res. Bull.* **1980,** *15* (6), 783-789.
12. Mizushima, K.; Jones, P. C.; Wiseman, P. J.; Goodenough, J. B., $LixCoO_2$ ($0<x\leqslant 1$): A new cathode material for batteries of high energy density. *Solid State Ionics* **1981,** *3-4*, 171-174.
13. Goodenough, J.; Mizuchima, K. Electrochemical cell with new fast ion conductors. US 4302518, 1981.
14. Manthiram, A., A reflection on lithium-ion battery cathode chemistry. *Nature Communications* **2020,** *11* (1).
15. Yoshino, A., The Birth of the Lithium-Ion Battery. *Angew. Chem. Int. Ed.* **2012,** *51* (24), 5798-5800.
16. Yoshino, A.; Sanechika, K.; Nakajima, T. Secondary battery. U.S. Patent No. 4,668,595, 26 May 1987, 1987.
17. Placke, T.; Kloepsch, R.; Dühnen, S.; Winter, M., Lithium ion, lithium metal, and alternative rechargeable battery technologies: the odyssey for high energy density. *J. Solid State Electrochem.* **2017,** *21* (7), 1939-1964.
18. Trahey, L.; Brushett, F. R.; Balsara, N. P.; Ceder, G.; Cheng, L.; Chiang, Y.-M.; Hahn, N. T.; Ingram, B. J.; Minteer, S. D.; Moore, J. S.; Mueller, K. T.; Nazar, L. F.; Persson, K. A.; Siegel, D. J.; Xu, K.; Zavadil, K. R.; Srinivasan, V.; Crabtree, G. W., Energy

storage emerging: A perspective from the Joint Center for Energy Storage Research. *Proceedings of the National Academy of Sciences* **2020,** *117* (23), 12550-12557.

19. Harks, P. P. R. M. L.; Mulder, F. M.; Notten, P. H. L., In situ methods for Li-ion battery research: A review of recent developments. *J. Power Sources* **2015,** *288*, 92-105.
20. Deng, Z.; Lin, X.; Huang, Z.; Meng, J.; Zhong, Y.; Ma, G.; Zhou, Y.; Shen, Y.; Ding, H.; Huang, Y., Recent Progress on Advanced Imaging Techniques for Lithium-Ion Batteries. *Adv. Energy Mater.* **2021,** *11* (2), 2000806.
21. Kempaiah, R.; Vasudevamurthy, G.; Subramanian, A., Scanning probe microscopy based characterization of battery materials, interfaces, and processes. *Nano Energy* **2019,** *65*, 103925.
22. Qian, D.; Ma, C.; More, K. L.; Meng, Y. S.; Chi, M., Advanced analytical electron microscopy for lithium-ion batteries. *NPG Asia Materials* **2015,** *7* (6), e193-e193.
23. Yang, F.; Feng, X.; Liu, Y. S.; Kao, L. C.; Glans, P. A.; Yang, W.; Guo, J., In Situ/Operando (Soft) X-ray Spectroscopy Study of Beyond Lithium-ion Batteries. *ENERGY & ENVIRONMENTAL MATERIALS* **2021,** *4* (2), 139-157.
24. McBreen, J., The application of synchrotron techniques to the study of lithium-ion batteries. *J. Solid State Electrochem.* **2009,** *13* (7), 1051-1061.
25. Hu, J. Z.; Jaegers, N. R.; Hu, M. Y.; Mueller, K. T., In situ and ex situ NMR for battery research. *J. Phys.: Condens. Matter* **2018,** *30* (46), 463001.
26. Blanc, F.; Leskes, M.; Grey, C. P., In Situ Solid-State NMR Spectroscopy of Electrochemical Cells: Batteries, Supercapacitors, and Fuel Cells. *Acc. Chem. Res.* **2013,** *46* (9), 1952-1963.
27. Liu, X.; Liang, Z.; Xiang, Y.; Lin, M.; Li, Q.; Liu, Z.; Zhong, G.; Fu, R.; Yang, Y., Solid-State NMR and MRI Spectroscopy for Li/Na Batteries: Materials, Interface, and In Situ Characterization. *Adv. Mater.* **2021,** *33* (50), 2005878.
28. Liu, D.; Shadike, Z.; Lin, R.; Qian, K.; Li, H.; Li, K.; Wang, S.; Yu, Q.; Liu, M.; Ganapathy, S.; Qin, X.; Yang, Q. H.; Wagemaker, M.; Kang, F.; Yang, X. Q.; Li, B., Review of Recent Development of In Situ/Operando Characterization Techniques for Lithium Battery Research. *Adv. Mater.* **2019,** *31* (28), 1806620.
29. Tripathi, A. M.; Su, W.-N.; Hwang, B. J., *In situ* analytical techniques for battery interface analysis. *Chem. Soc. Rev.* **2018,** *47* (3), 736-851.

30. Fan, Q.; Ng, L. M., In Situ FTIR-ATR Study of p-Silicon Photoelectrode/Potassium Ferri-Ferrocyanide Electrolyte Interface. *J. Electrochem. Soc.* **1994**
141.
31. Pérez-Villar, S.; Lanz, P.; Schneider, H.; Novák, P., Characterization of a model solid electrolyte interphase/carbon interface by combined in situ Raman/Fourier transform infrared microscopy. *Electrochim. Acta* **2013,** *106*, 506-515.
32. Pekarek, R. T.; Affolter, A.; Baranowski, L. L.; Coyle, J.; Hou, T.; Sivonxay, E.; Smith, B. A.; McAuliffe, R. D.; Persson, K. A.; Key, B.; Apblett, C.; Veith, G. M.; Neale, N. R., Intrinsic chemical reactivity of solid-electrolyte interphase components in silicon–lithium alloy anode batteries probed by FTIR spectroscopy. *Journal of Materials Chemistry A* **2020,** *8* (16), 7897-7906.
33. Li, J.-T.; Chen, S.-R.; Ke, F.-S.; Wei, G.-Z.; Huang, L.; Sun, S.-G., In situ microscope FTIR spectroscopic studies of interfacial reactions of Sn–Co alloy film anode of lithium ion battery. *J. Electroanal. Chem.* **2010,** *649* (1-2), 171-176.
34. Lanz, P.; Novák, P., Combined In Situ Raman and IR Microscopy at the Interface of a Single Graphite Particle with Ethylene Carbonate/Dimethyl Carbonate. *J. Electrochem. Soc.* **2014,** *161* (10), A1555-A1563.
35. Lafont, U.; Carta, D.; Mountjoy, G.; Chadwick, A. V.; Kelder, E. M., In Situ Structural Changes upon Electrochemical Lithium Insertion in Nanosized Anatase TiO_2. *The Journal of Physical Chemistry C* **2010,** *114* (2), 1372-1378.
36. Hongyou, K.; Hattori, T.; Nagai, Y.; Tanaka, T.; Nii, H.; Shoda, K., Dynamic in situ fourier transform infrared measurements of chemical bonds of electrolyte solvents during the initial charging process in a Li ion battery. *J. Power Sources* **2013,** *243*, 72-77.
37. Ha, Y.; Tremolet De Villers, B. J.; Li, Z.; Xu, Y.; Stradins, P.; Zakutayev, A.; Burrell, A.; Han, S.-D., Probing the Evolution of Surface Chemistry at the Silicon–Electrolyte Interphase via In Situ Surface-Enhanced Raman Spectroscopy. *The Journal of Physical Chemistry Letters* **2020,** *11* (1), 286-291.
38. Ge, A.; Videla, P. E.; Lee, G. L.; Rudshteyn, B.; Song, J.; Kubiak, C. P.; Batista, V. S.; Lian, T., Interfacial Structure and Electric Field Probed by *in Situ* Electrochemical Vibrational Stark Effect Spectroscopy and Computational Modeling. *The Journal of Physical Chemistry C* **2017,** *121* (34), 18674-18682.

39. Sole, C.; Drewett, N. E.; Hardwick, L. J., In situ Raman study of lithium-ion intercalation into microcrystalline graphite. *Faraday Discuss.* **2014,** *172*, 223-237.

40. Inaba, M.; Yoshida, H.; Ogumi, Z.; Abe, T.; Mizutani, Y.; Asano, M., In Situ Raman Study on Electrochemical Li Intercalation into Graphite. *J. Electrochem. Soc.* **1995,** *142* (1), 20.

41. Alves Dalla Corte, D. Effects of surface chemical treatment on silicon negative electrodes for lithium-ion batteries: an in situ infrared spectroscopic study

Effets du traitement chimique de la surface d'une électrode négative en silicium amorphe pour batterie lithium-ion: étude par spectroscopie infrarouge in situ. Ecole Polytechnique X, 2013.

42. Kirwan, L. J.; Fawell, P. D.; Van Bronswijk, W., In Situ FTIR-ATR Examination of Poly(acrylic acid) Adsorbed onto Hematite at Low pH. *Langmuir* **2003,** *19* (14), 5802-5807.

43. Yang, J.; Solomatin, N.; Kraytsberg, A.; Ein-Eli, Y., In-SituSpectro-electrochemical Insight Revealing Distinctive Silicon Anode Solid Electrolyte Interphase Formation in a Lithium-ion Battery. *ChemistrySelect* **2016,** *1* (3), 572-576.

44. Ikezawa, Y.; Nishi, H., In situ FTIR study of the Cu electrode/ethylene carbonate+dimethyl carbonate solution interface. *Electrochim. Acta* **2008,** *53* (10), 3663-3669.

45. Wang, Z.; Tan, J.; Yang, Z.; Luo, Y.; Ye, S., Observing Two-Dimensional Spontaneous Reaction between a Silicon Electrode and a $LiPF_6$-Based Electrolyte *In Situ* and in Real Time. *The Journal of Physical Chemistry Letters* **2022,** *13* (14), 3224-3229.

46. Sharabi, R.; Markevich, E.; Borgel, V.; Salitra, G.; Aurbach, D.; Semrau, G.; Schmidt, M. A., In situ FTIR spectroscopy study of $Li/LiNi_{0.8}Co_{0.15}Al_{0.05}O_2$ cells with ionic liquid-based electrolytes in overcharge condition. *Electrochem. Solid-State Lett.* **2010,** *13* (4), A32.

47. Iwasita, T.; Nart, F. C., In situ infrared spectroscopy at electrochemical interfaces. *Prog. Surf. Sci.* **1997,** *55* (4), 271-340.

48. Teshager, M. A.; Lin, S. D.; Hwang, B. J.; Wang, F. M.; Hy, S.; Haregewoin, A. M., In Situ DRIFTS Analysis of Solid-Electrolyte Interphase Formation on Li-Rich Li1. 2Ni0. 2Mn0. $6O_2$ and $LiCoO_2$ Cathodes during Oxidative Electrolyte Decomposition. *ChemElectroChem* **2016,** *3* (2), 337-345.

49. Shi, F.; Ross, P. N.; Zhao, H.; Liu, G.; Somorjai, G. A.; Komvopoulos, K., A catalytic path for electrolyte reduction in lithium-ion cells revealed by in situ attenuated total reflection-Fourier transform infrared spectroscopy. *J. Am. Chem. Soc.* **2015,** *137* (9), 3181-3184.

50. Chazalviel, J.-N.; Erné, B. H.; Maroun, F.; Ozanam, F., In situ infrared spectroscopy of the semiconductor|electrolyte interface. *J. Electroanal. Chem.* **2001,** *509* (2), 108-118.
51. Shi, F.; Ross, P. N.; Somorjai, G. A.; Komvopoulos, K., The Chemistry of Electrolyte Reduction on Silicon Electrodes Revealed by in Situ ATR-FTIR Spectroscopy. *The Journal of Physical Chemistry C* **2017,** *121* (27), 14476-14483.
52. Song, H.-Y.; Fukutsuka, T.; Miyazaki, K.; Abe, T., In situ Raman investigation of electrolyte solutions in the vicinity of graphite negative electrodes. **2016,** *18* (39), 27486-27492.
53. Chazalviel, J. N.; Erné, B. H.; Maroun, F.; Ozanam, F., New directions and challenges in modern electrochemistry: in situ infrared spectroscopy of the semiconductor|electrolyte interface. **2001,** *502* (1-2), 180-190.
54. Bae, I. T.; Xing, X.; Yeager, E. B.; Scherson, D., Ionic transport effects in in situ Fourier-transform infrared reflection adsorption spectroscopy. *Anal. Chem.* **1989,** *61* (10), 1164-1167.
55. Ataka, K.-i.; Osawa, M., In Situ Infrared Study of Water−Sulfate Coadsorption on Gold(111) in Sulfuric Acid Solutions. *Langmuir* **1998,** *14* (4), 951-959.
56. Marinković, N. S.; Hecht, M.; Loring, J. S.; Fawcett, W. R., A sniftirs study of the diffuse double layer at single crystal platinum electrodes in acetonitrile. *Electrochim. Acta* **1996,** *41* (5), 641-651.
57. Webster, R. D., In situ electrochemical-ATR-FTIR spectroscopic studies on solution phase carboxylate radical anionsElectronic supplementary information (ESI) available: first derivative EPR spectra of radical anions. See http://www.rsc.org/suppdata/p2/b2/b206087f/. *Journal of the Chemical Society, Perkin Transactions 2* **2002,** (11), 1882-1888.
58. Xiao, C.; Goh, T. W.; Brashler, K.; Pei, Y.; Guo, Z.; Huang, W., In Situ X-ray Absorption Spectroscopy Studies of Kinetic Interaction between Platinum(II) Ions and UiO-66 Series Metal–Organic Frameworks. *The Journal of Physical Chemistry B* **2014,** *118* (49), 14168-14176.
59. Fan, Q.; Ng, L. M., In situ photoelectrochemical characteristics of the n-CdTe Iacetic acid solution interface by FTIR-ATR ". *Journal of ElectroanalyticalChemistry* **1995**, 7.
60. Visser, H.; Curtright, A. E.; McCusker, J. K.; Sauer, K., Attenuated Total Reflection Design for in Situ FT-IR Spectroelectrochemical Studies. *Anal. Chem.* **2001,** *73* (17), 4374-4378.

61. Morigaki, K.-I., In situ analysis of the interfacial reactions between MCMB electrode and organic electrolyte solutions. *J. Power Sources* **2002,** *103* (2), 253-264.
62. Venkateswara Rao, A.; Chazalviel, J. N.; Ozanam, F., In situ characterization of the n-Si/acetonitrile interface by electromodulated infrared internal-reflection spectroscopy. **1986,** *60* (2), 696.
63. Vivek, J. P.; Berry, N. G.; Zou, J.; Nichols, R. J.; Hardwick, L. J., In Situ Surface-Enhanced Infrared Spectroscopy to Identify Oxygen Reduction Products in Nonaqueous Metal–Oxygen Batteries. *The Journal of Physical Chemistry C* **2017,** *121* (36), 19657-19667.
64. Panitz, J.-C.; Joho, F.; Novak, P., In Situ Characterization of a Graphite Electrode in a Secondary Lithium-Ion Battery Using Raman Microscopy. *Appl. Spectrosc.* **1999,** *53* (10), 1188-1199.
65. Snellenburg, J. J.; Laptenok, S.; Seger, R.; Mullen, K. M.; van Stokkum, I. H. M., Glotaran: A Java-Based Graphical User Interface for the R Package TIMP. *J. Stat. Software* **2012,** *49* (3), 22.

Chapter 2. Background

This chapter will cover the background information related to the systems studied in this thesis. Initial emphasis will be placed on interfaces in LIBs – their components (electrode and electrolyte), conversion of in interface into an interphase, and a strategy for interfacial energetic tuning. Next, characterization and analysis tools will be introduced and explained for their relevance to this work including electrochemical methods, in situ infrared spectroelectrochemistry, and global analysis. This background will serve as the basis for the next two chapters.

2.1 LITHIUM-ION BATTERY INTERFACES

Interfaces are the most important part of any electrochemical device. Electrochemistry revolves around the process of moving charge from one phase to another to drive reduction-oxidation (redox) reactions.[1, 2] In a typical LIB, the interfaces in question are between the solid electrode and liquid electrolyte the properties of which dictate thermodynamics and kinetics of charge transfer. Researchers have been studying the dynamic nature of this interface for decades, yet questions still remain. The goal of this thesis is to monitor these processes and manipulate interfacial properties using surface modification. Specific focus will be given to the anode/electrolyte interface to simplify analysis and better understand fundamental processes. The following section will outline the components of this interface (electrode and electrolyte), define the formation of an interphase (SEI), and give an overview of tuning interfacial energetics.

2.1.1 ***LIB Electrodes***

The properties of lithium-ion battery electrodes are some of the largest deciding factors of performance for a given device. As described in section 1.2.2, LIB comprises two solid electrodes

– the cathode (positive electrode) and the anode (negative electrode). There exists an array of different commercially available cathode materials. The most common cathodes are oxides in one of the following structures: layered ($Li(M)O_2$), spinel (LiM_2O_4), or olivine ($Li(M)PO_4$), where M represents one or more transition metals.[3, 4] Cathode properties - such as energy density, cyclability, cost, safety, and power density - can be tuned due to the flexibility in exploring these different structures and transition metal compositions.[5] Commercial anodes, on the other hand, have been dominated by one material since the 1990s.

Graphite has dominated the commercial LIB anode industry for the last several decades owing to its moderate theoretical capacity (372 mAh/g), low cost, electrical conductivity and amazing cycling stability.[4] During a lithiation, lithium is stored in graphite via an intercalation mechanism. The ABABA stacking of the sp^2 hybridized graphene layers shifts slightly to accommodate the lithium ions and turns into AIAIA, where I is the interstitial layer.[6] This allows for a theoretical stoichiometric lithium storage mechanism that follows $Li + 6C \rightarrow LiC_6$.[7] While the market has been dominated by graphite for the last 30 years, there is a growing need to shift to materials with higher capacity to meet the needs of a growing energy storage landscape.

Silicon is a top candidate for a next-generation anode material due to its extremely high specific capacity (4200 mAh/g, i.e., more than a factor of ten increase over graphite), advantageous operating voltage (0.4V vs. Li/Li^+) and high natural abundance.[8] However, unlike graphite, silicon undergoes an alloying mechanism in which Li-Si bonds are formed with the most lithiated phase being $Li_{22}Si_5$ at elevated temperatures.[9] While the theoretical capacity is ten times greater than graphite, the commercial viability of silicon has been hindered by stability issues. These issues stem from the large volume expansion (~300%) that occurs during lithiation. This has several adverse effects that lead to detrimental instability: (1) expansion/contraction causes the electrode to lose contact with the copper current collector which leads to incomplete (de)lithiation (2) expansion/contraction pulverizes passivation layer (SEI), exposing bare active material which leads to continued growth of SEI decrease in reversible capacity.[10-13] Efforts to overcome these effects include, but are not limited to, optimizing silicon particle size,[14] crosslinking strategies for enhanced mechanical performance,[15-18] and electrolyte additives[19-22] for stable SEI formation.[23] The latter highlights the need to consider both sides of the interface when exploring next-generation materials. The next section will elaborate on the electrolyte.

2.1.2 *LIB Electrolyte*

The electrolyte in a LIB is another key component for dictating battery performance in and interfacial processes. The current lithium-ion batteries comprise a liquid electrolyte containing a lithium salt solute and a mix of anhydrous, aprotic solvents. In an ideal world, the electrolyte would be chemically inert within the LIB, only providing ionic flow through the system while Faradaic behavior takes place at the electrode.[24, 25] This, however, is not always the case as the operating voltage window between anode reduction and cathode oxidation often leads to electrolyte instability. The ideal properties of a LIB electrolyte are as follows: large electrochemical window to circumvent degradation due to the operating voltage of the system, be ionically conductive but electronically insulating to promote Li^+ transport between electrodes, chemically inert to the inactive materials within the battery (separator, housing components, etc), comprise environmentally friendly components, and be able to withstand thermal, electrical and mechanical stressors.[24]

While a wide array of electrolyte compositions have been explored for use in LIBs, the most common commercially available electrolyte uses lithium hexafluorophosphate ($LiPF_6$) in a mix cyclic (ethylene carbonate, EC) and linear (i.e., dimethyl carbonate [DMC], diethyl carbonate [DEC], ethyl methyl carbonate [EMC]) carbonates. The choice of these components was the best compromise achieved to accommodate the properties stated above for commercially available LIBs using graphite anodes and oxide cathodes. $LiPF_6$ has high ionic conductivity compared to the handful of other available lithium salts ($LiAsF_6 > LiPF_6 > LiClO_4 > LiBF_4$).[26] While $LiPF_6$ has poor thermal stability and has undesirable decomposition products (HF), it has emerged as the salt of choice from this list due to environmental (poisonous As), safety (explosive $LiClO_4$) and stability (unstable passivation layer from $LiBF_4$).[24-27]

Electrolyte solvents are ideally aprotic (proton reduction occurs within the electrochemical window of the LIB), have low viscosity to promote ion motion, are chemically inert in a wide electrochemical window and have a high enough dielectric constant to dissolve the lithium salt.[25] The mixed carbonate solvent system commercially used today represents another compromise of these requirements. Cyclic ethylene carbonate (EC) is advantageous due to its large dielectric constant and resulting ability to dissociate lithium salt. However, its high viscosity and high melting point inhibit ion conductivity. As a result, linear alkyl carbonate such as DMC is mixed with EC to lower the viscosity of the electrolyte. While this solvent system comes at a safety price (highly flammable) it currently monopolizes the commercial electrolyte landscape due to its incredible stability. This stability is dictated by the inevitable interfacial reactions at the anode during lithation. Decomposition of the electrolyte is inevitable at the anode surface and are influenced by composition and ion speciation within the system.[28-31] These processes are discussed further in the following section.

2.1.3 ***Solid-Electrolyte Interphase (SEI)***

While the ideal anode/electrolyte interface would remain chemically inert, this is unfortunately not the case for the conventional electrolytes discussed above. Anode lithiation occurs under extreme reductive conditions (below 0.5V vs. Li/Li^+) which is enough to drive electrochemical decomposition of both $LiPF_6$ and the carbonate solvents (EC, DMC, FEC, etc.). During the first lithiation cycle, these irreversible decomposition reactions occur at the surface of the silicon anodes and form a passivating layer known as the solid-electrolyte interphase.[1, 32-34] The desired traits for this layer are that it is (1) ionically conductive so Li^+ can migrate reversibly through it to be stored in the active material and (2) electronically insulating to prevent further electrolyte reduction.[1, 25, 33-35] The stability and success of a LIB is dependent on the performance of the SEI. The technological world as we know it today was revolutionized by the discovery that switching from propylene carbonate (PC) to ethylene carbonate (EC) was the deciding factor for SEI stability the graphite anode surface.[30, 36-39] As discussed in section 2.1.1, SEI stability in silicon electrodes suffers greatly due to volume expansion/contraction during charge, leading to extreme capacity fade. Chapter 4 will propose a strategy for mitigating these effects via tuning interfacial energetics.

2.1.4 *Tuning Interfacial Energetics*

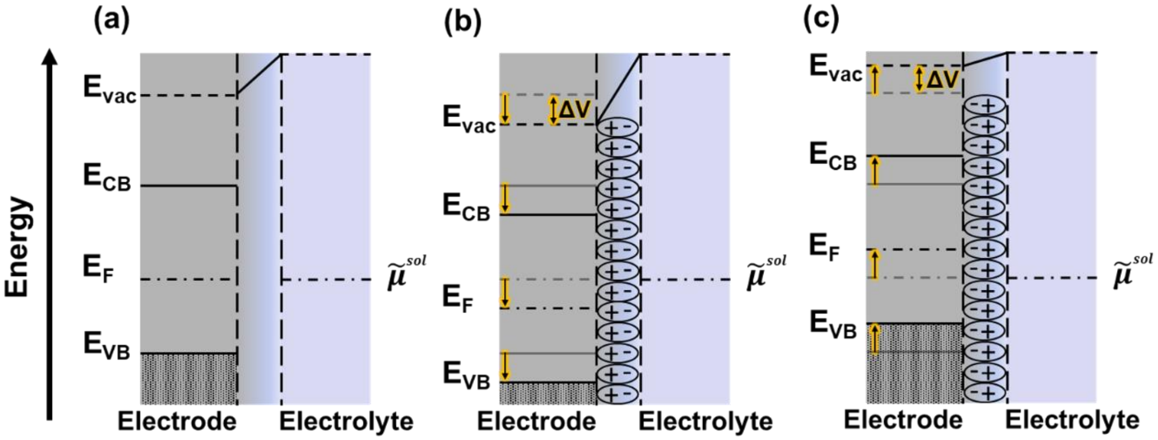

Figure 2.1. Tuning interfacial energetics using dipole surface modification.

Dipole surface modification has been explored as a tool for tuning interfacial energetics of semiconductor devices such as photovoltaic solar cells, electronic devices, field effect transistors and more.[40-47] The addition of a dipole layer on the surface shifts the electrode's energy levels with respect to the electrochemical potential of the electrolyte. Equation 2.1 shows the dependence of the potential drop across the dipole layer (ΔV) on surface density of dipoles (N), dipole moment strength (μ), effective dielectric constant of layer (ϵ), permittivity of free space (ϵ_0) and the tilt angle of the dipolar moiety in relation to the surface (θ).[40, 46, 47]

$$\Delta V = \frac{N\mu \cos\theta}{\epsilon\epsilon_0} \tag{2.1}$$

Figure 2.1a illustrates the energy diagram for the electrode/electrolyte interface with no dipole modification. When the dipole is pointed away from the surface, there is more charge density farther from the surface which lowers the band energies (Figure 2.1b). Alternatively, when the dipole is pointed towards the surface, charge density is larger closer to the electrode which pushes the band energies higher (Figure 2.1c). We note that when the dipoles are pointed outward (Figure 2.1b), the Fermi energy (E_F) in the electrode is driven lower than the electrochemical potential of the electrolyte ($\tilde{\mu}^{sol}$), therefore making it thermodynamically more difficult to reduce the electrolyte. Since we know from the above section that electrolyte reduction is unwanted in our LIB system, we hypothesize that this could be a powerful tool for mitigating this process when using group IV semiconductor anodes. Further study of this hypothesis is discussed in Chapter 4.

2.2 ELECTROCHEMICAL CHARACTERIZATION OF LITHIUM-ION BATTERIES

Electrochemical characterization is ubiquitous in the LIB research community. To study fundamental properties and isolate effects from one electrode, it is common to investigate half cells. That is, rather than using a typical oxide cathode material, we use lithium metal as the positive electrode (cathode). This allows us to reference the electrochemical processes to the Li/Li+ redox couple. Since our fundamental studies are performed on the bench scale, we use a 2032 coin cell form factor which will differ from larger, application-scale form factors. As such, our results are meant to inform future design rules, rather than suggest a plug and play improvement.

Galvanostatic cycling tests are some of the most powerful tools for studying battery performance. This entails applying a constant current calculated to drive a voltage change and achieve the theoretical specific capacity of the material being charged (4200 mAh/g for Si). Typically, a slow charge/discharge rate (C/20, i.e., one charge over the course of 20 hours) is programmed for the first cycle to enable robust SEI formation before switching to a faster rate for long term cycling (C/10 common for Si). Specific capacity as a function of cycle number is often used to visualize battery performance. To assess cycling stability, capacity retention is calculated by normalizing to the first cycle after the SEI formation step. This is due to the inevitable irreversible capacity loss that occurs when the SEI is formed. The differential capacity (dQ/dV) as a function of cell voltage reports on the phase changes occurring during electrochemical charge and discharge cycles. This allows us to monitor the evolution of these phases over the course of long-term cycling and correlate them with performance trends from capacity retention plots. Lastly, the coulombic efficiency (CE) is a measure of the charge transfer efficiency of the coin cells. This is calculated by taking the ratio of discharge capacity to charge capacity and is used as a marker for the reversibility.

The final electrochemical characterization tool that will be discussed in this work is electrochemical impedance spectroscopy (EIS). Briefly, EIS measures the sinusoidal current or voltage response of a cell at steady state that has been exposed to an AC voltage or AC current, respectively, over a range of frequencies. This is a transfer function tool that can be used to separate processes occurring at different time constants. From equivalent circuit modeling, we can monitor differences in resistive and capacitive components. This metric will be useful for comparing electrostatic contributions from dipole modifiers to these cell components in Chapter 4.

2.3 IN SITU VIBRATIONAL SPECTROELECTROCHEMISTRY

2.3.1 *Vibrational Spectroscopy Principles*

Infrared spectroscopy is a powerful tool for measuring molecular vibrations. The number of vibrational modes in a molecule is defined by 3N degrees of freedom based on the number of atoms it possesses (N). Accounting for three translational and three rotational motions, a nonlinear molecule has 3N-6 vibrational modes. One rotational degree of freedom is lost for linear molecules, resulting in the 3N-5. Depending on the degree of variation in potential energy as a function of atomic displacement (r) from their equilibrium position (bottom of the well), the transition can be approximated by a harmonic potential (Hooke's law) or an anharmonic potential (Morse type), as seen in Figure 2.2.[48]

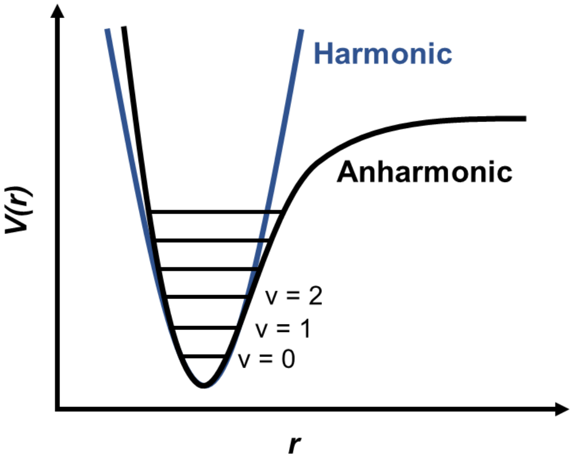

Figure 2.2. Representative plot of diatomic molecule with harmonic (blue) and anharmonic (black) oscillator potential wells and energy levels. Potential energy V(r) as a function of atomic displacement from equilibrium (r).

Selection rules dictate whether a vibrational mode can be measured by FTIR. The first requirement is that the transition dipole moment ($\frac{\partial\mu}{\partial r}$) of the vibrational mode must be non-zero. at a resonant frequency to the electromagnetic (EM) excitation light. The transition between vibrational states (v = 0, 1, 2, etc.) is only accomplished when the transition dipole moment of the molecule can absorb resonant incoming EM radiation. Therefore, if there is no change in dipole moment for a given vibrational mode, there will be no absorption. If a mode is purely harmonic, the vibrational energy will follow Equation 2.2, where v_i is the vibrational quantum number of the i^{th} mode, $\hbar$ is Planck's constant / 2π, and ω is 2π × frequency. Under this approximation, the only allowed transition is $\Delta v_i \pm 1$ and is known as a fundamental transition. If the displacement of the atoms does not satisfy the harmonic model, an anharmonic (Morse) potential function approximation is used (Equation 2.3, where x_i is dimensionless anharmonicity constant). This allows for transitions of $\Delta v_i > 1$, known as overtone and combination bands.

$$V_i = \hbar\omega(v_i + \tfrac{1}{2}) \qquad (2.2)$$

$$V_i = \hbar\omega\left(v_i + \frac{1}{2}\right) + \hbar\omega x_i \left(v_i + \frac{1}{2}\right)^2 \qquad (2.3)$$

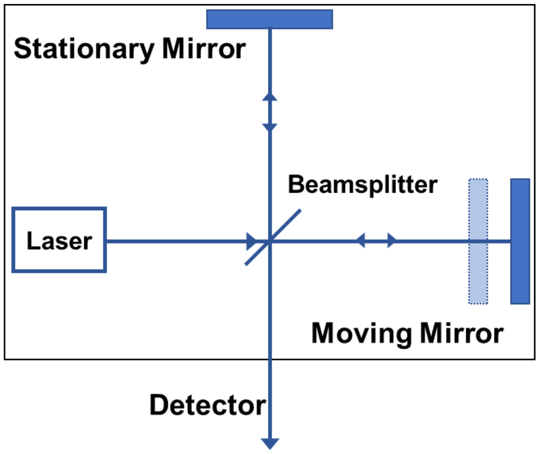

Figure 2.3. Michelson interferometer components including laser, beamsplitter, stationary and moving mirrors and detector.

Fourier-transform infrared (FTIR) spectroscopy is a technique that uses a Michelson interferometer to measure the vibrational modes discussed above. This is a device comprising a laser, beamsplitter, stationary and moving mirror, and detector (Figure 2.3). A beam of IR light from the laser is split into two paths – one to the stationary mirror and one to the moving mirror. The moving mirror creates a difference between the two paths which recombine back at the beamsplitter and create an interference pattern which is sent to the detector. For FTIR spectroscopy, the interference beam containing a variety of frequencies is passed through the sample and the resulting intensity ($I(\delta)$) as a function of path difference (δ) is detected. This interferogram is then converted via Fourier transform to intensity ($B(v)$) as a function of frequency (v) using Equation 2.4.[49]

$$B(v) = \int I(\delta) e^{i2\pi\delta v} d\delta \tag{2.4}$$

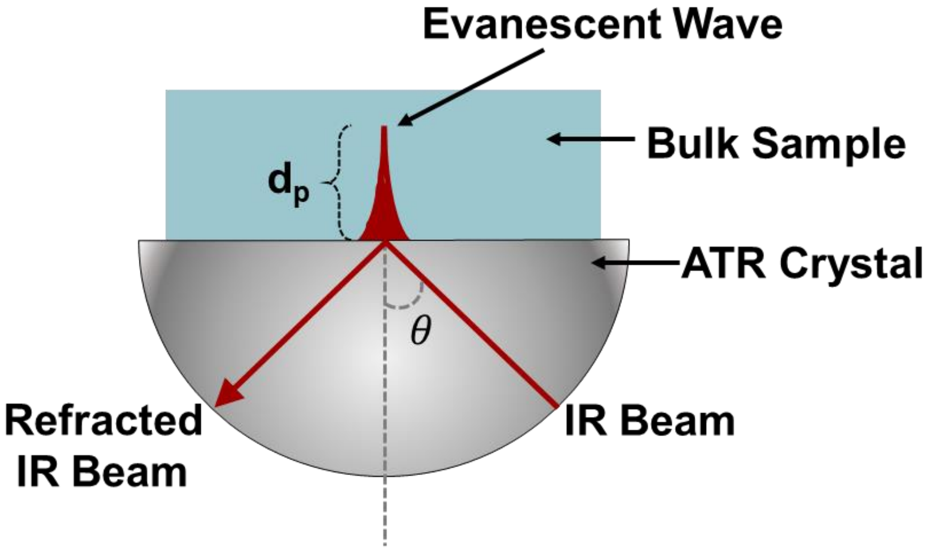

Figure 2.4. Single beam attenuated total reflectance (ATR) diagram.

While there exist many sampling methods for FTIR spectroscopy including but not limited to transmission, specular reflection and diffuse reflection, the work presented in this thesis will focus on attenuated total reflectance (ATR). During this method, as shown in Figure 2.4, an IR beam is refracted through an ATR crystal with a high refractive index (n_1), such as germanium (Ge), silicon (Si) or diamond (to name a few) at a certain angle of incidence (θ). When this beam hits the interface of the sample, with a smaller refractive index (n_2), an electric field extends orthogonally to the surface of the ATR crystal. This electric field is referred to as the evanescent wave. The evanescent wave extends into the sample with a penetration depth (d_p) defined in Equation 2.5.

$$d_p = \frac{\lambda}{2\pi(n_1^2 sin^2(\theta) - n_2^2)^{1/2}} \tag{2.5}$$

2.3.2 *In situ Vibrational Spectroelectrochemistry Cell Design*

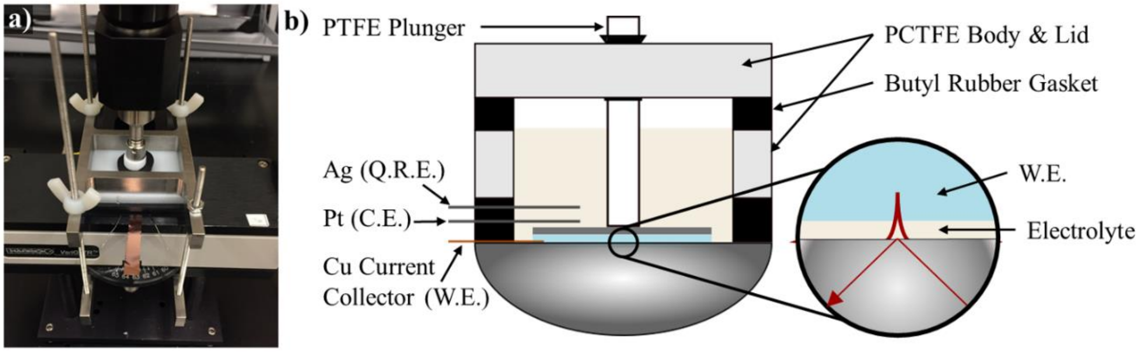

Figure 2.5. (a) Picture of air-free in situ vibrational spectroelectrochemical cell designed and built for potential-dependent ATR-FTIR measurements of model system ATR accessory. (b) Cross-sectional scheme of the interior of the sample cell.

We designed and fabricated a custom air-free electrochemical cell which contained a layer of electrolyte sandwiched between the working electrode (W.E.) and the Ge ATR element (Figure 2.5). The electrode was compressed onto the Ge using a Teflon^{TM} (PTFE, polytetrafluoroethylene) plunger and a piece of copper wire was used as a current collector to make connection with the TiO_2 electrode. The platinum (Pt) counter electrode (C.E.) and silver (Ag) quasi-reference electrode (Q.R.E) were inserted into the cell through a butyl rubber gasket. This was all encased in a Kel-F$^{®}$ (PCTFE, polychlorotifluoroethylene) body and lid with butyl rubber to ensure an air-tight seal. The cell was assembled in an argon-filled MBraun glove box.

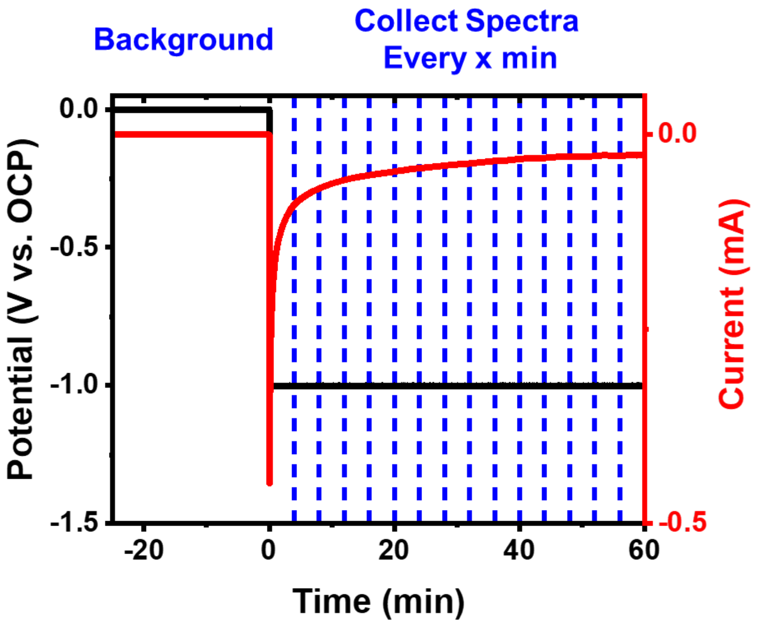

Figure 2.6. In situ FTIR spectroelectrochemical measurement protocol

Figure 2.6 illustrates the measurement protocol used for the in situ measurements using the cell described above. A background spectrum of the sample was measured using the FTIR spectrometer at open circuit potential (OCP) after an hour of equilibration time. The remaining difference spectra (blue dashed lines) were referenced to the OCP background. A chronoamperometric potential step of -1.0V away from OCP was applied to the cell and used to trigger the collection of the FTIR spectra every x minutes (x = 4 or 8 depending on instrument settings). Because of the experimental limitations of mass transport through our thin electrolyte layer, we will analyze the relative timescales for changes occurring as a result of the applied potential, rather than absolute times.

2.4 GLOBAL ANALYSIS

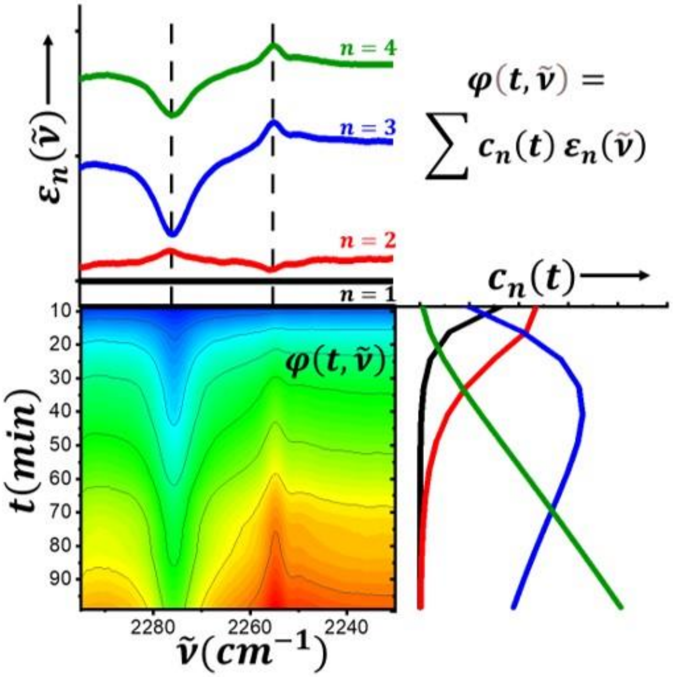

Figure 2.7. Visual representation of the global target analysis fitting matrix. Our time-resolved data (bottom left) is represented as a superposition of n components, each containing distinct energy-dependent spectral species (top left). These species are weighted by a time-dependent concentration profile (bottom right).

Global target analysis was performed using Glotaran, a graphical user interface for the R-package TIMP, to model our time-resolved ATR-FTIR spectroelectrochemical data.[50] This method, commonly used by spectroscopists, provides a quantitative measure of how spectrally active species evolve over time. We input our time-resolved FTIR data set and, using the model described below, recover kinetically-distinct spectra which are referred to as Species Associates Difference Spectra (SADS). Each SADS includes components for all vibrational reporters that evolve with a common time constant, allowing us to draw kinetic correlations between the dynamics for solvation, ion pairing and electron accumulation. This information would otherwise be lost without the use of this method due to the qualitative nature of the FTIR measurement.

We modeled the time-resolved data with a matrix (φ) defined by the superposition of n components, each containing a distinct energy-dependent spectral species ($\varepsilon_n(\tilde{\nu})$) (Figure 2.7, top left) comprising vibrational reporters which share the same time constant, otherwise known as SADS. These independent spectral species are weighted by a time-dependent concentration profile ($c_n(t)$) (Figure 2.7, bottom right), which illustrate how they are evolving over time. These kinetically-distinct spectra, or SADS, carry units of molar absorptivity. The time-resolved data set is defined by Equation 2.6[50]:

$$\varphi(t, \tilde{\nu}) = \sum c_n(t)\, \varepsilon_n(\tilde{\nu}) \tag{2.6}$$

The typical analysis model used in our analysis was a unidirectional, unbranched model (example shown in Figure A.1). As stated above, the mass transport limitations of our cell design lead us to analyze relative kinetics, rather than absolute. Therefore, we define the species as Initial, Fast, Medium and Slow. In this type of model, the initial species is populated by the initial change in speciation due to the applied potential, as recorded by the first spectrum. This species subsequently decays into the Fast which decays into the Medium which decays into the Slow which relaxes back to equilibrium. This will allow us to make relative kinetic correlations between various vibrational reporters within the systems being studied.

2.5 REFERENCES

1. Xu, K., Interfaces and interphases in batteries. *J. Power Sources* **2023,** *559,* 232652.
2. Bard, A. J.; Faulkner, L. R., *Electrochemical methods : fundamentals and applications*. Second edition. ed.; John Wiley & Sons, Inc.: Hoboken, NJ, 2001.
3. Manthiram, A., A reflection on lithium-ion battery cathode chemistry. *Nature Communications* **2020,** *11* (1).

4. Li, J.; Fleetwood, J.; Hawley, W. B.; Kays, W., From Materials to Cell: State-of-the-Art and Prospective Technologies for Lithium-Ion Battery Electrode Processing. *Chem. Rev.* **2022,** *122* (1), 903-956.
5. Stallard, J. C.; Wheatcroft, L.; Booth, S. G.; Boston, R.; Corr, S. A.; De Volder, M. F. L.; Inkson, B. J.; Fleck, N. A., Mechanical properties of cathode materials for lithium-ion batteries. *Joule* **2022,** *6* (5), 984-1007.
6. McKinnon, W.; Haering, R., Modern aspects of electrochemistry. *Plenum Press: New York* **1983,** *15*, 235.
7. Yazami, R.; Touzain, P., A reversible graphite-lithium negative electrode for electrochemical generators. *J. Power Sources* **1983,** *9* (3), 365-371.
8. Zhang, W.-J., A review of the electrochemical performance of alloy anodes for lithium-ion batteries. *J. Power Sources* **2011,** *196* (1), 13-24.
9. Nzereogu, P. U.; Omah, A. D.; Ezema, F. I.; Iwuoha, E. I.; Nwanya, A. C., Anode materials for lithium-ion batteries: A review. *Applied Surface Science Advances* **2022,** *9*, 100233.
10. Shi, F.; Song, Z.; Ross, P. N.; Somorjai, G. A.; Ritchie, R. O.; Komvopoulos, K., Failure mechanisms of single-crystal silicon electrodes in lithium-ion batteries. *Nature Communications* **2016,** *7* (1), 11886.
11. Ryu, J. H.; Kim, J. W.; Sung, Y.-E.; Oh, S. M., Failure Modes of Silicon Powder Negative Electrode in Lithium Secondary Batteries. *Electrochem. Solid-State Lett.* **2004,** *7* (10), A306.
12. McDowell, M. T.; Lee, S. W.; Nix, W. D.; Cui, Y., 25th Anniversary Article: Understanding the Lithiation of Silicon and Other Alloying Anodes for Lithium-Ion Batteries. *Adv. Mater.* **2013,** *25* (36), 4966-4985.
13. Obrovac, M. N.; Chevrier, V. L., Alloy Negative Electrodes for Li-Ion Batteries. *Chem. Rev.* **2014,** *114* (23), 11444-11502.
14. Liu, X. H.; Zhong, L.; Huang, S.; Mao, S. X.; Zhu, T.; Huang, J. Y., Size-Dependent Fracture of Silicon Nanoparticles During Lithiation. *ACS Nano* **2012,** *6* (2), 1522-1531.
15. Eshetu, G. G.; Figgemeier, E., Confronting the Challenges of Next-Generation Silicon Anode-Based Lithium-Ion Batteries: Role of Designer Electrolyte Additives and Polymeric Binders. *ChemSusChem* **2019,** *12* (12), 2515-2539.

16. Deng, L.; Zheng, Y.; Zheng, X.; Or, T.; Ma, Q.; Qian, L.; Deng, Y.; Yu, A.; Li, J.; Chen, Z., Design Criteria for Silicon-Based Anode Binders in Half and Full Cells. *Adv. Energy Mater.* **2022,** *12* (31), 2200850.
17. Jung, C.-H.; Kim, K.-H.; Hong, S.-H., Stable Silicon Anode for Lithium-Ion Batteries through Covalent Bond Formation with a Binder via Esterification. *ACS Appl. Mater. Interfaces* **2019,** *11* (30), 26753-26763.
18. Chen, S.; Song, Z.; Wang, L.; Chen, H.; Zhang, S.; Pan, F.; Yang, L., Establishing a Resilient Conductive Binding Network for Si-Based Anodes via Molecular Engineering. *Acc. Chem. Res.* **2022,** *55* (15), 2088-2102.
19. Zhang, S. S., A review on electrolyte additives for lithium-ion batteries. *J. Power Sources* **2006,** *162* (2), 1379-1394.
20. Song, S.-W.; Baek, S.-W., Silane-Derived SEI Stabilization on Thin-Film Electrodes of Nanocrystalline Si for Lithium Batteries. *Electrochem. Solid-State Lett.* **2009,** *12* (2), A23.
21. Aupperle, F.; Von Aspern, N.; Berghus, D.; Weber, F.; Eshetu, G. G.; Winter, M.; Figgemeier, E., The Role of Electrolyte Additives on the Interfacial Chemistry and Thermal Reactivity of Si-Anode-Based Li-Ion Battery. *ACS Appl. Energy Mater.* **2019,** *2* (9), 6513-6527.
22. Wang, J.; Zhang, L.; Zhang, H., Effects of electrolyte additive on the electrochemical performance of Si/C anode for lithium-ion batteries. *Ionics* **2018,** *24* (11), 3691-3698.
23. Xu, K.; Von Cresce, A., Interfacing electrolytes with electrodes in Li ion batteries. *J. Mater. Chem.* **2011,** *21* (27), 9849.
24. Xu, K., Nonaqueous Liquid Electrolytes for Lithium-Based Rechargeable Batteries. *Chem. Rev.* **2004,** *104* (10), 4303-4418.
25. Xu, K., Electrolytes and Interphases in Li-Ion Batteries and Beyond. *Chem. Rev.* **2014,** *114* (23), 11503-11618.
26. Liu, Y. K.; Zhao, C. Z.; Du, J.; Zhang, X. Q.; Chen, A. B.; Zhang, Q., Research Progresses of Liquid Electrolytes in Lithium-Ion Batteries. *Small* **2023,** *19* (8), 2205315.
27. Aurbach, D.; Talyosef, Y.; Markovsky, B.; Markevich, E.; Zinigrad, E.; Asraf, L.; Gnanaraj, J. S.; Kim, H.-J., Design of electrolyte solutions for Li and Li-ion batteries: a review. *Electrochim. Acta* **2004,** *50* (2-3), 247-254.

28. Raguette, L.; Jorn, R., Ion Solvation and Dynamics at Solid Electrolyte Interphases: A Long Way from Bulk? *The Journal of Physical Chemistry C* **2018,** *122* (6), 3219-3232.
29. Fulfer, K. D.; Kuroda, D. G., Ion speciation of lithium hexafluorophosphate in dimethyl carbonate solutions: an infrared spectroscopy study. *Physical Chemistry Chemical Physics* **2018,** *20* (35), 22710-22718.
30. Xu, K.; Lam, Y.; Zhang, S. S.; Jow, T. R.; Curtis, T. B., Solvation sheath of Li+ in nonaqueous electrolytes and its implication of graphite/electrolyte interface chemistry. *J. Phys. Chem. C* **2007,** *111* (20), 7411-7421.
31. Xu, K.; Lam, Y.; Zhang, S. S.; Jow, T. R.; Curtis, T. B., Solvation Sheath of Li+in Nonaqueous Electrolytes and Its Implication of Graphite/Electrolyte Interface Chemistry. *The Journal of Physical Chemistry C* **2007,** *111* (20), 7411-7421.
32. Peled, E., The Electrochemical Behavior of Alkali and Alkaline Earth Metals in Nonaqueous Battery Systems—The Solid Electrolyte Interphase Model. *J. Electrochem. Soc.* **1979,** *126* (12), 2047.
33. Peled, E.; Menkin, S., Review—SEI: Past, Present and Future. *J. Electrochem. Soc.* **2017,** *164* (7), A1703-A1719.
34. Peled, E.; Golodnitsky, D.; Penciner, J., The Anode/Electrolyte Interface. In *Handbook of Battery Materials*, Daniel, C.; Besenhard, J. O., Eds. Wiley-VCH Verlag GmbH & Co. KGaA: Weinheim, Germany, 2011; pp 479-523.
35. Kim, J.; Chae, O. B.; Lucht, B. L., Perspective—Structure and Stability of the Solid Electrolyte Interphase on Silicon Anodes of Lithium-ion Batteries. *J. Electrochem. Soc.* **2021,** *168* (3), 030521.
36. Wagner, M. R.; Albering, J. H.; Moeller, K. C.; Besenhard, J. O.; Winter, M., XRD evidence for the electrochemical formation of Li+(PC)yCn- in PC-based electrolytes. *Electrochem. Commun.* **2005,** *7* (9), 947-952.
37. Agubra, V. A.; Fergus, J. W., The formation and stability of the solid electrolyte interface on the graphite anode. *J. Power Sources* **2014,** *268*, 153-162.
38. Dey, A.; Sullivan, B., The electrochemical decomposition of propylene carbonate on graphite. *J. Electrochem. Soc.* **1970,** *117* (2), 222.
39. Xu, K.; von Wald Cresce, A., Li+-solvation/desolvation dictates interphasial processes on graphitic anode in Li ion cells. *J. Mater. Res.* **2012,** *27* (18), 2327-2341.

40. Guijarro, N.; Prévot, M. S.; Sivula, K., Surface modification of semiconductor photoelectrodes. *Physical Chemistry Chemical Physics* **2015,** *17* (24), 15655-15674.
41. Zojer, E.; Taucher, T. C.; Hofmann, O. T., The Impact of Dipolar Layers on the Electronic Properties of Organic/Inorganic Hybrid Interfaces. *Advanced Materials Interfaces* **2019,** *6* (14), 1900581.
42. Vilan, A.; Cahen, D., Chemical Modification of Semiconductor Surfaces for Molecular Electronics. *Chem. Rev.* **2017,** *117* (5), 4624-4666.
43. Otero, R.; Vázquez de Parga, A. L.; Gallego, J. M., Electronic, structural and chemical effects of charge-transfer at organic/inorganic interfaces. *Surf. Sci. Rep.* **2017,** *72* (3), 105-145.
44. Chen, Q.; Wang, C.; Li, Y.; Chen, L., Interfacial Dipole in Organic and Perovskite Solar Cells. *J. Am. Chem. Soc.* **2020,** *142* (43), 18281-18292.
45. Paniagua, S. A.; Giordano, A. J.; Smith, O. N. L.; Barlow, S.; Li, H.; Armstrong, N. R.; Pemberton, J. E.; Brédas, J.-L.; Ginger, D.; Marder, S. R., Phosphonic Acids for Interfacial Engineering of Transparent Conductive Oxides. *Chem. Rev.* **2016,** *116* (12), 7117-7158.
46. Ashkenasy, G.; Cahen, D.; Cohen, R.; Shanzer, A.; Vilan, A., Molecular Engineering of Semiconductor Surfaces and Devices. *Acc. Chem. Res.* **2002,** *35* (2), 121-128.
47. Yang, S.; Prendergast, D.; Neaton, J. B., Tuning Semiconductor Band Edge Energies for Solar Photocatalysis via Surface Ligand Passivation. *Nano Lett.* **2012,** *12* (1), 383-388.
48. Griffiths, P. R.; De Haseth, J. A.; Winefordner, J. D., *Fourier Transform Infrared Spectrometry*. Wiley: 2007.
49. Bates, J. B., Fourier Transform Infrared Spectroscopy. *Science* **1976,** *191* (4222), 31-37.
50. Snellenburg, J. J.; Laptenok, S.; Seger, R.; Mullen, K. M.; van Stokkum, I. H. M., Glotaran: A Java-Based Graphical User Interface for the R Package TIMP. *J. Stat. Software* **2012,** *49* (3), 22.

Chapter 3. Ion-Pairing Dynamics Revealed by Kinetically Resolved In Situ FTIR Spectroelectrochemistry during Lithium-Ion Storage

Reprinted (adapted) with permission from. ACS Appl. Mater. Interfaces 2021, 13 (41), 48546-48554. Copyright 2021 American Chemical Society.

3.1 OVERVIEW

To begin our study of LIB interfaces, a model system was chosen investigate kinetic correlations between electron accumulation in the electrode and ion speciation in the electrolyte. Understanding the kinetics of interfacial ion speciation could inform battery designs. However, this knowledge gap persists, largely due to the challenge of experimentally interrogating the evolution of ions near electrode interfaces in a sea of bulk signals. We report here the very first kinetically-resolved correlation between interfacial ion speciation and lithium-ion storage in a model system, by applying global analysis to in situ attenuated total reflectance (ATR) Fourier-Transform infrared (FTIR) spectroelectrochemical data. Our results suggest that it may be more kinetically viable for lithium to be extracted from contact ion pairs (CIPs) to contribute to faster electrode charging compared to fully-solvated lithium. As the search for fast charging lithium-ion batteries and supercapacitors wages on, this discovery suggests that manipulating the ion pairing within the electrolyte could be one effective strategy for promoting faster charging kinetics.

3.2 INTRODUCTION

Lithium-ion batteries (LIB) have revolutionized the technological world as we know it today. After over 30 years of research in the field, LIBs have become a ubiquitous energy storage system for our personal electronics and beyond. Perhaps most importantly, as the fight against climate change wages on, the world has begun a shift toward electric vehicles (EV). In accordance with the International Energy Agency's Sustainable Development Scenario (SDS), the number of electric vehicles (EVs) sold globally must increase 20-fold by 2030 to meet the emission goals set by the Paris Agreement.[1] To achieve this goal, LIB must reach higher energy densities and faster rate capabilities for cheaper prices to assuage consumer anxiety about the transition of traditional gasoline-powered vehicles.[1]

LIBs comprise three main components: electrolyte, negative electrode (anode), and positive electrode (cathode). The primary role of the electrolyte is to provide sufficient ion conductivity so that lithium ions (Li^+) can be easily shuttled between the two electrodes during charge and discharge cycles. Additionally, the properties of the electrolyte dictate the irreversible products formed on the surface of the negative electrode, called the solid electrolyte interphase (SEI).[2] While considerable effort has been made towards understanding these electrolyte characteristics the last several decades, the exact nature of interfacial speciation at the electrode/electrolyte interface remains an open question. Due to difficulties in resolving interfacial measurements, it has proven quite challenging to probe the ion speciation at the electrode/electrolyte junction. In this paper, we aim to shed light on this problem using an approach to kinetically correlate charge storage and ion dynamics.

Perhaps one of the most dramatic examples of how much influence speciation in the electrolyte can have played out in the historical development of modern LIB technologies, when the researcher field recognized the importance of switching from propylene carbonate-based (PC) to ethylene carbonate-based (EC) electrolyte solutions. After multiple years of attempting to achieve reversible lithiation of graphite, it was discovered that graphite exfoliation (rather than stable SEI formation) occurs as the result of the decomposition of the PC solvent.[3, 4] Quite remarkably, the removal of one methyl group resulted in the battery industry as we know it today. The shift to EC introduced completely new interfacial properties which mitigated exfoliation and allowed a stable SEI to form.[5-9] This demonstrates the transformational impact that one seemingly insignificant chemical modification in the electrolyte speciation can have on the overall viability of the technology.

Ion solvation at the electrode/electrolyte interface plays a huge role in the performance of charge storage systems in LIBs and beyond. In 2007, Xu et al. discovered that the inner solvation sheath of the lithium cations plays a direct role in the formation of the SEI.[10, 11] In later years, they revealed that the desolvation of lithium ions dictates the kinetics of charging a graphite electrode at ambient and low temperatures. [12, 13] Strategies such as introducing weakly solvating electrolytes, mixing solvents for preferential solvation, and additives have been employed to manipulate the solvation environment and influence battery performance. [14-16]

The discussion of electrolyte structure is incomplete without considering ion association. As concentration of the electrolyte increases, lithium begins to associate with the counterion to form contact ion pairs (CIPs), solvent-separated ion pairs (SSIPs) and aggregates.[17] This occurs on the concentration scale of commercially used electrolytes (~1M) and even more so in the search for next-generation super-concentrated electrolytes (~3-5M).[18] Considerable theoretical and experimental efforts have elucidated the importance of the interplay between solvation and ion association, including the influence on properties such as viscosity and conductivity.[19-28] Multiple groups have used ultra-fast spectroscopy to investigate fundamental properties which include preferential ion pairing with mixed solvents, molecular motions and geometries of acetonitrile within the first solvation shell of Li^+, and a non-rigid cation interaction between solvent molecules and counterions.[29-31] More recent research results highlight the influence ion pairing can have on interfacial processes within a battery. In the search for a multivalent cation to replace lithium as a next generation battery, researchers have discovered that ion pairing and cluster formation lead to more electroactive species which enhance reversibility and ion permittivity and lead to an unexpected increase in ionic conductivity.[32-34] It is our goal to better understand the influence of ion pairing on the charging dynamics of a model system relevant to LIBs and beyond. Herein, for the first time, we correlate interfacial ion speciation with charge storage dynamics during an anode charging cycle by applying global target analysis. This approach allows us to kinetically resolve individual vibrational fingerprints, for example, those of contact ion pairs vs. solvated lithium, from in situ IR spectroelectrochemical measurements.

Historically, our research laboratory has studied interfacial processes of next-generation, high-capacity conversion electrodes such as silicon (Si) and germanium (Ge) using sum-frequency generation (SFG). The overarching goal of our work revolves around gaining a fundamental understanding of the processes occurring within a battery to inform future design. We have successfully monitored interfacial reactions during the formation of the SEI on a Si negative electrode, defined electric field properties of battery electrolytes and investigated the nature of the influence of surface modifying Ge nanowires.[35-37] Throughout the course of these studies, two main problems have become apparent in the systems chosen: 1) volume expansion of conversion electrodes influenced the types of measurements available and 2) the SFG technique limited the scope of experiments due sample degradation. In particular, to avoid laser ablation, we were limited to collecting vibrational SFG signatures only before or after we had applied a DC electrode potential, but not during the charge or discharge profile. In this work, we aim to circumvent these issues by choosing a well-defined model electrode and a vibrational spectroelectrochemical technique that can be performed *during* charging, without damaging the sample.

We selected a model system to study the effects of ion speciation during lithiation of a negative electrode. The electrolyte is 1M lithium perchlorate ($LiClO_4$) in acetonitrile (ACN). While this is not a commercial LIB electrolyte formulation, it provides robust, IR-active vibrational signatures that can serve as reporters for ion pairing and solvation without interference from intensity-burrowing Fermi resonances that organic carbonates exhibit. Acetonitrile is a solvent often used for low-voltage charge storage systems such as electrochemical supercapacitors.[38] We use the symmetrical nitrile stretch of lithium-coordinated acetonitrile (Li-ACN) as a marker for solvation dynamics during lithiation of the negative electrode.[39] The lower frequency asymmetric perchlorate stretch is used as a reporter for the ion pairing in solution, as the perchlorate signature reflects the concentration of perchlorate in direct contact with lithium (CIPs).[40]

We chose an anatase titanium dioxide (TiO_2) sol gel film to use as a model electrode. While TiO_2 is not a commercially viable negative electrode material, it is a reliable testbed to monitor ion speciation because it allows us to circumvent ill-defined structural evolution (e.g., silicon volume expansion) and SEI formation. As such, the results of this study, not only lay the groundwork for future discoveries related to ion speciation at advanced battery electrode interfaces, but they also carry implications for applications ranging from supercapacitors to dye sensitized solar cells. Titania-based (TiO_2) negative electrodes are an attractive model system to study due to their safety, capacity retention, fast Li^+ transport kinetics and negligible volume expansion.[41] However, low theoretical capacity, poor electrical conductivity and low ionic diffusivity have obstructed their commercial viability. Nevertheless, advanced understanding of the kinetic competition between various ion speciation during electrochemical processes at TiO_2

interfaces will not only serve to overcome these obstacles but also benefit numerous scientific fields.

Operando vibrational Fourier-Transform infrared (FTIR) spectroelectrochemistry has been a powerful tool for studying ion speciation, adsorption, and SEI formation.[42-49] Our experimental design employs an external reflection geometry for *in situ* attenuated total reflectance (ATR) FTIR spectroelectrochemistry that reduces the signal amplitude from the bulk electrolyte (Figure 2.5). To suppress bulk electrolyte absorption, we utilize a thin solution layer of electrolyte in contact with the electrode. This design aspect of our home-built cell allows us to measure the ion speciation markers as they evolve in response to an applied potential across the electrode/electrolyte interface.[50] While the form factor for our measurement allows us to suppress bulk absorption, diffusion limitations only allow us to characterize the relative charging rate associated with one ionic species compared with another. Additionally, we are unable to deconvolute any spectral features for SSIPs, limiting analysis to CIPs only.

Herein, we couple *in situ* vibrational spectroelectrochemistry with global target analysis to gain kinetic information during a lithiation cycle. To the best of our knowledge, this is the very first kinetically-resolved spectral analysis of ion speciation during charging ever to be reported for any lithium storage material. We use vibrational reporters to probe CIP dissociation, desolvation of lithium and electron accumulation of the model TiO_2/ACN system. After collecting a time-resolved FTIR spectral data set during a lithiation cycle of the TiO_2 electrode, we then use global target analysis to deconvolute spectra and allow for kinetic correlations between speciation and charge storage. Our results indicate lithium-ion extraction from CIPs is kinetically correlated with electrode charging at early times, while electrode charging at later times is correlated with the removal of fully-solvated lithium from the electrolyte. Our findings suggest that manipulating ion speciation of the electrolyte, specifically by controlling the dynamics of CIPs, could promote faster charging. In the search for fast-charging LIBs for use in EVs and beyond, this result could be far-reaching and help inform future electrolyte design.

3.3 EXPERIMENTAL METHODS

Reagents. Lithium perchlorate (battery grade, dry, 99.99%), tetrabutylammonium perchlorate (≥ 99.0%), acetonitrile (anhydrous, 99.8%), titanium(IV) isopropoxide (≥ 97.0%), nitric acid (ACS reagent, 70%) were purchased from Sigma-Aldrich. Polyethylene glycol 2000 was purchased from TCI America. All reagents were used as received without further purification.

TiO_2 Electrode Preparation. An anatase TiO_2 sol-gel electrode was fabricated using a procedure previously reported in literature.[51] In a 200-mL three neck round bottom flask, 0.42 mL 70% nitric acid was added to 60 mL of deionized (DI) water. To this, 10 mL titanium isopropoxide was added dropwise over the course of ten minutes. This was heated to 80 ºC for about 8 hours with two necks left open to air. The resulting semi-transparent solution was cooled to room temperature and the appropriate amount of DI to achieve a concentration of 150 g TiO_2 per liter. Five milliliters of this solution were then heated to 200 ºC in a Teflon-lined autoclave for 12 hours. The cooled TiO_2 was added to 0.3 g of melted polyethylene glycol 2000 and was stirred for 6-8 hours. Using a doctor blade, the solution was spread across a clean indium tin oxide (ITO) substrate (1cm x 1cm slide, supported on glass) with a Scotch tape mask. Once the film of TiO_2 turned from opaque to transparent, the substrate was placed on a 450 ºC hot plate for 30 minutes. Electrodes were either used immediately or stored in a vacuum oven.

In Situ FTIR Spectroelectrochemical Measurement and Analysis. *In situ* vibrational ATR spectroelectrochemical measurements were performed using an FTIR spectrometer (Nicolet

8700) and a potentiostat (Autolab PGSTAT302N). The ATR-FTIR experiments used a mercury cadmium telluride (MCT) detector with a spectral range of 650 cm^{-1} to 3500 cm^{-1}, resolution of 0.5 cm^{-1} and 128 scans. Infrared light passes through the ATR element at an angle of 63.5° and the resulting evanescent wave penetrates between roughly 200-800 nm into the ACN layer in contact with the TiO_2, depending on the wavenumber. See Section 2.3.2 for a description of the air-free *in situ* cell and measurement protocol. For this study, spectra were collected every 8 min.

The *in situ* ATR-FTIR spectroelectrochemical time-resolved data set was fit to an unbranched, unidirectional model with four kinetically distinct spectral species that decay sequentially with increasing time (Figure A.1). The initial species is populated by the speciation change due to the initial applied potential and subsequently decays into the **Fast** species with a time constant of τ_{fast}. The **Fast** species decays into the **Medium** (τ_{medium}), the **Medium** into the **Slow** (τ_{slow}), and the **Slow** back to equilibrium. Data was not collected for the process of re-equilibration, so the **Slow** species represents the longest-lived species but does not provide quantitative information regarding the re-equilibration process. See Section 2.4 for more information about global analysis.

3.4 RESULTS AND DISCUSSION

We start by assigning vibrational signatures as reporters for solvation and ion pairing. It has been well established that ACN strongly coordinates Li^+, resulting in a blue shift of the nitrile vibrational stretch from 2253 cm^{-1} (**Bulk ACN**) to 2276 cm^{-1} (**Li-ACN**), shown in Figure 3.1a.[39] This lithium-coordinated acetonitrile (**Li-ACN**) peak will be used as the reporter for the first solvation shell of the lithium in solution.[40] Perchlorate offers analogous vibrational spectroscopic reporters, though slightly more complicated. The formation of CIPs between Li^+ and ClO_4^- breaks the degeneracy of the free ClO_4^- species, leading to a frequency shift of the asymmetric perchlorate band proportional to the polarizability of the cation.[40] A total of five bands contribute to the overall spectral shape for perchlorate between 1200-1000 cm^{-1}. Of these five bands shown in Figure 3.1b, three (1, 2 and 5) are associated with CIPs formed by the direct interaction between Li$^+$ and ClO_4^- and two are associated with free, unpaired perchlorate (3 and 4). There is still a debate in the literature as to the nature of peaks 2 and 4, owing either to the formation of isotopomers or a change in solvation number.[40, 52] To simplify analysis, we will focus on the primary peaks for paired (**Paired ClO_4^-**, peak 1, 1134 cm^{-1}) and unpaired perchlorate (**Unpaired ClO_4^-**, peak 3, 1102 cm^{-1}). These will serve as vibrational reporters for the association and dissociation of ion pairs.

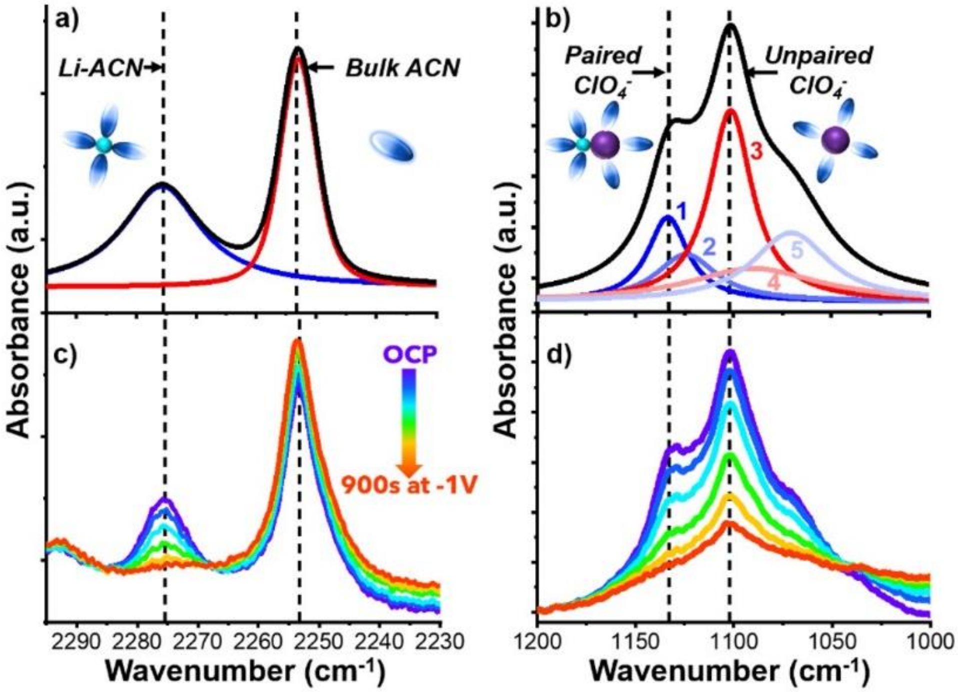

Figure 3.1. (a) Nitrile stretch (solvation reporter) of 1.0 M $LiClO_4$ in acetonitrile (ACN) at open circuit potential (OCP). ACN coordinates to Li+ causing a blue shift of nitrile peak. Free nitrile stretch appears at 2253 cm^{-1} and coordinated nitrile appears at 2276 cm^{-1}, providing a signature for solvation. (b) Perchlorate stretch (ion pairing reporter) of 1.0 M $LiClO_4$ in ACN at OCP. This is a convolution of multiple peaks corresponding to paired and unpaired anions. For the purposes of simplifying analysis, our focus will be on the most prominent peaks for paired (1134 cm^{-1}) and unpaired (1102 cm^{-1}) perchlorate. When a potential of -1 V (vs OCP) is applied

to 1.0 M $LiClO_4$ in ACN using the in situ cell described in Figure 2.5, the concentration of coordinated (solvated)/ uncoordinated ACN (c) and paired/unpaired perchlorate (d) changes at the electrode/electrolyte interface. Spectra for (c) and (d) were collected at a time interval of ~150 s and serve as a qualitative representation of the change in species concentration due to applied potential.

It has been well established that the peaks defined above are influenced by changes in concentration. [39, 40] As $LiClO_4$ concentration increases, the intensity of the peaks for **Li-ACN** and **Paired ClO_4^-** increase. It is expected that the ion speciation concentration profile of the electrical double layer across the electrode/electrolyte interface will change in response to the applied voltage during the lithiation of our TiO_2 electrode. As a potential of -1.0 V away from open circuit potential (OCP) is applied to our sample, it is observed that both solvation (**Li-ACN**) and ion pairing (**Paired ClO_4^-**) evolve over a period of 900s, collected at an interval of ~150 s (Figure 3.1c and Figure 3.1d). The spectra show an expected decrease in **Li-ACN** and the entire perchlorate spectral envelope (paired and unpaired) during lithiation. Each spectral region represents the convolution of multiple peaks, which makes it difficult to discern by simple visual inspection how all vibrational reporters are changing over the course of this experiment. Fortunately, we can gain quantitative information about the data in Figure 3.1c and Figure 3.1d using global target analysis which allows us to kinetically resolve spectral species evolving with the same time constant and reveal a more detailed picture.

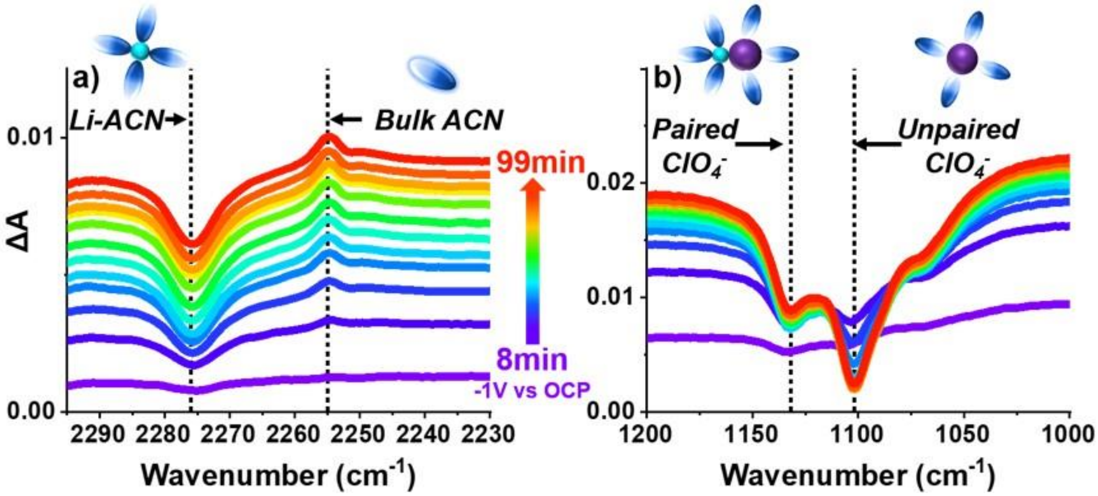

Figure 3.2. Time-resolved in situ ATR-FTIR spectroelectrochemistry data of (a) solvation (Li-ACN) signature and (b) ion pairing (Paired ClO_4^-) signature. Referenced against OCP, these data represent the difference in interfacial speciation due to an applied potential of -1V (vs. OCP). Spectra were collected every 8 minutes over a 99 minute window.

To better understand the underlying ion speciation across the interface due to applied potential, spectra were collected every 8 minutes of a period of 99 minutes to produce a more robust time-resolved dataset. Spectra were referenced versus OCP and collected every 8 minutes over a period of 99 min. The plots shown in Figure 3.2 were collected as difference spectra referenced to OCP meaning all peaks represent conditions of the system away from equilibrium that appear because of the applied potential across the interface. Positive peaks correspond to increased concentration of a species while and negative peaks correspond to a decrease in concentration. Qualitative analysis of this data set follows the expectation that lithium intercalation or pseudocapacitive charging[53] of the TiO_2 electrode result at the expense of the desolvation of lithium (decrease in **Li-ACN**) and the dissociation of lithium from CIP (decrease in **Paired ClO_4^-**). Further analysis is required to better understand how the ion speciation dynamics are changing over time.

While it is necessary for the desolvation of lithium and dissociation of contact ion pairs to occur to balance charge at the electrode, the kinetics of these processes are not readily apparent. One might anticipate that electron accumulation associated with extracting Li$^+$ from contact ion pairs may proceed prior to that associated with extracting Li$^+$ from within their full solvation shell due to the thermodynamic comparison of the solvation energy of Li-ACN$_4$ (-295 kJ/mol) and Li-ClO$_4$ ion association energy (-9.1 kJ/mol).[52, 54]

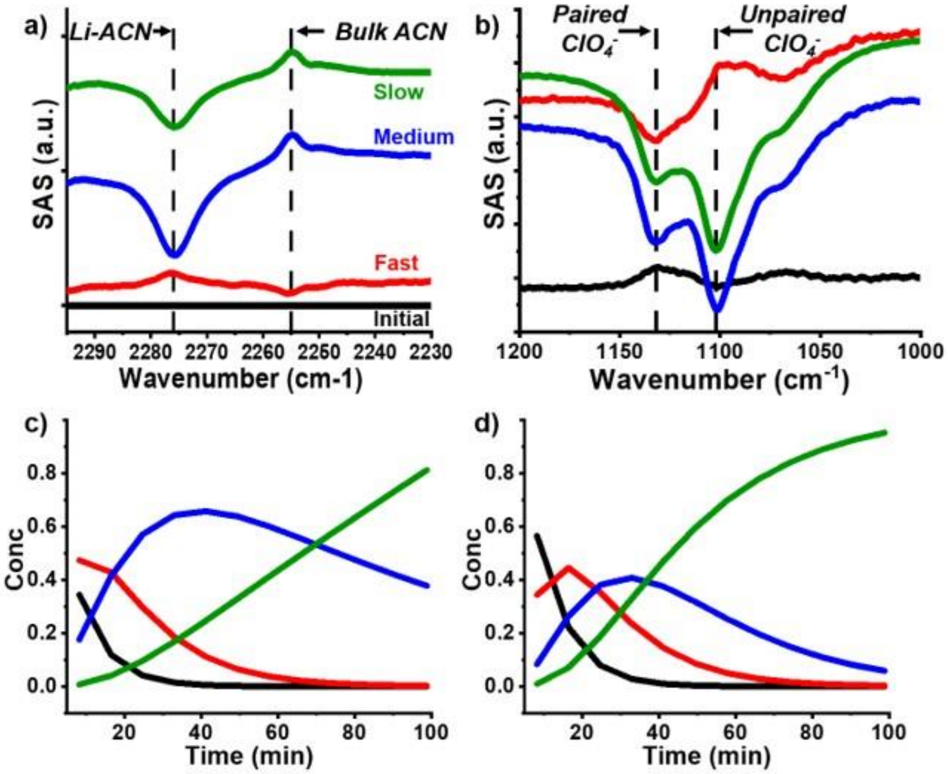

Figure 3.3. Species associated difference spectra (SADS) resulting from global target analysis of the time-resolved data for the (a) nitrile (solvation reporter) and (b) perchlorate (ion pairing reporter) vibrational stretches. SADS comprise vibrational signatures which are either enriched (positive peak) or depleted (negative peak) with the same time constant. The y-axis defined as SADS carries units of molar absorptivity. Concentration profiles of each SADS for the nitrile (a) and perchlorate (b) with respect to time are shown in (c) and (d), respectively.

Global target analysis was used to successfully fit the two spectral regions of interest (nitrile and perchlorate) to the same sequential model. The resulting Species Associated Difference Spectra (SADS) for each region (Figure 3.3a and Figure 3.3b) elucidate the vibrational signatures which are either enriched (positive peak) or depleted (negative peak) for each kinetically-distinct regime. For example, the SADS labeled **Fast** represent the solvation (Figure 3.3a) and ion pairing (Figure 3.3b) reporters which are evolving with the same time constant (τ_{fast}). This allows us to draw kinetic correlations between ion speciation processes that occur at the same time. The concentrations of moieties that contribute to these SADS evolve over the course of the experiment, which is depicted by the time-dependent concentration profiles shown in Figure 3.3c and Figure 3.3d.

The initial state (black), populated due to the applied potential across the interface, decays sequentially into the **Fast** (red) species at a rate of τ_{fast} = 8 min which decays into the **Medium** (blue) species (τ_{medium} = 14 min) which decays into the **Slow** (green) species (τ_{slow} =78 min) (Figure A.1). Analysis of this result will begin with the vibrational resonances for nitrile and perchlorate stretches, the origin of the baseline shifts will be discussed below. At the fastest timescale, we observe that the concentration of **Paired ClO_4^-** decreases and **Unpaired ClO_4^-** increases which suggests fast dissociation of contact ion pairs. On this same timescale, we see a corresponding increase in the concentration of **Li-ACN**, suggesting competitive solvation of the vacant coordination site on the lithium dissociated from the CIP. This suggests that there is an initial fast dissociation of contact ion pairs resulting in an increase of unpaired perchlorate and solvated lithium ions. This is followed by two kinetic regimes **Medium** and **Slow** that both kinetically correlate to an overall decrease of perchlorate anion (paired and unpaired) with the loss of solvated lithium. This result supports the hypothesis that during a lithiation cycle at the negative electrode, a fast dissociation of contact ion pairs is followed by slower desolvation of lithium. This suggests that it may be more kinetically viable for lithium to be extracted from CIPs to contribute to faster electrode charging compared to that of fully-solvated lithium. Further analysis of electron accumulation in the electrode is required to correlate the kinetics of the vibrational resonances for ion pairing and solvation with the rates of electron accumulation while charging the anode.

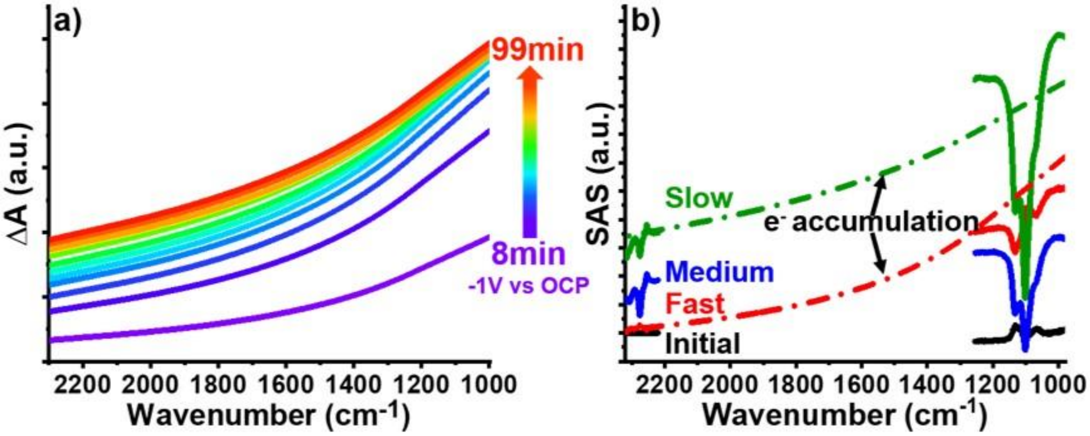

Figure 3.4. (a) Power laws were fit to the baseline of each spectrum of the time-resolved data set to represent the electron accumulation within the TiO_2 electrode. (b) Global target analysis of the power law fits resolved two kinetic SADS for the electron accumulation, Fast and Slow. When overlaid with the SADS for the vibrational resonances of solvation and ion pairing, we reveal a kinetic correlation between ion speciation across the interface and charge storage. No electron accumulation species was found to match the Medium kinetic trace, indicating that the rise in its baseline is due to a frequency independent shift.

As we lithiate the anode by applying a negative potential, free electrons are accumulated in the TiO_2 electrode. As electrons are injected into the conduction band of a semiconductor, the material exhibits a continuum of intraband absorption signatures that appear in the mid-IR.[55] Correspondingly, the absorbance for the electron accumulation (α) is present as a structureless, broad feature with increasing amplitude in the low-energy region of the spectrum, following a power law defined as $\alpha = A\tilde{\nu}^{p}$, where p ranges from -3.5 to -1.5 depending on the type of interaction occurring to conserve momentum.[55] This signature has been observed for anatase TiO_2 with photoinduced[56] and electrochemical[57] electron accumulation. The electron accumulation signature for our time-resolved vibrational data set was fit to the power law defined above for each time trace. The fitting results are depicted in Figure 3.4a with values for p ranging between -2.2 and -1.2.

To correlate the electron accumulation signature with the vibrational reporters for solvation and ion pairing, we modeled the time-dependent evolution of our power law fits using the same global analysis fitting routine. The fit suggests that there are two kinetic regimes for electron accumulation during charge storage in the TiO_2 electrode. To accurately compare the amplitude of the solvation and ion pairing signatures, the concentration-weighted spectral profiles were overlaid with the SADS for the electron accumulation. This revealed that the **Fast** and **Slow** time constants are kinetically correlated with charge storage (Figure 3.4b). Interestingly, no unique individual species associated spectral component for the overall electron accumulation signature could be kinetically correlated with the **Medium** kinetic regime that we observe for the nitrile and perchlorate vibrational signatures. We attribute the rise in amplitude for the **Medium** trace to a frequency independent baseline shift due to the applied potential. While the origin of this is unknown, we observe a similar baseline shift that does not follow the same power law character as the electron accumulation signature when tetrabutylammonium (TBA^+) is substituted for Li^+ (Figure A.3). Because TBA^+ cannot compensate the injected charge, the electron accumulation signature does not appear and instead we observe a frequency independent baseline shift, analogous to that we observe for the **Medium** trace.

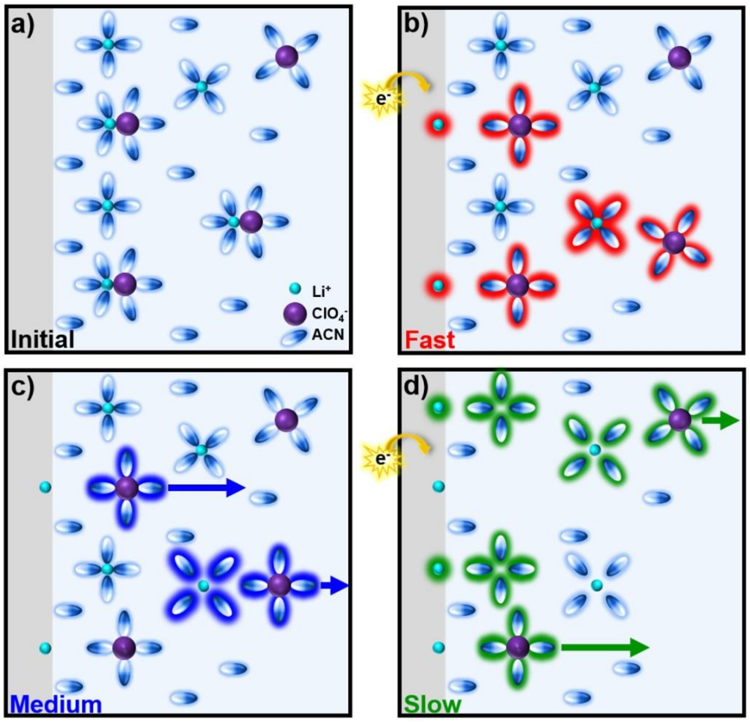

Figure 3.5. (a) Initial organization of interfacial electrolyte species due to applied potential across the interface. (b) Fast time scale dissociation of CIPs kinetically correlated with the initial electron accumulation in the electrode. (c) Medium time scale re-equilibration desolvation of lithium and loss of all perchlorate (paired and unpaired) forms intermediate state which is independent of electron accumulation. (d) Slow time scale charge storage resulting as a consequence of desolvated lithium.

The results shown in Figure 3.4b support the hypothesis that it is kinetically more facile to charge compensate stored electrons on the anode by extracting lithium from CIPs rather than fully-solvated lithium. The initial state (Figure 3.5a) due to the applied potential decays to the **Fast** kinetic regime (Figure 3.5b) which corresponds to the dissociation of CIPs and fast electron accumulation (charge storage) in the electrode. This is followed by a **Medium** kinetic regime (Figure 3.5c) that we speculate is a re-equilibration period which is independent of electron accumulation in the electrode. In this step, the perchlorate anion (paired and unpaired) appears to be drawn away from the working electrode/solution interface, presumably toward the counter electrode, along with some re-equilibration of the lithium-ion solvation environment that does not appear to correlate with electron accumulation on the TiO_2. Once re-equilibration has occurred, the continued desolvation of lithium (decrease in **Li-ACN**) is correlated with a second electron accumulation species in the **Slow** kinetic regime (Figure 3.5d).

The fast charging kinetics that we observe for paired lithium-ions appear surprising at first glance, since bulk ion pair transport to the electrode in an electric field is generally considered to be sluggish and therefore undesirable compared to free ions.[2] One explanation for this observation in kinetically-resolved optical signatures evidentially arises from the fact that our *in situ* measurement geometry preferentially surveys the response of species confined within regions responsive only to an applied voltage (i.e. diffusion layer and double layer) and, to a considerable extent, suppresses much of the background bulk solvent response. This suggests that the ion speciation environment, and specifically the nature of the ion pairing, could have huge implications for manipulating the kinetics of interfacial charge storage. As the search for fast charging LIBs wages on, our results suggest that manipulating the ion pairing within the electrolyte could be one effective strategy for promoting faster charging kinetics in LIBs.

3.5 CONCLUSIONS

Ion speciation of the electrolyte is one of the most pivotal characteristics of a lithium-ion battery. Recalling our discussion of the switch from PC to EC, it is evident that even minor alterations in the electrolyte speciation can dictate the success of lithium-ion batteries. The nature of ion pairing within the electrolyte appears to have a much larger influence on the system than was originally considered, influencing fundamental properties, and cycling behavior.[19-34] Herein we present kinetic correlations between ion dynamics and charge storage in a model system that adds another piece of information to this puzzle. *In situ* ATR-FTIR spectroelectrochemical measurements coupled with global target analysis reveal that lithium ions extracted from contact ion pairs are kinetically correlated with fast charge storage of the negative electrode. This is followed by a slower process of desolvating lithium to store charge. This finding suggests that a manipulation of the contact ion pairing environment within a battery electrolyte could have a significant influence on rate capabilities. We can use this type of study as a building block to begin to investigate ways to engineer the ion speciation of the electrolyte to promote faster kinetics for ion storage and mitigate unwanted electrochemical solvent/electrolyte reduction. Further application-based studies are underway in our laboratory to determine if increasing the concentration of contact ion pairs will result in enhanced cycling rate performance.

3.6 REFERENCES

1. IEA *Global EV Outlook 2021*; Paris, 2021; pp 1-97.
2. Xu, K., Nonaqueous Liquid Electrolytes for Lithium-Based Rechargeable Batteries. *Chem. Rev.* **2004,** *104* (10), 4303-4418.
3. Dey, A.; Sullivan, B., The electrochemical decomposition of propylene carbonate on graphite. *J. Electrochem. Soc.* **1970,** *117* (2), 222.
4. Wagner, M. R.; Albering, J. H.; Moeller, K. C.; Besenhard, J. O.; Winter, M., XRD evidence for the electrochemical formation of Li+(PC)yCn- in PC-based electrolytes. *Electrochem. Commun.* **2005,** *7* (9), 947-952.
5. Fong, R.; Von Sacken, U.; Dahn, J. R., Studies of lithium intercalation into carbons using nonaqueous electrochemical cells. *J. Electrochem. Soc.* **1990,** *137* (7), 2009.
6. Winter, M.; Besenhard, J. O.; Spahr, M. E.; Novak, P., Insertion electrode materials for rechargeable lithium batteries. *Adv. Mater.* **1998,** *10* (10), 725-763.

7. Agubra, V. A.; Fergus, J. W., The formation and stability of the solid electrolyte interface on the graphite anode. *J. Power Sources* **2014,** *268*, 153-162.
8. Verma, P.; Maire, P.; Novák, P., A review of the features and analyses of the solid electrolyte interphase in Li-ion batteries. *Electrochim. Acta* **2010,** *55* (22), 6332-6341.
9. Xu, K., Whether EC and PC differ in interphasial chemistry on graphitic anode and how. *J. Electrochem. Soc.* **2009,** *156* (9), A751.
10. Xu, K., “Charge-transfer” process at graphite/electrolyte interface and the solvation sheath structure of Li+ in nonaqueous electrolytes. *J. Electrochem. Soc.* **2007,** *154* (3), A162.
11. Xu, K.; Lam, Y.; Zhang, S. S.; Jow, T. R.; Curtis, T. B., Solvation sheath of Li+ in nonaqueous electrolytes and its implication of graphite/electrolyte interface chemistry. *J. Phys. Chem. C* **2007,** *111* (20), 7411-7421.
12. Li, Q.; Lu, D.; Zheng, J.; Jiao, S.; Luo, L.; Wang, C.-M.; Xu, K.; Zhang, J.-G.; Xu, W., Li^+-Desolvation Dictating Lithium-Ion Battery’s Low-Temperature Performances. *ACS Appl. Mater. Interfaces* **2017,** *9* (49), 42761-42768.
13. Xu, K.; von Wald Cresce, A., Li+-solvation/desolvation dictates interphasial processes on graphitic anode in Li ion cells. *J. Mater. Res.* **2012,** *27* (18), 2327-2341.
14. Yao, Y. X.; Chen, X.; Yan, C.; Zhang, X. Q.; Cai, W. L.; Huang, J. Q.; Zhang, Q., Regulating Interfacial Chemistry in Lithium-Ion Batteries by a Weakly Solvating Electrolyte**. *Angew. Chem.* **2020,** *133* (8), 4136-4143.
15. Seo, D. M.; Reininger, S.; Kutcher, M.; Redmond, K.; Euler, W. B.; Lucht, B. L., Role of Mixed Solvation and Ion Pairing in the Solution Structure of Lithium Ion Battery Electrolytes. *J. Phys. Chem. C* **2015,** *119* (25), 14038-14046.
16. Zhang, S. S., Design aspects of electrolytes for fast charge of Li-ion batteries. *InfoMat* **2021,** *3* (1), 125-130.
17. Marcus, Y.; Hefter, G., Ion Pairing. *Chem. Rev.* **2006,** *106* (11), 4585-4621.
18. Borodin, O.; Self, J.; Persson, K. A.; Wang, C.; Xu, K., Uncharted Waters: Super-Concentrated Electrolytes. *Joule* **2020,** *4* (1), 69-100.
19. Seo, D. M.; Borodin, O.; Han, S.-D.; Ly, Q.; Boyle, P. D.; Henderson, W. A., Electrolyte solvation and ionic association. *J. Electrochem. Soc.* **2012,** *159* (5), A553.

20. Seo, D. M.; Borodin, O.; Han, S.-D.; Boyle, P. D.; Henderson, W. A., Electrolyte solvation and ionic association II. Acetonitrile-lithium salt mixtures: highly dissociated salts. *J. Electrochem. Soc.* **2012,** *159* (9), A1489.
21. Seo, D. M.; Borodin, O.; Balogh, D.; O'Connell, M.; Ly, Q.; Han, S.-D.; Passerini, S.; Henderson, W. A., Electrolyte solvation and ionic association III. Acetonitrile-lithium salt mixtures–transport properties. *J. Electrochem. Soc.* **2013,** *160* (8), A1061.
22. Han, S.-D.; Borodin, O.; Allen, J. L.; Seo, D. M.; McOwen, D. W.; Yun, S.-H.; Henderson, W. A., Electrolyte solvation and ionic association: IV. Acetonitrile-lithium difluoro (oxalato) borate (LiDFOB) mixtures. *J. Electrochem. Soc.* **2013,** *160* (11), A2100.
23. Han, S.-D.; Borodin, O.; Seo, D. M.; Zhou, Z.-B.; Henderson, W. A., Electrolyte solvation and ionic association: V. Acetonitrile-lithium bis (fluorosulfonyl) imide (LiFSI) mixtures. *J. Electrochem. Soc.* **2014,** *161* (14), A2042-A2053.
24. Borodin, O.; Han, S.-D.; Daubert, J. S.; Seo, D. M.; Yun, S.-H.; Henderson, W. A., Electrolyte Solvation and Ionic Association: VI. Acetonitrile-Lithium Salt Mixtures: Highly Associated Salts Revisited. *J. Electrochem. Soc.* **2015,** *162* (4), A501-A510.
25. Henderson, W. A.; Seo, D. M.; Han, S.-D.; Borodin, O., Electrolyte Solvation and Ionic Association. VII. Correlating Raman Spectroscopic Data with Solvate Species. *J. Electrochem. Soc.* **2020,** *167* (11), 110551-110558.
26. Lucht, B. L.; Collum, D. B., Ethereal Solvation of Lithium Hexamethyldisilazide: Unexpected Relationships of Solvation Number, Solvation Energy, and Aggregation State. *J. Am. Chem. Soc.* **1995,** *117* (39), 9863-9874.
27. Chapman, N.; Borodin, O.; Yoon, T.; Nguyen, C. C.; Lucht, B. L., Spectroscopic and Density Functional Theory Characterization of Common Lithium Salt Solvates in Carbonate Electrolytes for Lithium Batteries. *J. Phys. Chem. C* **2017,** *121* (4), 2135-2148.
28. Lucht, B. L.; Collum, D. B., Lithium Hexamethyldisilazide: A View of Lithium Ion Solvation through a Glass-Bottom Boat. *Acc. Chem. Res.* **1999,** *32* (12), 1035-1042.
29. Fulfer, K. D.; Kuroda, D. G., Solvation Structure and Dynamics of the Lithium Ion in Organic Carbonate-Based Electrolytes: A Time-Dependent Infrared Spectroscopy Study. *J. Phys. Chem. C* **2016,** *120* (42), 24011-24022.
30. Chen, X.; Kuroda, D. G., Molecular motions of acetonitrile molecules in the solvation shell of lithium ions. *J. Chem. Phys.* **2020,** *153* (16), 164502.

31. Lim, J.; Lee, K.-K.; Liang, C.; Park, K.-H.; Kim, M.; Kwak, K.; Cho, M., Two-Dimensional Infrared Spectroscopy and Molecular Dynamics Simulation Studies of Nonaqueous Lithium Ion Battery Electrolytes. *J. Phys. Chem. B* **2019,** *123* (31), 6651-6663.
32. Hahn, N. T.; Self, J.; Seguin, T. J.; Driscoll, D. M.; Rodriguez, M. A.; Balasubramanian, M.; Persson, K. A.; Zavadil, K. R., The critical role of configurational flexibility in facilitating reversible reactive metal deposition from borohydride solutions. *J. Mater. Chem. A* **2020,** *8* (15), 7235-7244.
33. Self, J.; Hahn, N. T.; Fong, K. D.; McClary, S. A.; Zavadil, K. R.; Persson, K. A., Ion Pairing and Redissociaton in Low-Permittivity Electrolytes for Multivalent Battery Applications. *J. Phys. Chem. Lett.* **2020,** *11* (6), 2046-2052.
34. Han, K. S.; Hahn, N. T.; Zavadil, K. R.; Jaegers, N. R.; Chen, Y.; Hu, J. Z.; Murugesan, V.; Mueller, K. T., Factors Influencing Preferential Anion Interactions during Solvation of Multivalent Cations in Ethereal Solvents. *J. Phys. Chem. C* **2021,** *125* (11), 6005-6012.
35. Olson, J. Z.; Johansson, P. K.; Castner, D. G.; Schlenker, C. W., Operando Sum-Frequency Generation Detection of Electrolyte Redox Products at Active Si Nanoparticle Li-Ion Battery Interfaces. *Chem. Mater.* **2018,** *30* (4), 1239-1248.
36. Olson, J. Z.; Schneider, S. H.; Johansson, P. K.; Luk, T. S.; Schlenker, C. W., Stark Tuning Rates of Organic Carbonates Used in Electrochemical Energy Storage Devices. *The Journal of Physical Chemistry C* **2019,** *123* (18), 11484-11492.
37. Pandres, E. P.; Olson, J. Z.; Schlenker, C. W.; Holmberg, V. C., Germanium Nanowire Battery Electrodes with Engineered Surface-Binder Interactions Exhibit Improved Cycle Life and High Energy Density without Fluorinated Additives. *ACS Appl. Energy Mater.* **2019,** *2* (9), 6200-6208.
38. Zhong, C.; Deng, Y.; Hu, W.; Qiao, J.; Zhang, L.; Zhang, J., A review of electrolyte materials and compositions for electrochemical supercapacitors. *Chem. Soc. Rev.* **2015,** *44* (21), 7484-7539.
39. Fawcett, W. R.; Liu, G.; Faguy, P. W.; Foss, C. A.; Motheo, A. J., Attenuated total reflection fourier-transform infrared spectroscopic study of ion–solvent and ion–ion interactions in alkali-metal perchlorate–acetonitrile solutions. *J. Chem. Soc., Faraday Trans.* **1993,** *89* (5), 811-816.

40. Eberspächer, P.; Wismeth, E.; Buchner, R.; Barthel, J., Ion association of alkaline and alkaline-earth metal perchlorates in acetonitrile. *J. Mol. Liq.* **2006,** *129* (1-2), 3-12.
41. Madian, M.; Eychmüller, A.; Giebeler, L.; Madian, M.; Eychmüller, A.; Giebeler, L., Current Advances in TiO_2-Based Nanostructure Electrodes for High Performance Lithium Ion Batteries. *Batteries* **2018,** *4* (1), 7.
42. Teshager, M. A.; Lin, S. D.; Hwang, B. J.; Wang, F. M.; Hy, S.; Haregewoin, A. M., In Situ DRIFTS Analysis of Solid-Electrolyte Interphase Formation on Li-Rich Li1. 2Ni0. 2Mn0. 6O_2 and $LiCoO_2$ Cathodes during Oxidative Electrolyte Decomposition. *ChemElectroChem* **2016,** *3* (2), 337-345.
43. Sharabi, R.; Markevich, E.; Borgel, V.; Salitra, G.; Aurbach, D.; Semrau, G.; Schmidt, M. A., In situ FTIR spectroscopy study of $Li/LiNi_{0.8}Co_{0.15}Al_{0.05}O_2$ cells with ionic liquid-based electrolytes in overcharge condition. *Electrochem. Solid-State Lett.* **2010,** *13* (4), A32.
44. Akita, Y.; Segawa, M.; Munakata, H.; Kanamura, K., In-situ Fourier transform infrared spectroscopic analysis on dynamic behavior of electrolyte solution on $LiFePO_4$ cathode. *J. Power Sources* **2013,** *239*, 175-180.
45. Shi, F.; Ross, P. N.; Zhao, H.; Liu, G.; Somorjai, G. A.; Komvopoulos, K., A catalytic path for electrolyte reduction in lithium-ion cells revealed by in situ attenuated total reflection-Fourier transform infrared spectroscopy. *J. Am. Chem. Soc.* **2015,** *137* (9), 3181-3184.
46. Alves Dalla Corte, D.; Caillon, G.; Jordy, C.; Chazalviel, J.-N.; Rosso, M.; Ozanam, F., Spectroscopic Insight into Li-Ion Batteries during Operation: An Alternative Infrared Approach. *Adv. Energy Mater.* **2016,** *6* (2), 1501768.
47. Lanz, P.; Novák, P., Combined in situ Raman and IR microscopy at the interface of a single graphite particle with ethylene carbonate/dimethyl carbonate. *J. Electrochem. Soc.* **2014,** *161* (10), A1555.
48. Hongyou, K.; Hattori, T.; Nagai, Y.; Tanaka, T.; Nii, H.; Shoda, K., Dynamic in situ fourier transform infrared measurements of chemical bonds of electrolyte solvents during the initial charging process in a Li ion battery. *J. Power Sources* **2013,** *243*, 72-77.
49. Marino, C.; Boulaoued, A.; Fullenwarth, J.; Maurin, D.; Louvain, N.; Bantignies, J.-L.; Stievano, L.; Monconduit, L., Solvation and Dynamics of Lithium Ions in Carbonate-Based Electrolytes during Cycling Followed by Operando Infrared Spectroscopy: The Example of

NiSb $_2$, a Typical Negative Conversion-Type Electrode Material for Lithium Batteries. *J. Phys. Chem. C* **2017,** *121* (48), 26598-26606.

50. Iwasita, T.; Nart, F. C., In situ infrared spectroscopy at electrochemical interfaces. *Prog. Surf. Sci.* **1997,** *55* (4), 271-340.
51. Heimer, T. A.; D'Arcangelis, S. T.; Farzad, F.; Stipkala, J. M.; Meyer, G. J., An Acetylacetonate-Based Semiconductor−Sensitizer Linkage. *Inorg. Chem.* **1996,** *35* (18), 5319-5324.
52. Erkabaev, A. M.; Yaroslavtseva, T. V.; Reznitskikh, O. G.; Bushkova, O. V., Solvation of anions in acetonitrile solutions: FTIR and quantum chemical study for Br^-, ClO_4^-, AsF_6^-, and $CF_3SO_3^-$. *Spectrochimica Acta* **2020,** *229*, 117873.
53. Wang, J.; Polleux, J.; Lim, J.; Dunn, B., Pseudocapacitive Contributions to Electrochemical Energy Storage in TiO_2(Anatase) Nanoparticles. *J. Phys. Chem. C* **2007,** *111* (40), 14925-14931.
54. Mishustin, A. I., Temperature dependence of ion association constants in nonaqueous solutions of metal perchlorates. *Russ. J. Inorg. Chem.* **2013,** *58* (6), 684-690.
55. Pankove, J. I., *Optical processes in semiconductors*. Dover Publications, Inc.: New York, 1971.
56. Szczepankiewicz, S. H.; Moss, J. A.; Hoffmann, M. R., Slow Surface Charge Trapping Kinetics on Irradiated TiO_2. *J. Phys. Chem. B* **2002,** *106* (11), 2922-2927.
57. Berger, T.; Anta, J. A.; Morales-Flórez, V., Electrons in the Band Gap: Spectroscopic Characterization of Anatase TiO_2 Nanocrystal Electrodes under Fermi Level Control. *J. Phys. Chem. C* **2012,** *116* (21), 11444-11455.

Chapter 4. Increased Capacity Retention in Li-Ion Battery Silicon Anodes by Dipole-Modification

4.1 OVERVIEW

With an in situ spectroelectrochemical technique in place and an initial understanding of interfacial ion dynamics within a model system, we turn to study the more technologically-relevant next-generation anode material Si. To address the issues of cycling stability due to SEI cracking from volume expansion during charging, we explore a dipole surface modification strategy. We hypothesized that tuning the electronic structure of the electrode/electrolyte interface, will mitigate unwanted side reactions at crack sites in the SEI. In this chapter, we present data that demonstrates a performance enhancement for our dipole-modified cells, supporting our hypothesis. Recognizing the complexity of this system, we probe the origin of this enhancement further to reveal possible improvements that could be made in the system by suppressing detrimental mechanical and desolvation effects that occurred as a result of our initial modification strategy (functional groups crosslinked to the binder). These results inform fundamental dynamics within a modified system and informs next steps for future improvement strategies.

4.2 INTRODUCTION

Lithium-ion batteries (LIBs) are ubiquitous in our world today. From streamlining portable electronics to fueling electric vehicles, we are reliant on this technology. Made from three active components (anode, cathode, and electrolyte), LIBs are energy storage devices that convert chemical potential energy into electricity to power devices via electrochemical reactions. According to the International Energy Agency (IEA), LIBs will play a pivotal role in reaching net zero emissions by 2050.[1] While decisive progress has been made in this field since the 1970s, projected increases in energy storage demand are steep, necessitating further study into next-generation materials with the potential to meet the challenge.

Since commercialization in the 1990s, graphite has dominated the market for LIB anodes due to its relatively high energy density, high operating voltages impressive cycling stability.[2-5] However, its moderately low theoretical capacity (372 mAh/g) cannot meet the demands of a clean energy future. We turn to next-generation alloying electrodes as an alternative option. Silicon (Si) is a promising candidate due to its appropriate discharge voltage (0.4V vs. Li/Li^+), natural abundance and high theoretical capacity (4200 mAh/g).[6, 7] However, instability of Si cells is a major roadblock for commercialization.

Volume expansion is the source of instability for silicon anodes. During the alloying lithiation process, the particles can expand up to 300% which leads to the following detrimental effects: (1) loss of mechanical integrity due to matrix disconnection (2) host alloy lithium trapping (3) surface oxide reactions (4) aggregation and (5) continued formation of the passivating solid-electrolyte interface.[8-11] Multiple strategies have been explored to address these issues including, but not limited to, nanostructuring of Si,[12] mixed Si/graphite composites,[13] binder optimization,[14, 15] and slurry modification for improved mechanical properties.[16] The work presented in this paper aims to propose a strategy for mitigating the continued SEI formation during cycling.

The SEI is a passivating layer formed on the surface of an electrode due to the decomposition of electrolyte species under reducing potentials.[17-20] The ideal SEI is one that is ionically conductive, allowing lithium ions (Li^+) to migrate through the layer, but electronically insulating, preventing continued irreversible reduction and layer growth.[21] As seen in Figure 4.1a volume expansion causes cracks in the SEI layer begin to form, exposing bare active material (crack sites). Further electrolyte reduction occurs at these sites and over the course of many cycles, the SEI continues to grow. This irreversibly consumes Li^+ and causes unstable cycle performance. In this paper, we propose an interfacial energetic tuning strategy that can act to dynamically respond to the enhanced electric fields at the crack sites and mitigate further SEI formation while allowing for lithium transport across the intact SEI layer (Figure 4.1c). We hypothesize that this heterogeneous modification strategy can act to mitigate volume expansion effects while maintaining electrode cycling integrity.

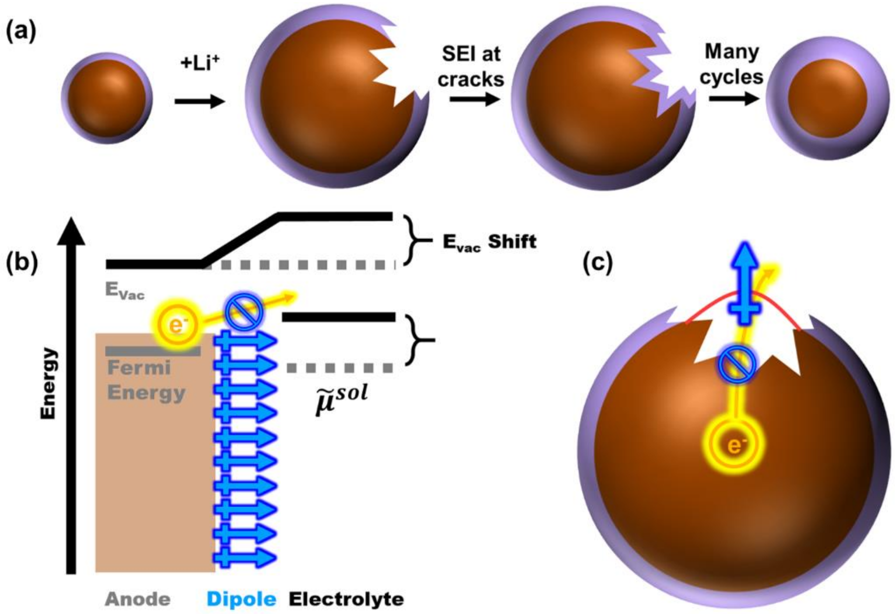

Figure 4.1. (a) Silicon (orange sphere) volume expansion causes cracks in SEI layer (purple layer), further decomposition occurs at these crack sites and over many cycles grows a thick SEI layer which causes capacity fade. (b) dipolar surface modification can shift the Fermi energy of the anode relative to the electrochemical potential ($\tilde{\mu}^{sol}$) of the electrolyte, making electrolyte reduction thermodynamically uphill. (c) interfacial energetic tuning strategy of binder modification (red line with arrow) allows the dipoles to dynamically align at crack sites to mitigate further SEI formation.

If the interfacial charge transfer energetics can be tuned at crack sites (sites without an intact SEI) in silicon, then the degree of excess SEI formation could be controlled. The tuning of electron transfer barrier by engineering interfacial dipole characteristics is an established design strategy in the field of photovoltaics.[22, 23] The charge transfer barrier across an interface is a function of the surface dipole. This surface dipole electrostatically shifts the local vacuum level (ΔE_{VAC}), the energy required to free an electron from the surface, by Equation 4.7:

$$\Delta E_{VAC} = \frac{q_e \mu}{\varepsilon_0 A} \tag{4.7}$$

Where q_e is the charge of an electron, ε_0 is the permittivity of free space, and μ/A is the dipole moment per surface area.[23]

At metal surfaces, a dipole moment may be induced by electron reorganization locally at the interface.[24-27] The interfacial dipole can be tuned by functionalization of the surface with moieties with a permanent dipole moment. The direction of this local E_{VAC} shift is determined by the net dipole moment direction. A dipolar layer oriented away from the surface (i.e., the electron-deficient region proximal to the surface) will induce a local destabilization of E_{VAC}, increasing the barrier to electron transfer across the interface (Figure 4.1b).

This strategy has been deployed to shift the potentials associated with chemical transformation using uniform dipole alignment with respect to a planar interface.[23, 24, 28-35] However, pathways for applying this dipole modification strategy to systems that undergoes dynamic fluctuations in size and shape, as is the case with alloying electrodes for lithium-ion storage, have hitherto been unclear. As a first attempt at applying this strategy to alloying electrodes, we report here a dipolar modification of a composite electrode system consisting of silicon active material, polyacrylic acid (PAA) binder, and conductive carbon additive. Rather than simply modifying the active material surface with a dipolar layer directly, the binder has been modified. We hypothesize that this may allow for dipolar alignment at points in the electrode where the electric field is strong (i.e., defect sites where the field is uncompensated by an ion gradient).

The conformational lability of the dipolar modifiers allows for the electric field to apply a torque and dynamically orient the dipoles such that E_{VAC} is increased at the interface.

4.3 EXPERIMENTAL METHODS

Reagents. Dimethyl carbonate (anhydrous, ≥ 99%), fluoroethylene carbonate (99%), lithium metal ribbon (99.9% trace metals basis, 0.75 mm thickness), poly(acrylic acid) (average M_v ~450,000), and Whatman glass fiber separator (19mm discs, grade gf/f) were purchased from Sigma-Aldrich. 3-cyanopropyltriethoxysilane (97%) and vinyltriethoxysilane (97%) were purchased from Gelest. Silicon powder (crystalline, APS ≤50 nm, 98%, laser synthesized from vapor phase) was purchased from Alfa Aesar. Ethylene carbonate (99%) was purchased from BASF. Conductive carbon (Vulcan XC72R) was purchased from Cabot Corporation. Silicon powder (150 nm, ≥ 99.9%) was purchased from MSE Supplies. Copper foil (9-μm thickness) was purchased from MTI Corporation. Lithium hexafluorophosphate (battery grade, dry, 99%) was purchased from Oakwood Chemical. All CR2032 coin cell components were purchased from Pred Materials International. All reagents were used as received without further purification.

Binder Modification and Electrode Preparation. Poly(acrylic acid) (PAA) was dissolved in deionized (DI) water to achieve a concentration of 67 mg/mL. The binder modification (Figure 2a) was performed by adding the neat silane (3-cyanopropyltriethoxysilane [CPTES] or vinyltriethoxysilane [VTES]) into the PAA solution dropwise in a 1:1 weight ratio. This was stirred for around 18 hours and used immediately to prepare films or electrodes.

Silicon electrodes were prepared using mass ratios of 80% silicon nanoparticles (Si-NP, ≤50nm or 150nm), 10% conductive carbon, and 10% binder (PAA, CPTES-PAA or VTES-PAA). The modifier loading was around 9 % of the total slurry weight. All three components were mixed manually using a mortar and pestle for around 10 minutes. The slurry was then doctor bladed onto a copper foil substrate with a nominal thickness of 38.1 μm and dried on a hotplate set to 80 °C. Once dry, the electrodes were punched out with a 15mm diameter hole punch and stored in a vacuum oven set to 100 °C overnight. Electrodes were then weighed and transferred to an argon-filled MBraun glovebox.

Binder-only films were prepared for characterization using Fourier transform infrared (FTIR) spectroscopy. ITO substrates were cleaned with a consecutive washing protocol of 5 minutes in each of the following: soap + DI water, DI water, acetone, isopropyl alcohol. The binder solutions (PAA, CPTES-PAA, VTES-PAA) were doctor bladed onto the ITO slides using a tape mask (58 μm thickness) and a glass stir rod. These films were dried on a hot plate set to 80 °C and then stored in a vacuum oven set to 100 °C overnight.

Coin Cell Assembly. Half cells were assembled in an argon-filled MBraun glovebox. Briefly, the electrode on the current collector, the glass fiber separator, and the plastic spacer were placed in the stainless-steel cup, consecutively. Then 150 μL of the electrolyte solution [1 M LiPF6 in 1:1 v/v EC:DMC (ethylene carbonate/dimethyl carbonate), with 10% v/v FEC)] was added dropwise onto the glass fiber separator to saturate it. The lithium foil, stainless-steel spacer, stainless-steel spring, and stainless-steel cap were then added to complete the half- cell assembly. A crimper (MTI Corporation) was used to seal the half- cell.

Electrochemical Characterization. Galvanostatic cycling of prepared coin cells was performed with a MACCOR 4200 16-channel cycler. Coin cells were typically cycled at C/20 from OCP to 0.01V and back to 1.2V (vs. Li/Li^+ CE/RE) for a single formation cycle, and subsequently at C/10 between 1.2V and 0.01V until 200 cycles were reached. Capacity data was taken during cycling and differential capacity (dQ/dV) data was calculated from this. Power cycling tests on half cells made using 150 nm SiNP were performed using the following protocol: C/20 formation cycle, C/10 x5, C/5 x5, 1C x5, 2C x5 and C/10x5.

Electrochemical impedance spectroscopy (EIS) measurements of coin cells was performed using a Metrohm Autolab PGSTAT302N potentiogalvanostat in a two-electrode setup. A typical EIS experiment consisted of lithiating the anode to a given state of charge (SOC), and then letting the open circuit potential (OCP) relax until the change in OCP reached less than 1 mV/hr (adapted from Ruffo et al.).[36] Impedance measurements were then made in the frequency range 100,000 Hz to 0.1 Hz, at 10 points per decade of frequency. The AC perturbation amplitude used was 3mV to ensure that pseudolinearity could be assumed. Each impedance measurement at a given SOC was performed twice, the first in descending frequency order, and the second in ascending frequency order, in order to assess the integrity of the data. All measurements showed nearly identical impedance responses between the first and second measurements.

In Situ Vibrational Spectroscopy. *In situ* vibrational ATR spectroelectrochemical measurements were performed using an FTIR spectrometer (Nicolet 8700) and a potentiostat (Autolab PGSTAT302N). The ATR-FTIR experiments used a mercury cadmium telluride (MCT) detector with a spectral range of 650 cm^{-1} to 4000 cm^{-1}, resolution of 2 cm^{-1} and 128 scans. Infrared light passes through the ATR element at an angle of around 60° and the resulting evanescent wave penetrates between roughly 500-3000 nm into the 1M lithium hexafluorophosphate ($LiPF_6$) in 1:1 EC:DMC with 10% v/v FEC electrolyte layer in contact with the binder only films, depending on the wavenumber. See Section 2.3.2 for a description of the air-free *in situ* cell and measurement protocol. For this study, spectra were collected every 4 min.

4.4 RESULTS AND DISCUSSION

Electrostatic Binder Modification. We chose binder modification as an initial strategy for incorporating the dipolar moiety within the electrode slurry. This was chosen in hopes of circumventing the potential for parasitic reactions with the surface modifier if it were directly tethered to the active silicon material. Ideally, the modified binder would be able to accommodate the large volume expansion while keeping the dipolar moieties intact. During lithiation of the electrode, volume expansion will cause cracks in the SEI layer. The enhanced field at these sites will align the dipolar moieties nearby, inducing the vacuum level shift discussed above, and increasing the barrier electrolyte reduction. Where the SEI remains intact, the field is screened by the lithium-ion gradient across the SEI, leaving the dipoles randomly oriented, and thus inducing no local energy level shift. This promotes a selective and dynamic retardation of the electron transfer at crack sites (reducing further SEI growth) while maintaining adequate Li^+ transport through the intact sections of the SEI.

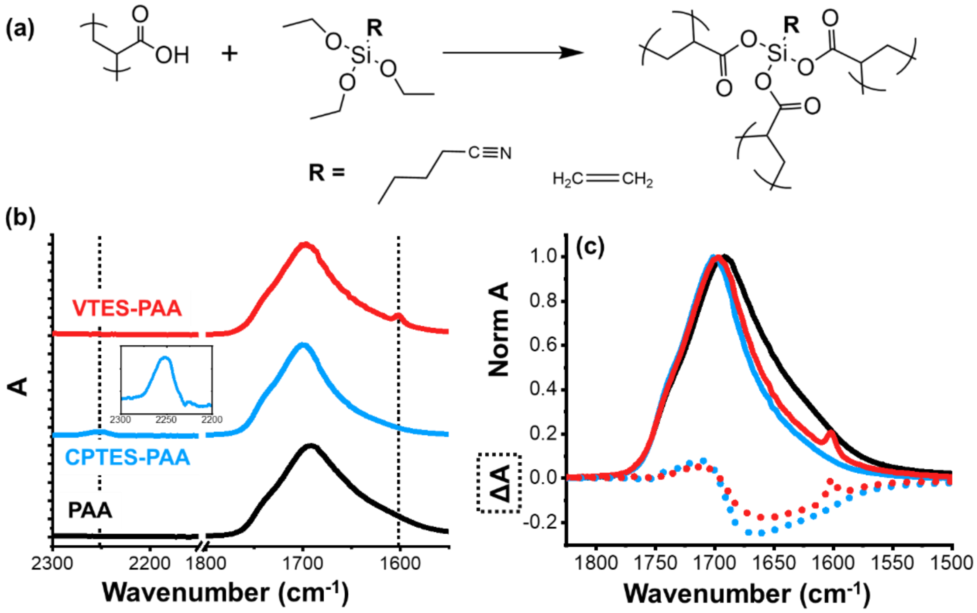

Figure 4.2. (a) Reaction scheme of poly(acrylic acid) (PAA) crosslinking with either 3-cyanopropyltriethoxysilane (CPTES) or Vinyltriethoxysilane (VTES). (b) FTIR characterization

of the functional groups after modification for VTES-PAA (top, 1600 cm-1), CPTES-PAA (middle, 2255 cm^{-1}), and PAA (bottom). (c) Normalized carbonyl stretch of PAA [black], CPTES-PAA [blue] and VTES-PAA [red] (top) with difference spectra (bottom, modified – unmodified) showing blue shift with formation of silyl ester.

Silane-based PAA modification has been used as a strategy for cell improvement in the last several years.[37, 38] These species are advantageous as they afford the option for both binder crosslinking via the -COOH species of the PAA, as well as direct modification of the Si particles. Figure 4.2a. illustrates the scheme for crosslinking between PAA and a triethoxy silane with various functional group options for comparing dipolar vs. nonpolar modifications. We chose two silanes for this study based on their polarity and R-group vibrational activity: 3-cyanopropyltriethoxysilane (CPTES) and vinyltriethoxysilane (VTES). We use FTIR analysis to characterize modified binder films. First, we observe the appearance of the nitrile and vinyl vibrational signatures for CPTES-PAA and VTES-PAA, respectively (Figure 4.2b). Next, we expect to see a blue shift in the carbonyl stretch from the -COOH on the PAA once the silyl ester is formed.[39] Figure 4.2c. shows the vibrational absorption spectra for the C=O stretch in PAA, CPTES-PAA and VTES-PAA binder-only films. Taking the difference spectra of modified binder – PAA-only binder (Figure 4.2c., bottom) it is evident that there is a blue shift which indicate the modification was successful. Lastly, it is apparent that both CPTES-PAA and VTES-PAA have a similar magnitude in frequency shift as well as ΔA which suggest that they each have a similar degree of functionalization and are therefore reasonable candidates to compare.

Electrochemical Performance of Modified Cells. To test our hypothesis, we initially compared coin cells made with the dipole-modified (CPTES-PAA) and unmodified (PAA) binders. These were incorporated into a slurry with a ratio of 8:1:1 silicon nanoparticles (≤50 nm): conductive carbon: binder. We chose nanosized particles (≤ 50nm) to test the influence of our dipolar modifier in a system that is already somewhat optimized for reasonable performance to highlight the realistic potential for improvement that our approach may offer. This strategy mitigates the cracking and fracturing of the particles themselves, which is important to ensure the modification environment stays intact. Over the course of 200 cycles, it is evident that CPTES-PAA shows enhanced cycling stability compared to PAA (Figure 4.3a). This supports our hypothesis that the incorporation of a dipolar modifier should improve cell stability.

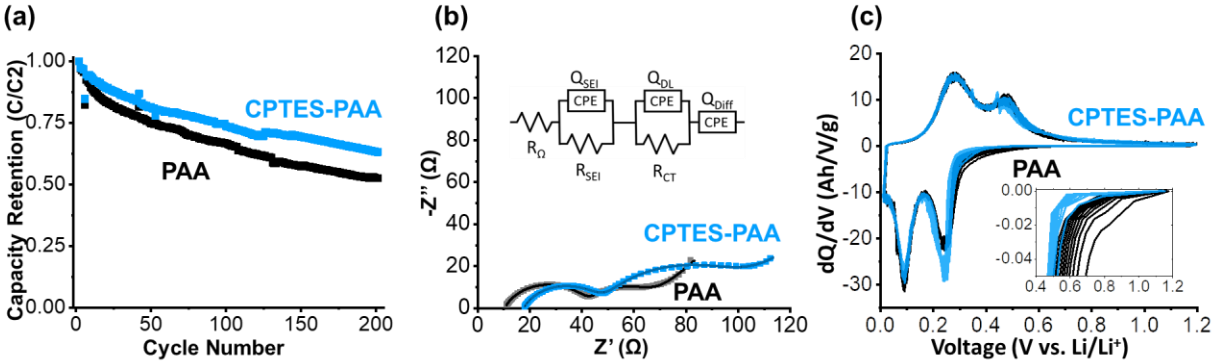

Figure 4.3. (a) Capacity retention (C/C2) of half cells made with 80% 50nm SiNP, 10% conductive carbon, and 10% binder (PAA [black] or CPTES-PAA [blue]). (b) Nyquist plot of half cells after seven cycles using PAA or CPTES-PAA and the corresponding equivalent circuit model and fits (lines), showing an increase in R_{CT} as seen in the second semicircle. (c) Differential capacity (dQ/dV) of the initial cycles for half cells made with PAA (black) and CPTES-PAA (blue).

Table 4.1. Equivalent circuit model fits of Nyquist plots from Figure 4.3

	$R_{\Omega}(\Omega)$	$R_{SEI}(\Omega)$	Q_{SEI} $(s^n\mu\Omega^{-1})$	n_{SEI}	$R_{CT}(\Omega)$	Q_{DL} $(s^n\mu\Omega^{-1})$	n_{DL}	C_{SEI} (µF)
PAA	10.4	32	25	0.755	22.5	2630	0.754	2.47
CPTES -PAA	17.7	29.8	49.7	0.743	51.1	2990	0.718	5.22

We turn to electrochemical impedance spectroscopy to probe the influence of the electrostatic modifier more deeply. The spectra from this measurement are represented in Nyquist plots (Figure 4.3b, bottom) and fit to an equivalent circuit model (Figure 4.3b, top). The equivalent circuit comprises an ohmic resistance (R_{Ω}) in series with a constant phase element (CPE) (to model the low-frequency diffusion) and two parallel R-CPE elements. When fitted, the R-CPE element with the lower time constant (corresponding to the faster process) was assigned to the SEI impedance, and the R-CPE element with the higher time constant was assigned to charge transfer impedance.

To simplify analysis, we will focus on the components related to the SEI and charge transfer (CT). C_{SEI} is inversely proportional to the SEI thickness based on Equation 4.1:[40]

$$d_{SEI} = \frac{\varepsilon\varepsilon_0 A}{C_{SEI}} \tag{4.1}$$

Where ε is the dielectric constant of the SEI, and A is the electrode surface area. The capacitance, C, can be calculated for an R-CPE element by Equation 4.2:

$$C = \frac{(RQ)^{1/n}}{R} \tag{4.2}$$

Where R is the value of the resistance, and Q and n are CPE parameters in Equation 4.3:

$$Z_{CPE} = \frac{1}{Q(j\omega)^n} \tag{4.3}$$

Where Z_{CPE} is the impedance of a CPE, j is the imaginary unit, and ω is angular frequency. From the results shown in Table 4.1 of the equivalent circuit modeling (ECM) of the spectra in Figure 4.3b, we observe that the C_{SEI} is two times larger for CPTES-PAA compared to PAA. This supports our hypothesis that the dynamic response of the dipoles in the system act to dynamically mitigate continued SEI growth and therefore form a thinner SEI compared to PAA.

The charge transfer impedance element consists of a resistance (charge transfer resistance, R_{CT}) in parallel with a CPE representing the electrical double layer at the active material-electrolyte interface (Q_{dl}). Commonly, R_{CT} is interpreted as the charge transfer resistance for the lithium transport from the SEI into the active material.[41] Under this interpretation, an increase in R_{CT} would result in detrimental cycling performance (i.e., worse capacity retention). However, from the equivalent circuit modeling results shown in Table 4.1, it is clear that CPTES-PAA has a larger R_{CT} value compared to PAA, despite its better performance. Therefore, we conclude that this R_{CT} assignment is incomplete.

Due to the reciprocal nature of electron and Li^+ flux in the cell, R_{CT} may be either dominated by transfer of a positively charged particle (Li^+) into the active material or the transfer of a negatively charged particle (electron) out of the active material. The relative contribution of both processes to the overall charge transfer impedance will depend on the relative barrier for either process to occur. Given our prior postulate regarding the dynamic reorientation of the exogenous dipolar moieties occurring primarily at failure points in the SEI since the ion gradient across the intact SEI will nullify the local field. Thus, we hypothesize that a correlation between increased capacity retention and an increase in the R_{CT} value will occur in our dipole modified electrodes. Indeed, we observe that better performance is correlated with a larger R_{CT} value. Evidently, for this specific system, the R_{CT} value and the increase thereof reports on the localized electrostatic response of the dipole modifier near the SEI failure points. In these regions, electron transfer to solvent to form SEI is the primary process, so modulating the barrier primarily affects that process. As the interfacial dipole modification dynamically acts to nullify the interfacial field near the SEI crack sites, pushing the electrolyte reduction more thermodynamically uphill, it is more difficult for this charge transfer to occur, resulting in an increase in the value of R_{CT}.

To further investigate the influence of the dipole modification on the cell behavior, we turn to differential capacity (dQ/dV) analysis (Figure 4.3c). As discussed above, we hypothesize that our heterogeneous modification strategy allows for dynamic mitigation of continued electrolyte reduction while maintaining lithiation processes. Differential capacity analysis reports on electrochemical activity at potentials (V vs. Li/Li^+) corresponding to various processes occurring during (de)lithiation. We note that all four peaks corresponding to Si phase changes during lithiation (0.25V and 0.09V) and delithiation (0.3V and 0.45V) exhibit negligible shifts in overpotential when comparing PAA to CPTES-PAA. This suggests that our modification strategy has not substantially affected the process of (de)lithiation. However, the overpotential for the onset potential which corresponds to electrolyte reduction (0.4V – 1.0V) exhibits a significant cathodic shift of roughly 200 mV for CPTES-PAA compared to PAA.[42] This suggests that we are in fact making it more difficult for further electrolyte reduction to occur when the dipolar modifier is present while maintaining the ability to effectively (de)lithiate the Si active material.

Mechanical Evaluation of Stressed Cells. While we chose to incorporate the electrostatic modifier via binder crosslinking to accommodate the volume expansion, we anticipated the possibility of detrimental mechanical effects. It has been demonstrated that a high degree of silane-based binder crosslinking additives can have an adverse effect on the mechanical properties of the binder, making the electrodes brittle and unable to withstand the strain of volume expansion/contraction.[37] As such, we set out to test a mechanical control to clarify the effects of binder crosslinking versus electrostatic contribution.

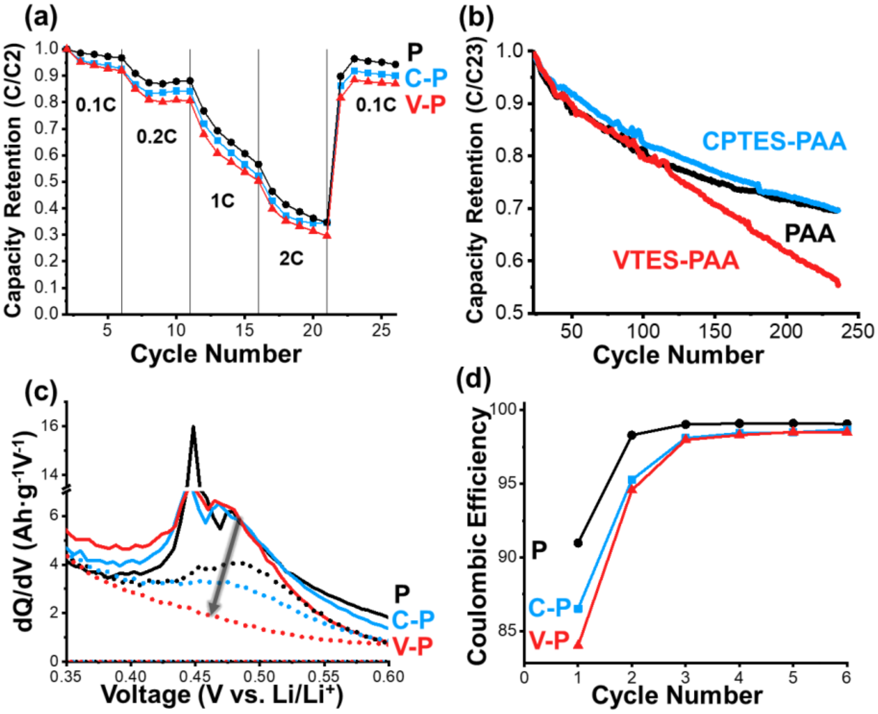

Figure 4.4. Data corresponding to half cells made with 80% 150nm Si NP, 10% conductive carbon and 10% binder (PAA [P, black], CPTES-PAA [C-P, blue], VTES-PAA [V-P, red]). (a) Power cycling test after one formation cycle (C/20). (b) Capacity retention normalized to the 23rd cycle from plot (a) to monitor the stability of the cells after kinetic stress. (c) dQ/dV of cycle 36 (solid) and cycle 236 (dotted) from cycles shown in capacity retention plot. (d) Coulombic efficiency (C.E.) of first six cycles.

To accelerate the detrimental effects of volume expansion and better evaluate the performance of the respective modifiers, we introduced two stressors. First, we switched to a larger Si-NP size (150 nm) to increase the volume expansion effects. This size was selected since it is the critical diameter over which the Si particles crack and fracture upon first lithiation, leading to particle pulverization.[12] Thus, allowing for more pronounced SEI cracking, therefore enhancing the desired effect of electrostatic control, while allowing the particles themselves to stay intact. The second stressor was to subject the cells to a cycling rate test, which would introduce a kinetic challenge to the cells. This allows us to compare the mechanical stability under kinetic stress

(Figure 4.4a), as well as long term cycling performance after both stressors have been applied (Figure 4.4b).

The differences between unmodified (PAA), dipole-modified (CPTES-PAA) and nonpolar-modified (VTES-PAA) Icells are assessed from the data presented in Figure 4. The rate test (Figure 4.4a) suggests that the cells with modified binders perform slightly worse than the unmodified PAA. This corroborates the hypothesis that binder crosslinking at high loadings leads to adverse mechanical effects. To test the cycling stability of these stressed cells, they were cycled out to cycle 236. The capacity retention normalized to C/C23 (second cycle of C/10 after rate test) is shown in Figure 4.4b. It is clear that the nonpolar-modified cell (VTES-PAA) performs the worst of the three cases. This supports the hypothesis that high crosslinking loading causes detrimental mechanical effects and leads to poor cycling stability. The dipole-modified cells (CPTES-PAA) show an initial improvement compared to unmodified (PAA), with convergence at later cycles. The marked improvement of CPTES-PAA versus VTES-PAA seems to suggest that the electrostatic effects of the dipole modification may be enough to overcome the detrimental mechanical effects of crosslinking.

Analysis of the electrochemical characterization provides further insight into the differences between these cells. The differential capacity (dQ/dV) plot in Figure 4.4c shows the last delithiation stage of the discharge process. The combination of sharp and broad peaks around 0.45 V vs. Li/Li^+ is the final stage of delithiation from the crystalline silicon phase.[43] The disappearance of this peak between cycles 36 (solid lines) and 236 (dotted lines) in the VTES-PAA cells suggests that this delithiation phase is inaccessible due to continued SEI growth.[44] While this peak decreases in magnitude for CPTES-PAA, it does not completely disappear as is the case for VTES-PAA and looks more akin to PAA. This suggests that the SEI growth for VTES-PAA is much more drastic than CPTES-PAA or PAA, supporting our hypothesis that crosslinking leads to detrimental mechanical effects.

We assess the initial impact of the modifiers on the cell performance using the coulombic efficiency (CE) of the first six cycles (cycle 1 – formation cycle at C/20, cycles 2-6 – C/10) in Figure 4.4d. The lower initial CE for CPTES-PAA (86.5±0.4%) and VTES-PAA (84.0±0.1%) compared to PAA (91.0±0.1%) suggests a higher degree of initial irreversible processes occur during the formation cycle when crosslinking is present. Additionally, we note that the CE stabilization occurs more rapidly for unmodified PAA, indicating that the binder crosslinking may influence the stabilization of the SEI formation. We will use *in situ* vibrational spectroelectrochemistry to probe this further in the next section.

Mechanistic Insight Using In Situ Spectroelectrochemistry. We turn to in situ FTIR spectroelectrochemistry as a tool for probing mechanistic insights to help shed light on the results discussed above. To simplify analysis and assess how solvation dynamics change with modification, we performed these measurements on binder-only films. In 2021, Martin et.al. discovered that during curing, PAA undergoes a decarbonylation reaction to form a crosslinked polyether network.[45] They describe that this network acts as a solvent cage, promoting desolvation prior to Li^+ transport through the binder. Shutting off the formation of the polyether cage via esterification of the carboxyl moieties, they observed that solvated lithium migrates through the binder medium leading to slow SEI stabilization. We hypothesize that this could be a contributing factor to the slower stabilization of CE in Figure 4.4d.

. For our FTIR analysis, we will focus on the C-O stretching region (Figure 4.5a) to monitor the vibrational reporters for solvated and free DMC (1328 cm^{-1} and 1274 cm^{-1}) and EC (1202 cm^{-1} and 1158cm^{-1}).[46] To test whether our silane crosslinking strategy disrupts this “solvent cage” and slows down desolvation dynamics, we focus on the EC-Li$^+$ signature since EC is the primary species in the inner solvation sheath of Li$^+$.[47] The normalized fits of the intensity of the EC-Li$^+$ diminishing over 60 minutes of cathodic polarization (-1V vs. OCP) and their corresponding time constants (τ) are shown in Figure 4.5b. It is evident that desolvation occurs more quickly for unmodified PAA compared to modified CPTES-PAA and VTES-PAA. This is indicative that our modification does in fact open the solvent cage, promoting solvated lithium to migrate into the binder and slowing down the kinetics for desolvation. Taken together, these data suggest future avenues for further improving our modification scheme to avoid the kinetic penalty associated with our current strategy.

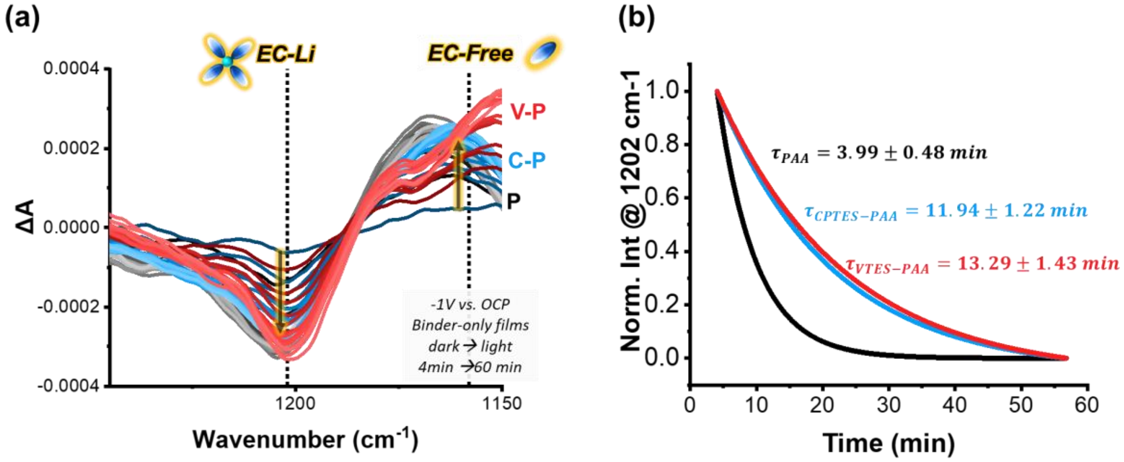

Figure 4.5. (a) In situ spectroelectrochemical FTIR spectra for binder-only films PAA (black), CPTES-PAA (blue), and VTES-PAA (red) in 1M $LiPF_6$ in 1:1 EC:DMC (10% FEC) after -1V (vs. OCP) polarization for one hour. Spectra collected every 4 minutes. Spectral window shows C-O stretch for free and Li-coordinated EC (1202 cm^{-1} and 1158 cm^{-1}), respectively. Negative going peaks represent a diminished concentration of the corresponding species and positive going peaks are the increased concentration (b) EC-Li decay fits normalized for easier comparison with time constants. Due to measurement restrictions, time constants are to be taken as relative values rather than true values.

4.5 CONCLUSIONS

We have shown here that dipolar modification of the binder in a composite electrode system leads to increased capacity retention in Li-ion half cells. Our analysis suggests that, in a technologically relevant system, the improvement from the dipolar modification significantly outweighs the potential drawbacks arising from changes in mechanical and solvation properties associated with this initial implementation method of introducing these exogenous dipole modifiers. The evidence presented here supports the hypothesis that dynamic alignment of the dipolar functionality is a potential mechanism for improving the capacity retention of advanced silicon-based Li-ion battery anodes. At the same time, further study to examine the local chemical, thermodynamic, and conformational changes appear to hold promise for shedding light on potential future improvements for this approach. We also conclude that the method of incorporation is far from optimized. Further study into how best to maximize the dipolar effect and minimize the detrimental effects arising from sub-optimal mechanical and solvation properties appear to be compelling. One initial avenue for optimization may be to increase the ratio of dipolar groups to crosslinking points, possibly by incorporation of oligomers of CPTES rather than monomers. An alternate route for this is to directly modify active material surfaces with chains of dipolar moieties, such that when the surface expands, the chains can stretch out and align with the electric field. With these further studies, design heuristics could be created, and applied to a variety of battery chemistries.

4.6 REFERENCES

1. Bouckaert, S.; Pales, A. F.; McGlade, C.; Remme, U.; Wanner, B.; Varro, L.; D'Ambrosio, D.; Spencer, T. *Net zero by 2050: A roadmap for the global energy sector*; License: CC BY 4.0; International Energy Agency: Paris, 2021.
2. Nzereogu, P. U.; Omah, A. D.; Ezema, F. I.; Iwuoha, E. I.; Nwanya, A. C., Anode materials for lithium-ion batteries: A review. *Applied Surface Science Advances* **2022,** *9*, 100233.
3. Yazami, R.; Touzain, P., A reversible graphite-lithium negative electrode for electrochemical generators. *J. Power Sources* **1983,** *9* (3), 365-371.
4. Asenbauer, J.; Eisenmann, T.; Kuenzel, M.; Kazzazi, A.; Chen, Z.; Bresser, D., The success story of graphite as a lithium-ion anode material – fundamentals, remaining challenges, and recent developments including silicon (oxide) composites. *Sustainable Energy & Fuels* **2020,** *4* (11), 5387-5416.
5. Li, J.; Fleetwood, J.; Hawley, W. B.; Kays, W., From Materials to Cell: State-of-the-Art and Prospective Technologies for Lithium-Ion Battery Electrode Processing. *Chem. Rev.* **2022,** *122* (1), 903-956.
6. Boukamp, B. A.; Lesh, G. C.; Huggins, R. A., All-Solid Lithium Electrodes with Mixed-Conductor Matrix. *J. Electrochem. Soc.* **1981,** *128* (4), 725.
7. Zuo, X.; Zhu, J.; Müller-Buschbaum, P.; Cheng, Y.-J., Silicon based lithium-ion battery anodes: A chronicle perspective review. *Nano Energy* **2017,** *31*, 113-143.
8. Zhang, W.-J., A review of the electrochemical performance of alloy anodes for lithium-ion batteries. *J. Power Sources* **2011,** *196* (1), 13-24.
9. Shi, F.; Song, Z.; Ross, P. N.; Somorjai, G. A.; Ritchie, R. O.; Komvopoulos, K., Failure mechanisms of single-crystal silicon electrodes in lithium-ion batteries. *Nature Communications* **2016,** *7* (1), 11886.
10. Ryu, J. H.; Kim, J. W.; Sung, Y.-E.; Oh, S. M., Failure Modes of Silicon Powder Negative Electrode in Lithium Secondary Batteries. *Electrochem. Solid-State Lett.* **2004,** *7* (10), A306.
11. Kasavajjula, U.; Wang, C.; Appleby, A. J., Nano- and bulk-silicon-based insertion anodes for lithium-ion secondary cells. *J. Power Sources* **2007,** *163* (2), 1003-1039.

12. Liu, X. H.; Zhong, L.; Huang, S.; Mao, S. X.; Zhu, T.; Huang, J. Y., Size-Dependent Fracture of Silicon Nanoparticles During Lithiation. *ACS Nano* **2012,** *6* (2), 1522-1531.
13. Li, X.; Zhang, M.; Yuan, S.; Lu, C., Research Progress of Silicon/Carbon Anode Materials for Lithium-Ion Batteries: Structure Design and Synthesis Method. *ChemElectroChem* **2020,** *7* (21), 4289-4302.
14. Young, B. T.; Nguyen, C. C.; Lobach, A.; Heskett, D. R.; Woicik, J. C.; Lucht, B. L., Role of binders in solid electrolyte interphase formation in lithium ion batteries studied with hard X-ray photoelectron spectroscopy. *J. Mater. Res.* **2019,** *34* (1), 97-106.
15. Nguyen, C. C.; Yoon, T.; Seo, D. M.; Guduru, P.; Lucht, B. L., Systematic Investigation of Binders for Silicon Anodes: Interactions of Binder with Silicon Particles and Electrolytes and Effects of Binders on Solid Electrolyte Interphase Formation. *ACS Appl. Mater. Interfaces* **2016,** *8* (19), 12211-12220.
16. Zhao, Y. M.; Yue, F. S.; Li, S. C.; Zhang, Y.; Tian, Z. R.; Xu, Q.; Xin, S.; Guo, Y. G., Advances of polymer binders for silicon-based anodes in high energy density lithium-ion batteries. *InfoMat* **2021,** *3* (5), 460-501.
17. Peled, E., The Electrochemical Behavior of Alkali and Alkaline Earth Metals in Nonaqueous Battery Systems—The Solid Electrolyte Interphase Model. *J. Electrochem. Soc.* **1979,** *126* (12), 2047.
18. McDowell, M. T.; Lee, S. W.; Nix, W. D.; Cui, Y., 25th Anniversary Article: Understanding the Lithiation of Silicon and Other Alloying Anodes for Lithium-Ion Batteries. *Adv. Mater.* **2013,** *25* (36), 4966-4985.
19. Kim, J.; Chae, O. B.; Lucht, B. L., Perspective—Structure and Stability of the Solid Electrolyte Interphase on Silicon Anodes of Lithium-ion Batteries. *J. Electrochem. Soc.* **2021,** *168* (3), 030521.
20. Wölke, C.; Sadeghi, B. A.; Eshetu, G. G.; Figgemeier, E.; Winter, M.; Cekic-Laskovic, I., Interfacing Si-Based Electrodes: Impact of Liquid Electrolyte and Its Components. *Advanced Materials Interfaces* **2022,** *9* (8), 2101898.
21. Peled, E.; Golodnitsky, D.; Penciner, J., The Anode/Electrolyte Interface. In *Handbook of Battery Materials*, Daniel, C.; Besenhard, J. O., Eds. Wiley-VCH Verlag GmbH & Co. KGaA: Weinheim, Germany, 2011; pp 479-523.

22. Khodabakhsh, S.; Sanderson, B. M.; Nelson, J.; Jones, T. S., Using Self-Assembling Dipole Molecules to Improve Charge Collection in Molecular Solar Cells. *Advanced Functional Materials* **2006,** *16* (1), 95-100.
23. Zojer, E.; Taucher, T. C.; Hofmann, O. T., The Impact of Dipolar Layers on the Electronic Properties of Organic/Inorganic Hybrid Interfaces. *Advanced Materials Interfaces* **2019,** *6* (14), 1900581.
24. Otero, R.; Vázquez de Parga, A. L.; Gallego, J. M., Electronic, structural and chemical effects of charge-transfer at organic/inorganic interfaces. *Surf. Sci. Rep.* **2017,** *72* (3), 105-145.
25. Kahn, A., Fermi level, work function and vacuum level. *Materials Horizons* **2016,** *3* (1), 7-10.
26. Cahen, D.; Naaman, R.; Vager, Z., The Cooperative Molecular Field Effect. *Adv. Funct. Mater.* **2005,** *15* (10), 1571-1578.
27. Cahen, D.; Kahn, A., Electron Energetics at Surfaces and Interfaces: Concepts and Experiments. *Adv. Mater.* **2003,** *15* (4), 271-277.
28. Macleod, B. A.; Steirer, K. X.; Young, J. L.; Koldemir, U.; Sellinger, A.; Turner, J. A.; Deutsch, T. G.; Olson, D. C., Phosphonic Acid Modification of $GaInP_2$ Photocathodes Toward Unbiased Photoelectrochemical Water Splitting. *ACS Appl. Mater. Interfaces* **2015,** *7* (21), 11346-11350.
29. Bastide, S.; Butruille, R.; Cahen, D.; Dutta, A.; Libman, J.; Shanzer, A.; Sun, L.; Vilan, A., Controlling the Work Function of GaAs by Chemisorption of Benzoic Acid Derivatives. *The Journal of Physical Chemistry B* **1997,** *101* (14), 2678-2684.
30. Yang, S.; Prendergast, D.; Neaton, J. B., Tuning Semiconductor Band Edge Energies for Solar Photocatalysis via Surface Ligand Passivation. *Nano Lett.* **2012,** *12* (1), 383-388.
31. Guijarro, N.; Prévot, M. S.; Sivula, K., Surface modification of semiconductor photoelectrodes. *Physical Chemistry Chemical Physics* **2015,** *17* (24), 15655-15674.
32. Vilan, A.; Cahen, D., Chemical Modification of Semiconductor Surfaces for Molecular Electronics. *Chem. Rev.* **2017,** *117* (5), 4624-4666.
33. Chen, Q.; Wang, C.; Li, Y.; Chen, L., Interfacial Dipole in Organic and Perovskite Solar Cells. *J. Am. Chem. Soc.* **2020,** *142* (43), 18281-18292.

34. Bard, A. J.; Bocarsly, A. B.; Fan, F. R. F.; Walton, E. G.; Wrighton, M. S., The concept of Fermi level pinning at semiconductor/liquid junctions. Consequences for energy conversion efficiency and selection of useful solution redox couples in solar devices. *J. Am. Chem. Soc.* **1980,** *102* (11), 3671-3677.
35. Paniagua, S. A.; Giordano, A. J.; Smith, O. N. L.; Barlow, S.; Li, H.; Armstrong, N. R.; Pemberton, J. E.; Brédas, J.-L.; Ginger, D.; Marder, S. R., Phosphonic Acids for Interfacial Engineering of Transparent Conductive Oxides. *Chem. Rev.* **2016,** *116* (12), 7117-7158.
36. Ruffo, R.; Hong, S. S.; Chan, C. K.; Huggins, R. A.; Cui, Y., Impedance Analysis of Silicon Nanowire Lithium Ion Battery Anodes. *J. Phys. Chem. C* **2009,** *113*, 11390-11398.
37. Bie, Y.; Yang, J.; Lu, W.; Lei, Z.; Nuli, Y.; Wang, J., A Facile 3D Binding Approach for High Si Loading Anodes. **2016,** *212*, 141-146.
38. Zeng, X.; Shi, Y.; Zhang, Y.; Tang, R.; Wei, L., Vinyltriethoxysilane crosslinked poly(acrylic acid sodium) as a polymeric binder for high performance silicon anodes in lithium ion batteries. *RSC Adv* **2018,** *8* (51), 29230-29236.
39. Arkles, B.; Launer, P. J., Infrared Analysis of Organosilicon Compounds: Spectra-Structure Correlations. In *Silicon Compounds: Silanes & Silicones*, Gelest, Inc: Morrisville, PA, 2013; pp 175-178.
40. Schneier, D.; Horowitz, Y.; Kasnatscheew, J.; Grünebaum, M.; Wiemhöfer, H.-D.; Winter, M.; Peled, E., Evaluating the Passivation Layer of Freshly Cleaved Silicon Surfaces by Binary Silane-Based Electrolytes. *Batteries and Supercaps* **2021,** *4*, 1611-1619.
41. Keefe, A. S.; Buteau, S.; Hill, I. G.; Dahn, J. R., Temperature Dependent EIS Studies Separating Charge Transfer Impedance from Contact Impedance in Lithium-Ion Symmetric Cells. *Journal of The Electrochemical Society* **2019,** *166* (14), A3272-A3279.
42. Hou, T.; Yang, G.; Rajput, N. N.; Self, J.; Park, S.-W.; Nanda, J.; Persson, K. A., The influence of FEC on the solvation structure and reduction reaction of $LiPF_6$/EC electrolytes and its implication for solid electrolyte interphase formation. *Nano Energy* **2019,** *64*, 103881.
43. Obrovac, M. N.; Christensen, L., Structural Changes in Silicon Anodes during Lithium Insertion/Extraction. *Electrochem. Solid-State Lett.* **2004,** *7* (5), A93.
44. Yoon, T.; Nguyen, C. C.; Seo, D. M.; Lucht, B. L., Capacity Fading Mechanisms of Silicon Nanoparticle Negative Electrodes for Lithium Ion Batteries. *J. Electrochem. Soc.* **2015,** *162* (12), A2325-A2330.

45. Martin, T. R.; Pekarek, R. T.; Coyle, J. E.; Schulze, M. C.; Neale, N. R., Understanding why poly(acrylic acid) works: decarbonylation and cross-linking provide an ionically conductive passivation layer in silicon anodes. *Journal of Materials Chemistry A* **2021,** *9* (38), 21929-21938.
46. Lanz, P.; Novák, P., Combined In Situ Raman and IR Microscopy at the Interface of a Single Graphite Particle with Ethylene Carbonate/Dimethyl Carbonate. *J. Electrochem. Soc.* **2014,** *161* (10), A1555-A1563.
47. Xu, K.; Lam, Y.; Zhang, S. S.; Jow, T. R.; Curtis, T. B., Solvation Sheath of Li+in Nonaqueous Electrolytes and Its Implication of Graphite/Electrolyte Interface Chemistry. *The Journal of Physical Chemistry C* **2007,** *111* (20), 7411-7421.

APPENDIX A: SUPPLEMENTARY INFORMATION FOR CHAPTER 3

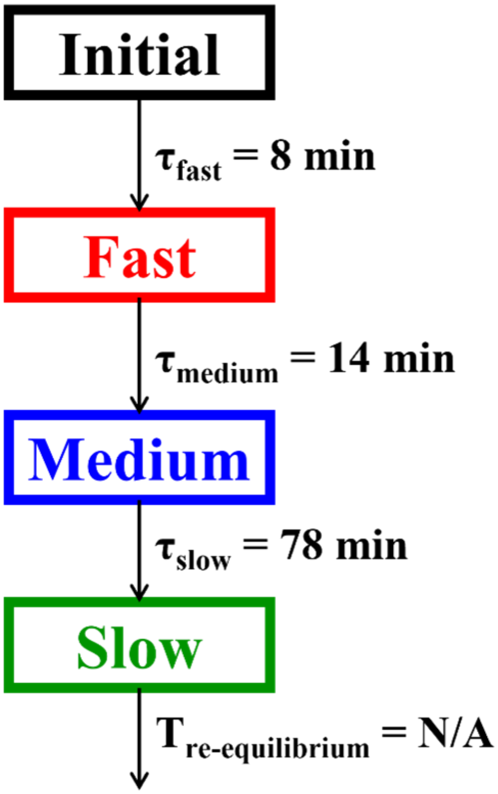

Figure A.1. Unbranched, unidirectional sequential model used for Global Target Analysis (Glotaran). Each box represents the kinetically distinct spectral species which includes all vibrational reporters evolving on the same time constant. The initial spectral species is populated by the speciation change due to the initial applied potential and subsequently decays into the second, Fast species with a time constant of τfast. The Fast species decays into the Medium, the Medium into the Slow, and the Slow decays back to equilibrium. Data was not collected for the process of re-equilibration, so the Slow species represents the longest-lived species but does not provide quantitative information regarding the re-equilibration process.

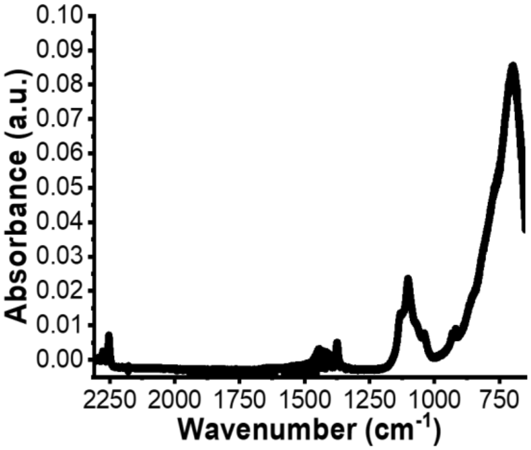

Figure A.2. Full FTIR spectrum of our sample cell with an anatase titanium dioxide electrode and 1.0 M lithium perchlorate ($LiClO_4$) electrolyte. Electrolyte signatures (~2250 cm^{-1} nitrile stretch and ~1100 cm^{-1} perchlorate stretch) and electrode signature (~750 cm^{-1} O-Ti-O stretch) are both resolved in our cell geometry.

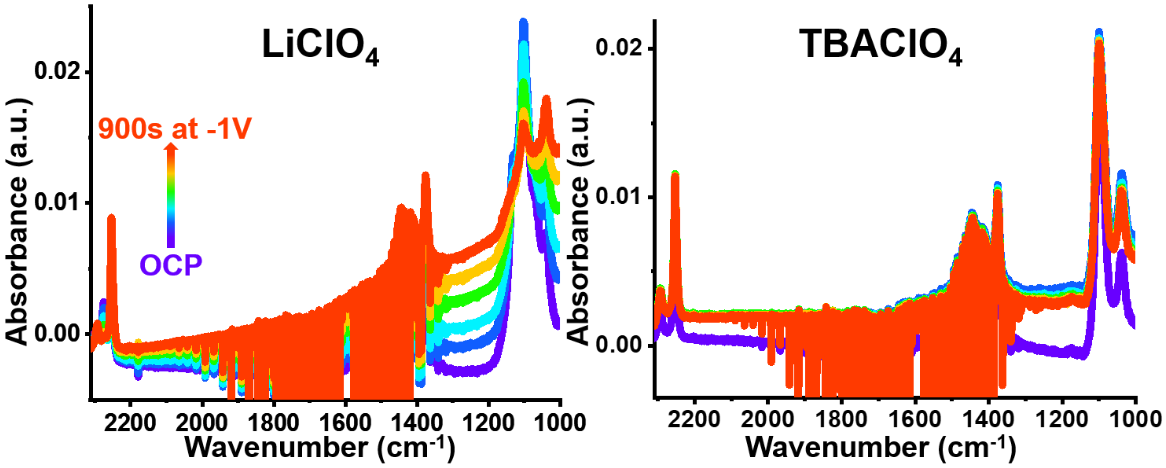

Figure A.3. Broad, structureless signature associated with electron accumulation grows when a potential of -1 V (vs open circuit potential, OCP) is applied using our in situ cell for 1.0 M lithium perchlorate ($LiClO_4$) on the left. No such feature is observed when we switch to a larger cation in 1.0 M tetrabutylammonium perchlorate ($TBAClO_4$) on the right. A frequency independent baseline shift is observed in 1 M $TBAClO_4$.

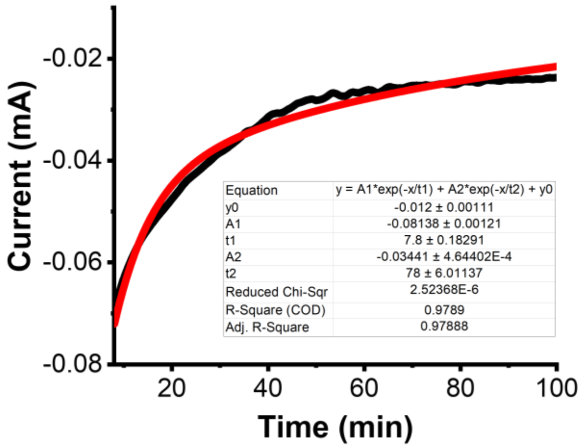

Equation	y = A1*exp(-x/t1) + A2*exp(-x/t2) + y0
y0	-0.012 ± 0.00111
A1	-0.08138 ± 0.00121
t1	7.8 ± 0.18291
A2	-0.03441 ± 4.64402E-4
t2	78 ± 6.01137
Reduced Chi-Sqr	2.52368E-6
R-Square (COD)	0.9789
Adj. R-Square	0.97888

Figure A.4. Chronoamperogram for corresponding in situ FTIR spectroelectroechemical measurement. X-axis scaled to relevant window of 8-100 min to match the corresponding spectral window.

Emma Armstrong Cave

(541) 510-4638 ● Emma.a.cave@gmail.com ● linkedin.com/in/emma-cave-7aa90653/

EDUCATION

University of Washington, Seattle, WA September 2017 - Present
PhD Candidate in Chemistry, CEI Graduate Fellow, Advisor: Prof. Cody Schlenker

Ursinus College, Collegeville, PA August 2008 - May 2012
BS in Chemistry, Magna cum laude, Dean's Honor List 2008-2012, Minors: Mathematics, Spanish, Advisor: Prof. Mark Ellison

WORK EXPERIENCE

Graduate Research Assistant December 2017 - Present
Dr. Cody Schlenker, University of Washington Department of Chemistry, Seattle, WA

- Studies interfacial **ion dynamics**, **charge transfer kinetics** and **silicon electrode surface modification** within rechargeable lithium-ion batteries (LIBs) using electrochemic and spectroscopic techniques
- Fabricates **silicon negative electrodes**, assembles and tests **lithium-ion battery coin cells**
- Chemical hygiene officer: performs safety audits, eyewash checks, training and risk assessments
- Cultivates laboratory growth by mentoring and training both graduate- and undergraduate-level researchers
- *Instruments*: **Maccor** battery testing system, potentiostat, galvanostat, electrochemical impedance spectrometer, Fourier-Transform Infrared (FTIR) spectrometer, argon glovebox, UV-Vis spectrometer, thermal deposition / e-beam evaporator, confocal Raman microscope, solid-state silicon NMR

Graduate Staff Assistant July 2022-Present
Photonics Research Center, University of Washington Department of Chemistry, Seattle, WA

- Supports laboratory management of a multi-user shared research facility (Photonics Research Center) by performing regular instrument maintenance, troubleshooting issues as they arise, and training users on safety and instrument operation

Contractor and Summer Intern July 2021-Present
Membrion, Inc., Seattle, WA

- Supports the Research and Development team via **materials characterization** and grant writing assistance
- Established new experimental protocols for materials preparation, characterization and application

Torrance Tech Due Diligence Analyst September 2019 - June 2020
E8 Angels in partnership with the Clean Energy Institute (CEI) at the UW

- Served as a technical consultant on investment due diligence teams to assess several battery start-up companies
- Collaborated with a team of graduate students and senior fellows to create and present a "Batteries for Angels 101" study group session for the general E8 membership

Environmental Chemist March 2014 - July 2017
Environmental Services Assistance Team (ESAT), EPA Region 3, Fort Meade, MD
Contractor: ICF (December 2016-present), Cherokee Nation Technology Solutions (March 2014-December2016)

- Performed sample preparation, analysis and results report of environmental water, soil and air samples for the Environmental Protection Agency's (EPA) Superfund program
- *Analyses*: Inorganic Anions by Ion Chromatography (EPA 300.0), Dissolved Hexavalent Chromium by Ion Chromatography (Aqueous EPA 218.6/ Soil EPA 3060A), Total Dissolved Solids, Total Suspended Solids, pH

Chemist March 2013 - March 2014
US Army Corps of Engineers, Washington Aqueduct Division, Washington D.C. - Contractor: Spectrum Healthcare Resources

- Performed daily wet chemistry analyses on drinking water samples in accordance with the EPA Clean Water Act Standard Methods, quality control checks, and sample login
- *Analyses*: Ammonia, Free and Total by Ion Selective Electrode, Total Hardness, Calcium and Magnesium by EDTA Titration, Alkalinity, Turbidity, pH, and Chlorine, Total Residual

Research Assistant July 2012 - November 2012
Abt Associates, Bethesda, MD - Contractor: Cherokee Nation Government Solutions

- Assisted in the compiling of a chemical database for the Design for the Environment division of the EPA
- Performed Pollution Prevention analysis for the Toxic Release Inventory Program of the EPA

Undergraduate Research Assistant January 2011 - May 2012
Dr. Mark Ellison, Ursinus College Chemistry Department, Collegeville, PA

- Explored the function of double-walled carbon nanotubes as electron acceptors in organic photovoltaic solar cells

TEACHING EXPERIENCE

Teaching Assistant April 2019 – August 2022
University of Washington Department of Chemistry, Seattle, WA Sept 2017 – Aug 2018

- Supported lecturer and mentored teaching group as Lead Teaching Assistant for 100- and 500-level chemistry courses
- Taught battery electrode fabrication, coin cell assembly and testing for **Battery Module** of "Energy Materials, Devices and Systems" lab course designed by Clean Energy Institute faculty
- Taught discussion sections for general chemistry courses, advised students during help sessions, proctored exams and instructed weekly laboratory sessions for 48 students weekly
- Graded lab reports, exams, and quizzes for 100- and 500-level chemistry courses
- Supported administrative projects such as transitioning to virtual classes

Laboratory Teaching Assistant January 2012 - May 2012
Ursinus College Chemistry Department, Collegeville, PA

- Supported General Chemistry II laboratory by answering questions, grade worksheets, and assisting the professor

PUBLICATIONS

Cave, E. A.; Carr, T. A.; Schlenker, C. W., Dynamically Responsive Electrode Modification for Electrochemical Energy Storage. *In Preparation* 2023.

Cave, E. A.; Olson, J. Z.; Schlenker, C. W., Ion-Pairing Dynamics Revealed by Kinetically Resolved In Situ FTIR Spectroelectrochemistry during Lithium-Ion Storage. *ACS Appl. Mater. Interfaces* 2021, 13 (41), 48546-48554.

PRESENTATIONS

Cave, E. A.; Carr, T. A.; Tran, C.; Schlenker, C. W.: "Dynamically Responsive Electrode Modification for Electrochemical Energy Storage". Presented at the 2022 Orcas International Conference on Energy Conversion & Storage, September 9, 2022. **[Poster]**

Cave, E. A.; "Clean Energy Storage: Lithium-Ion Batteries and Beyond". Presented at UW Clean Energy Scholars Seminar Series, August 3, 2022. Presented at Ursinus College, October 4, 2022. **[Oral Presentation]**

Cave, E. A.; "Ion Pairing Dynamics Revealed by Kinetically-Resolved in situ FTIR Spectroelectrochemistry during Lithium-Ion Storage". Presented at Ursinus College Chemistry Seminar Talks, October 1, 2021. **[Oral Presentation]**

Cave, E. A.; Olson, J. Z.; Schlenker, C. W.: "Interfacial Ion Dynamics in Electrochemical Energy Storage". Presented at the 2020 Orcas International Conference on Energy Conversion & Storage, September 11, 2020. **[Poster - won Audience Choice Award]**

Cave, E. A.; Olson, J. Z.; Schlenker, C. W.: "Monitoring and Manipulating Electric Fields at Electrochemical Energy
Storage Interfaces with In Situ Spectroelectrochemistry". Presented at the 2018 Next Generation Electrochemistry (NGenE) Workshop, June 6, 2019. **[Poster]**

Cave, E. A.; Olson, J. Z.; Schlenker, C. W. "Interfacial Electric Fields in Electrochemical Energy Storage". Presented at the 2018 Orcas International Conference on Energy Conversion & Storage, September 6, 2018. **[Poster]**

Cave, E.A.; Fronheiser, P.; Ellison, M.; "Investigation of the use of double-walled carbon nanotubes in organic solar cells". Presented at the 244th American Chemical Society National Meeting, Philadelphia, PA, August 20, 2012. **[Poster]**

Cave, E.A.; "Investigation of the Use of Double-Walled Carbon Nanotubes in the Production of Organic Solar Cells", 76th Annual Intercollegiate Student Chemistry Convention, April 14, 2012. **[Oral Presentation - 1st prize in the physical chemistry division]**

AWARDS AND HONORS

The American Chemical Society Scholastic Achievement Award ● The Merck Index Award ● Phi Beta Kappa Honors Society ● Kappa Mu Epsilon Mathematics Honors Society ● Diversity, Equity, and Inclusion Leadership Award (UW 2023)

AFFILITATIONS

Promoting Chemistry Undergraduate Research Equity (ProCURE), *Founding Member*	2020-Present
UW Inclusion in Chemical Sciences (InCS), *Member*	2017-Present

Officer Positions*: Vice President* (2020 – 2021) | *Outreach Coordinator* (2018-2020, 2022-2023)

oSTEM at the UW, *Member* 2017-Present

Officer Positions*: President* (2020 – 2022) | *Graduate Outreach Coordinator* (2019-2020)

UW Chemistry Mentorship Network, *Mentor* 2018 - 2020

American Chemical Society (ACS), *Student Member* 2011 - 2012

Ursinus College Beardwood Chemical Society, *Student Representative* 2011 - 2012

COMMUNITY OUTREACH

2017-2018: 1 event, *2018-2019:* 6 events, *2019-2020:* 4 events, *2020-2021:* 1 event, *2021-2022:* 2 events, *2022-2023:* 1 event